Aerodynamic Design of a Flying V Aircraft in Transonic Conditions

Yuri Alexander Laar

Delft University of Technology

TU Delft

Aerodynamic Design of a Flying V Aircraft in Transonic Conditions

by

Yuri Alexander Laar

Student Name	Student Number
Yuri Laar	4659031

Supervisors: Dr. ir. J. Benad, Dr. ir. R. Vos
Project Duration: Dec, 2022 - Oct, 2023
Faculty: Faculty of Aerospace Engineering, Delft

Cover: Flying-V Mach contours, flying above the Mountains

TU Delft

Preface

After six great years, my time as a student has come to an end. With this thesis project I have tried to combine all the knowledge and skills gathered in such a period in one final work. I was hoping I could do something regarding wing aerodynamics for my thesis project, especially after the inspiring Aircraft Aerodynamics course by dr. Veldhuis and the Advanced Aircraft Design course by dr. Vos. When I saw the thesis posting for the Flying V aerodynamic optimization, I knew this was exactly what I wanted to do and I owe a lot to Justus Benad for trusting me to execute such a project. After struggling with non-converging meshes for a while, I can genuinely say that I had a lot of fun trying different ideas and discussing different design options with Justus and Roelof.

I have to thank all the people at the TU Delft who helped me with both the technical and design parts of my project. To start, I want to thank Justus Benad for taking me on and giving me much help and direction during our meetings. Our discussions and Justus positive feedback were a great motivator to keep improving the design and his expertise in aircraft design brought many insights into the design strategy. Secondly, I would like to thank Roelof Vos for his feedback during the Flying V Aerodynamics meetings and the academic feedback on the writing. All his experience brings forth unique insights and directions. I want to thank Alexander Heidebrecht who showed me the basis of transonic simulations in Fluent, answered my questions about meshing patiently and whose scripts were very useful in setting up my own simulation, Nikki van Luijk, my predecessor, for her Flying V introduction, insights and HPC help and CATIA expert Daniel Atherstone for the help with all CAD related problems and the creation of the parametric model.

Next to the academic help, the help from my friends and family was much appreciated over the last year. A special thanks to A. Axel, A. Ruben and A. Davy for keeping me company at IO. Thanks for all the laughs we had and I hope I could also entertain you guys whenever the software froze or a simulation crashed. All the rowing and indoor training for the Ringvaart was a good distraction, so thanks to my rowing squad and rowing friends. Finally, my parental home in Amersfoort and sometimes the Steeg were a nice retreat and a good chance to relax. Thanks to my family for their support over the years. Overall I look back on a great time and I am proud of the achievements of this thesis!

Yuri Alexander Laar
Delft, September 2023

Abstract

With the airline industry almost recovered from the COVID-19 pandemic, the focus on the long-term future can be regained. With expectations of a doubling in passenger traffic in 2040, this growth leads to significant environmental challenges. Part of the solution lies in a more efficient aircraft shape, increasing the lift-to-drag ratio (L/D). Benad envisioned a flying-wing aircraft where payload and fuel both reside in a V-shaped, crescent wing with large winglets that double as vertical tail planes: the Flying V. As the passengers sit in the V-shaped wing, the lift-producing area is increased significantly with respect to a traditional aircraft, while the wetted area is reduced. Based on previous Flying V studies, a new parametrization of the Flying V was constructed by Benad. A detailed aerodynamic optimization is required to maximize the efficiency of this design. This thesis project aims to maximize the lift-to-drag ratio of the Flying V in cruise conditions by means of a high-fidelity CFD investigation.

The design parameters that describe the outer mold line of the Flying V are manually modified and the aerodynamic performance of the aircraft is assessed by means of computational fluid dynamics. The aircraft is parameterized in CATIA, based on previously performed work. The CATIA model ensures a smooth transition between different wing sections. The oval retention parameter (ORT) is introduced, which dictates the position where the oval inner structure stops and the interpolation to the airfoil section starts. The Reynolds-averaged Navier–Stokes equations (RANS) equations are solved to obtain the numerical results. A structured mesh consisting of 15 million nodes with a grid convergence index of 0.01% discretizes the fluid domain. The solver includes a 3rd-order MUSCL spatial discretization, where fluxes are computed using the Roe Flux-Difference Splitting Scheme. The low-Reynolds, Menter SST turbulence model is used. Next to the three-dimensional optimization, a two-dimensional gradient-based airfoil optimization is set up to generate airfoils suitable for the outboard wing. The numerical set-up is validated using ONERA M6 validation data.

The baseline design showed excessive wave drag on the outboard wing and a lack of spanwise lift at the mid-wing. In phase 1 of the design, several iterations were conducted, during which the inner, mid and outboard wing sections were optimized, focusing both on elliptical lift and section performance. A lack of lift in the middle section was resolved by an increase in camber and aft-loading. Improved airfoil sections on the outboard wing were better capable of efficiently generating the required lift coefficient for more elliptical lift. The lift-to-drag ratio obtained was 23.1 at an angle of attack of 3.5 degrees. The second phase consisted of a planform optimization, where small changes were performed to redistribute and reduce wing area. This increased the lift-to-drag ratio to 23.7. In the third phase, the two-dimensional airfoil optimization proved to not increase the L/D. Airfoils obtained from Obert proved to increase efficiency and reduce Mach numbers on the outboard wing. The maximum lift-to-drag ratio obtained was 24.2 at an angle of attack of 3.6 degrees (Mach = 0.85, C_L =0.26, Re = 88.3 million). The drag divergence Mach number is estimated at 0.925.

Contents

List of Figures

List of Tables

Nomenclature

Abbreviations

Symbols	Explanation	Symbols	Explanation
AOA	Angle of attack	NLF	Natural Laminar Flow
AR	Aspect ratio	NP	Neutral Point
AVL	Athena vortex lattice	NPARC	National Program for Applications-Oriented Research in CFD
BL	Boundary layer	ORP	Oval Retention Parameter
BWB	Blended wing body	RANS	Reynolds Averaged Navier-Stokes
CFD	Computational fluid dynamics	Re	Reynolds number
COP	Center of Pressure	SA	Spallart-Allmaras
CRM	Common research model	SC	Supercritical
DNS	Direct numerical simulation	SST	Shear-stress model
FV	Flying V	t/c	Thickness-to-chord ratio
GCI	Grid convergence index	TE	Trailing edge
L/D	Lift-to-drag ratio	TP	Transition point
LE	Leading edge	URANS	Unsteady Reynolds Averaged Navier-Stokes
LES	Large eddy simulation		

Symbols

Symbols	Explanation	Unit	Symbols	Explanation	Unit
a	Speed of sound	m/s	t_{ji}	Viscous stress tensor	N/m^2
A	Area	m^2	u	x-velocity	m/s
c	Chord	m	u_τ	Friction velocity	m/s
C_d	Section drag coefficient	(-)	u^+	Normalized velocity	(-)
C_D	Drag coefficient	(-)	V	Velocity	m/s
C_f	Skin friction coefficient	(-)	v	y-velocity	m/s
C_{ijk}	Turbulent diffusion	m^2/s^3	w	Cabin width parameter	m
C_l	Section lift coefficient	(-)	Y_m	Dilatation of turbulence	kg/sm^3
C_p	Pressure coefficient	(-)	y^+	Normalized y-coordinate	(-)
d	distance	m	α	Angle of attack	rad
D_w	Wave drag	N	β	Prandtl-Glauert correction	(-)
e	Specific Energy	J/kg	δ	Kink angle	rad
F	Flux	(-)	δ^*	Displacement thickness	m
G	Cabin Height Parameter	(m)	δ_v	Viscous length scale	(-)
I	Turbulence Intensity	(-)	δ_x	Boundary layer thickness	m
J	Jacobian	(-)	ζ	Bulk viscosity	Ns/m^2
k	Turbulence kinetic energy	J	ϵ	dissipation	m^2/s^3
L	Planform Length Parameter	m	γ	Ratio of specific heats	(-)
M	Mach number	(-)	Γ	Preconditioning matrix	(-)
p	Pressure	Pa	κ	Von Karman constant	(-)
Pe	Peclet number	(-)	ξ	Damping Coefficient	(-)
Pr	Prandtl number	(-)	Λ	Sweep angle	rad
q	Heat flux	J/m^2	μ	Dynamic viscosity	Ns/m^2
r	Radius	m	ν	Kinematic viscosity	m^2/s
R	Riemann invariant	(-)	ν_T	Eddy viscosity	m^2/s
R_y	Wall normal Reynolds number	(-)	ω	Specific dissipation	Js/m^2
S	Surface area	m^2	ϕ	Velocity potential	m^2/s
S_{ij}	Strain rate tensor	1/s	Π	Pressure-strain correlation	m^2/s^3
t	Time	s	ρ	density	kg/m^3
T	Temperature	K	τ	Slenderness ratio	(-)

1 Introduction

After two years of COVID-19 travel restrictions, the aviation industry has recently been recovering from the reduced number of passenger traffic. As of September 2023, the number of flights is at 90% of pre-COVID-19 numbers [13]. Looking forward, Airbus predicts a yearly growth rate of 3.9%, leading to double the passenger traffic in 2040, with respect to pre-COVID-19 world annual traffic [20]. While this growth might be beneficial from an economic standpoint, an increase in flights leads to a potential increase in emissions. With the European goal of a reduction of CO_2 emissions of 55% in 2030 and climate neutrality in 2050 [41], this growth leads to significant challenges.

Part of the solution lies in a more efficient aircraft shape, increasing the lift-to-drag ratio (L/D). Current aircraft, separating lifting surface (the wing) and payload structure (the fuselage), are seeing diminishing improvements in efficiency over time [30]. A new aircraft concept can improve aircraft efficiency further. Benad [5] envisioned a flying wing aircraft in a V shape: the Flying V. As the passengers sit in the V-shaped wing, the lift-producing area is increased significantly with respect to a traditional aircraft, while the wetted area is reduced. The design also has several advantages over several blended wing body designs. The design poses, for example, an easier trade-off between trimming requirements and an elliptical lift distribution [16]. Aerodynamic studies have been performed on the Flying V with varying degrees of fidelity ([16, 23, 40, 45, 27, 10]). To overcome shortcomings in previous parametrizations, a new CATIA-based parametrization was devised by Benad. This parametrization is the starting point of this study. As the model is only optimized using low-fidelity methods, a need for a high-fidelity study arises. This thesis project aims to maximize the lift-to-drag ratio of the Flying V in cruise conditions by means of a high-fidelity CFD investigation.

1.1. Research Objective

Several aerodynamic studies have been conducted regarding the cruise performance of the Flying V, improving upon the original lattice vortex based optimization of Benad [5]. Notably, Faggiano [16] performed a mixed optimization method of lattice vortex and Euler-based simulations. The parametrization of the Flying V was altered by Hillen [23] and Oosterom [45] to account for manufacturability and introduce family design options, respectively. Van Luijk optimized the new parametrization of the Flying V with a combination of low and high-fidelity methods. The ParaPy model showed, however, some shortcomings [61]. A need for high-fidelity optimization has arisen with a new, CATIA-based, parametrization of the Flying V. The research objective for this thesis topic:

Research Objective

The research objective is to maximize the lift-to-drag ratio of the Flying V in cruise conditions by means of a high-fidelity CFD investigation.

Several sub-objectives have been constructed to facilitate the final objective. These ensure the reliability of the simulation, aim to gain insight into the physics behind the design and cover the multidisciplinary aspects of the design.

Research Sub-Objectives

- Establish a well-validated simulation framework, with a high level of result reliability
- Gather insights about the effect certain parametrization variables have on the aerodynamic performance of the Flying V
- Ensure the accordance of structural and stability requirements with the aerodynamic design

1.2. Research Questions

Based on the research objective, a research question and research subquestions are constructed. The main question should be answered with a numeric value at the end of the thesis. The subquestions aim to guide both the literature review and the research to make sure every aspect of the design is covered.

Research Question

What is the maximum lift-to-drag drag the Flying V can achieve in cruise conditions?

The areas of research are split up into three sections:

- Computational Fluid Dynamics
- Transonic Aerodynamics
- Flying V aerodynamics

Questions related to this research:

1. Computational Fluid Dynamics
   (a) What are the mesh requirements for transonic aerodynamic simulations?
   (b) Which turbulence models are suitable for transonic aerodynamics?
   (c) How should shock regions be refined?
   (d) What is a good advection scheme for transonic aerodynamics?
   (e) What are good validation methods?
2. Transonic Aerodynamics
   (a) What are the consequences of having a highly swept wing in transonic cruise conditions?
   (b) What are the main mechanisms that can cause separation in cruise conditions?
   (c) What are the main factors influencing 2D/airfoil design in transonic conditions?
   (d) Which 3D phenomena have to be taken into account when designing a swept wing?
   (e) What secondary flow principles are important in swept wing design?
3. Flying V aerodynamics
   (a) What are critical aerodynamic areas of the Flying V?
   (b) What is important in the transition from inboard to outboard wing in the Flying V?
   (c) What is the drag divergence Mach number of the final design?
   (d) How does the position of center of pressure change with angle of attack?
   (e) What is the maximum operating Mach number of the final design?
   (f) At what point does buffeting become a risk for the final design?

1.3. Thesis Outlook

The thesis is structured in the following way. Chapter 2 gives an overview of the previously performed aerodynamic Flying V work. Chapter 3 treats the methodology of the thesis. This encompasses the current parametrization of the Flying V, the numerical setup, optimization workflow and physical

design principles. The numerical setup section consists of the theory behind the numerical settings, the meshing strategy, domain and boundary conditions and the simulation setup and convergence strategy. The optimization workflow describes how an iteration is performed. The design principle section describes transonic physics and wing design principles. Chapter 4 verifies and validates the numerical method. The results are presented and discussed in chapter 5. This section also includes the performance of the final design. The thesis is concluded in chapter 6.

2

Flying V Aerodynamic Background

Ever since the start of fixed-wing aviation, engineers and designers have tried to move away from the standard tube-and-wing configuration, towards less conventional configurations. Whether a larger efficiency, more range, more carrying capacity or stealth is the objective, the flying wing and blended wing body (BWB) have shown promising characteristics throughout history.

Figure 2.1: Top left: Dunne D.8 [1], Top right: Northrop YB-35 [2], Bottom left: Northrop Grumman B-2 Spirit [3], Bottom right: Airbus ZEROe BWB [4]

The first functional practical flying-wing concepts arose in Europe around 1910. Inspired by the glider experiments of Otto Lilienthal, one of the first working prototypes was created by J. W. Dunne, with the Dunne D.8[1] [56]. The Second World War brought new attention to flying wings for a military purpose with the benefit of an extended range and flight time, combined with a practical shape for carrying ordinance. The Germans designed the Horten Ho 229 and the Americans designed what would ultimately become the Northrop YB-35[2]. Stability and control remained issues [56]. The YB-35 was ultimately developed into the well known Northrop Grumman B-2 Spirit [3]. Next to its efficiency, the flying wing proved to have good stealth characteristics as well [56].

A different approach is to retain a fuselage-like section, in the form of a blended wing body. An example of this is the Airbus ZEROe BWB[4]. The transonic airliner blended wing body consists of an inboard wing/passenger section with a high thickness-to-chord ratio and a more traditional outboard wing with supercritical airfoils, as described by Liebeck [33]. Chen [12] summarizes the advantages and disadvantages of blended wing bodies as follows: The aerodynamic advantages consist of a reduction of most forms of drag due to a wetted area reduction, smooth transitions and improved lift distributions. Stability, trimming and practical issues are the most significant disadvantages of the BWB.

While multiple studies show the promising efficiency gains of such a configuration [49, 34, 52, 35], the

[1]https://en.wikipedia.org/wiki/Dunne D.8
[2]https://en.wikipedia.org/wiki/Northrop YB-35
[3]https://en.wikipedia.org/wiki/Northrop Grumman B-2 Spirit
[4]https://edition.cnn.com/travel/article/airbus-zero-emissions-concept-plane/index.html

aft-positions of the neutral point and centre of pressure lead to a small moment arm of the control surfaces. This necessitates a large control surface area and results in potential trim drag penalties [49].

2.1. The Flying V

Building on the last hundred years of unconventional planform design, Justus Benad came up with a new flying wing concept at the Airbus Future Projects office in Hamburg: the Flying V [5]. The Flying V is a flying wing aircraft where payload and fuel both reside in a V-shaped, crescent wing with large winglets that double as vertical tail planes. The Flying V promises the efficiency benefits of blended wing bodies, while adhering to logistical constraints similar to the A350 and avoiding the need for an extraordinarily large control surface area [7]. The Flying V fits in the same E-category airport apron as the A350 [5]. As stated by Benad [5]: "Remarkable is also the elliptical lift distribution of the naturally stable design using only a moderate wing twist and no reflexed camber lines.".

The first aerodynamic design was based around the Airbus ODILIA tool, a 3D lattice vortex method. The tool allowed the optimization of the aircraft wing twist, striving for an elliptic lift distribution.

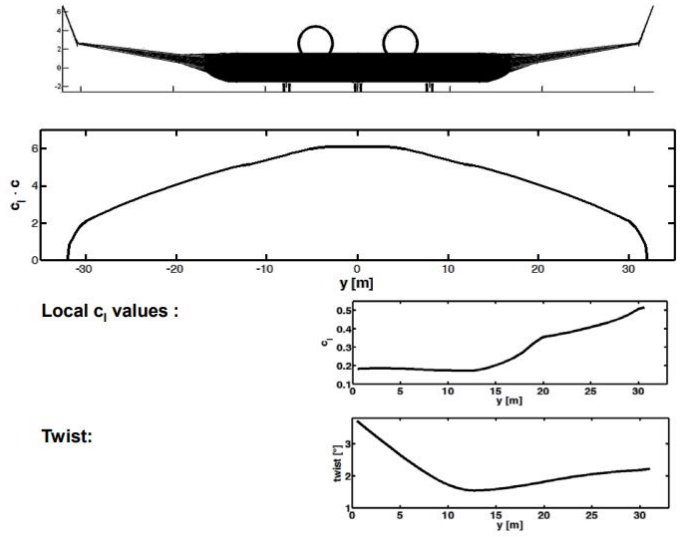

Figure 2.2: Original Flying V lift and twist distribution[5]

The transition between fuselage wing and outboard wing causes a reduction in chord length. This reduction in chord length requires a lower sectional lift coefficient at the root to achieve an elliptical lift distribution (figure 2.2). Due to this low wing loading, the high t/c fuselage wing is less likely to reach pressure coefficients resulting in strong shock waves and wave drag is reduced. Wave drag was therefore disregarded in the original Flying V design. A 10% increase in L/D compared to the A350-900 was estimated [5].

2.1.1. Faggiano's Aerodynamic Optimization

After Benad's original study, the Flying V was further aerodynamically optimized by Faggiano in 2016 [17]. Faggiano implemented Euler solver SU2, together with panel code AVL, into the knowledge-based engineering ParaPy environment [6]. The solver choice is a compromise between optimization fidelity and optimization speed. The Euler code will be able to predict shock waves and wave drag, allowing for a more reliable prediction than Benad's original estimates. By not switching to a RANS-based CFD simulation, the cost of the simulation is still kept relatively low, permitting the use of a large design space.

Faggiano[16] incorporated supercritical Whitcomb airfoils into the outboard wing of the Flying V. With

[5]https://skybrary.aero/articles/icao-aerodrome-reference-code
[6]*https* : *//parapy.nl/*

the original twist distribution, the first results showed excessive lift on the outboard wing, resulting in a less optimal lift distribution. High Mach numbers, resulting in strong shocks were observed at the outboard wing.

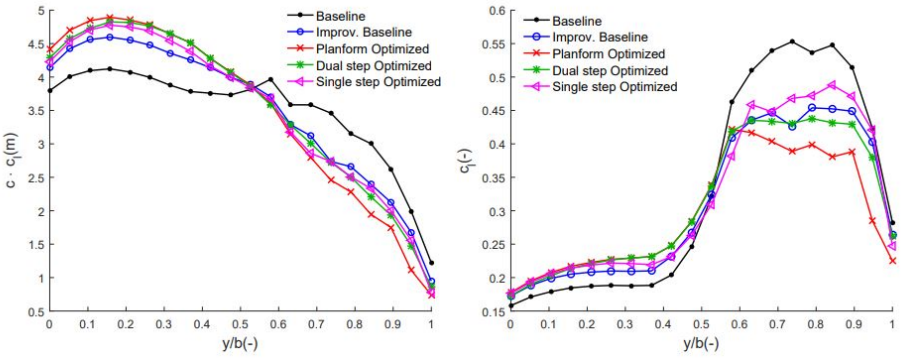

Figure 2.3: Lift distribution of 2016 iteration of the Flying V aerodynamic design[17]

Faggiano decreased the outboard wing twist and swept back the outboard wing further. The effects of this can be seen in figure 2.3, as the improved baseline design. The lift distribution is more elliptical and the c_l at the tip is reduced.

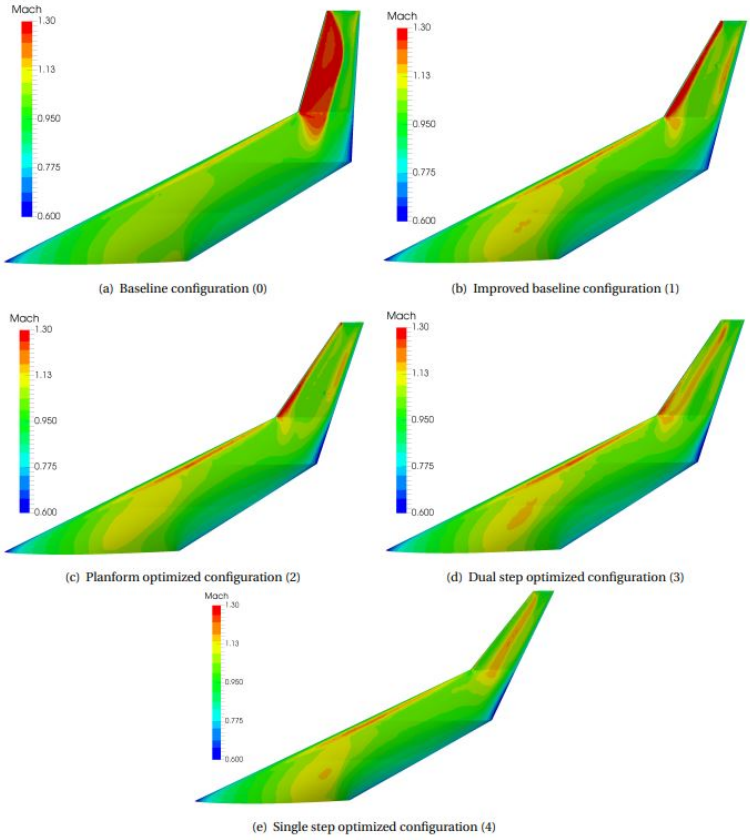

Figure 2.4: Mach contours of the 5 configurations[17]

These manual optimization steps are followed by an optimization algorithm-driven second phase. Two approaches are taken: a dual-step approach, where first the planform and second the airfoils are optimized and a single-step approach, where the whole aircraft is optimized in one step. The taper ratio

is increased, reducing lift at the outboard section. In both approaches, the outboard wing is swept back further and there is a certain degree of front loading introduced into the airfoil, to decrease the suction on the upper surface, with an acceptable pitching moment.

Figure 2.4 shows the results of the optimization. The large supersonic region of the baseline is significantly reduced and a strong shock is avoided. The algorithm-driven optimization reduces the pressure peak at the leading edge and the region of highest velocity can be seen more aft. This also reduced the risk of leading-edge separation, as a possible shock wave does not occur near the leading edge. The maximum Mach number reached is reduced from 1.47 to 1.25 [17]. Compared to the baseline Flying V, the aft loading at the root is reduced, decreasing the pitching moment of the aircraft.

The overall result of the design study was an increase in lift-to-drag ratio from 22.8 to 23.7. Furthermore, the work done increased the fidelity of the aerodynamic performance estimations.

2.1.2. New Parameterization and Family Design

Hillen [23] redefined the parametrization of the Flying V in 2020, as described in section 3.1. The new parameterization allows for cabin flexibility and takes into account manufacturability. The increased cabin size did lead however to a rapid decrease in thickness between the inboard and outboard wing, leading to unfavourable pressure distributions. The lift-to-drag ratio decreased by 13% compared to Faggiano's design.

This new parameterization was used by Niewenhuizen [40], to conceptually optimize the Flying V. Increasing the inboard wing length and decreasing the inboard wing sweep angle promised some significant improvements. The aerodynamic model used is low fidelity, based on the thesis from Faggiano [16], so further aerodynamic investigation is required.

Oosterom [45] investigated the conceptual creation of a Flying V family, altering the parametrization. Oosterom looked at changing the length of the untapered cabin to create a family of aircraft. AVL is used in combination with a viscous model to estimate aerodynamic drag. The lift-to-drag ratio of the family is estimated to be between 20.9 and 21.6, depending on the version. An overall fuel burn improvement of 22% for the FV-1000 was estimated, compared to the A350-1000. Again the aerodynamic modelling method in this study is relatively low fidelity, so a more in-depth study is required.

Van Luijk [61] performed a constrained aerodynamic shape optimisation of the new parametrization. She optimized the planform using a vortex-lattice method and optimized the outboard wing through a Free-Form Deformation shape optimization based on the Euler equations[61]. The highest lift-to-drag ratio obtained was 20.3. It is believed this lift-to-drag ratio can be improved through a parametrization with smoother transitions.

2.1.3. Remaining Aerodynamic Studies

Several other Flying V aerodynamic studies have been performed, most focused on stability coefficients and high lift.

Johnson [27] experimentally investigated the effect of winglet integration on the Flying V. As the winglet and the wing-winglet junction were not significantly aerodynamically optimized, the integration of the winglet reduced the lift-to-drag ratio. The C_L is slightly increased at low angles of attack, due to a decrease in induced angle of attack and slightly decreased at higher angles of attack, possibly due to an increase in separation due to interference effects. The drag coefficient increased in all relevant angles of attack, mainly due to the increase in friction drag.

Optimization of the nose cone of the Flying V was performed by Brouwer [10]. Brouwer simulated the full aircraft at cruise Reynolds number using a RANS approach. At this Reynolds number, Brouwer managed to simulate the boundary layer within the viscous sublayer (y+<1), showing the feasibility of this method for high Reynolds numbers. Different designs are proposed, incorporating the cockpit into the Flying V. The designs generally reduce the aft loading and increase the suction peak, reducing shock strengths, as can be seen in figure 2.5. Different designs show improvements with respect to the original Flying V ranging from 1.3 to 2.7 %.

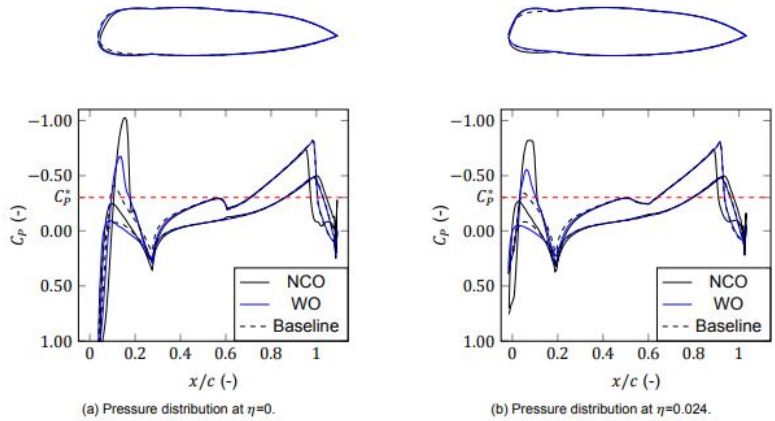

Figure 2.5: Comparison of C_p plots inboard wing from Brouwer. Calculated at M=0.85, $\alpha = 3°$, Re = 8.4e7, C_p*=-0.3[10]

Different experimental and computational research has been done on the high-lift capabilities of the Flying V. Even though high-lift is not the focus subject of this thesis, it can be useful to name some of the key components.

Viet [62] experimentally investigated the high lift behaviour of the Flying V. Viet showed that the Flying V scale model exerts linear C_{L_α} behaviour until an angle of attack of 11 degrees. Beyond 11 degrees, a leading edge vortex at the leading edge kink started to occur, leading to vortex lift and increasing the C_{L_α}. At thirteen degrees, a trailing edge vortex also appears. This vortex starts to merge with the leading edge vortex at higher angles of attack. At higher angles of attack, the leading edge vortex also moves forward and the C_{L_α} starts to decrease. At 41 degrees the wing stalls with a $C_{L_{max}}$ of 1.09. However, a pitch break exists at an angle of attack of 20 degrees, placing stability limits on the Flying V. Van Uitert [60] showed this phenomenon could be slightly improved using trip strips or possibly a stall fence. Benad showed similar vortical structures using high-fidelity simulation methods[8].

Even though it is not the focus point of the study, handling characteristics might influence the efficiency at cruise conditions.

Eigenmodes	**Approach (Ma = 0.2)**				**Cruise (Ma = 0.85)**			
	Forward		Aft		Forward		Aft	
	ς	ω	ς	ω	ς	ω	ς	ω
Short Period	0.683	0.681	0.744	0.609	0.225	2.01	0.303	1.41
Phugoid	$-2.31 \cdot 10^{-3}$	0.161	$-4.37 \cdot 10^{-2}$	0.146	$7.19 \cdot 10^{-2}$	$5.43 \cdot 10^{-2}$	$6.97 \cdot 10^{-2}$	$5.37 \cdot 10^{-2}$
Dutch Roll	$-8.14 \cdot 10^{-2}$	0.992	$-8.97 \cdot 10^{-2}$	0.848	$-7.38 \cdot 10^{-3}$	0.811	$4.68 \cdot 10^{-3}$	0.732
Aperiodic Roll	-	-	-	-	-	-	-	-
Spiral	-	-	-	-	-	-	-	-

Figure 2.6: Damping ratio and natural frequency for eigenmodes of the Flying V.[46]

Using a combination of AVL for the linear regime and wind tunnel testing for non-linear behaviour van Overeem *et al.* [46] showed that the aircraft is trimmable for the whole flight regime, with acceptable elevon deflection at cruise. At approach conditions, slightly unstable Phugoid and Dutch roll eigenmodes were observed (figure 2.6). Level 1 flight handling characteristics were observed for a majority of the flight envelope. Later Joosten [28] showed that the current iteration of the Flying V did have stable lateral eigenmodes, based on an inviscid model.

3

Methodology

This chapter focuses on the parameterization of the Flying V, simulation set-up, optimization procedure and design principles of the research project. The Flying V is parameterized in CATIA, ensuring a smooth transition between the sections. The simulation is performed with ANSYS Fluent using a 3rd-order MUSCL Reynolds Averaged Navier-Stokes simulation. The model is manually optimized to reduce simulation costs and more easily take into account the multidisciplinary aspects of the project.

3.1. Parametrization

The Flying V concept, as envisioned by Benad [5] in 2015, featured a single-shell structure, with two cylindrical pressurized sections. To increase design flexibility, the oval cross-section proposed by Vos et al. [63] was incorporated into the design. Faggiano [16] expanded upon the existing model, enhancing its capabilities to facilitate mid-fidelity optimization. The model was parameterized in the ParaPy environment [1]. The inboard section of the wing is defined by the oval fuselage, while the outboard wing is composed of transonic airfoil sections. An interpolated transition section lies between these sections.

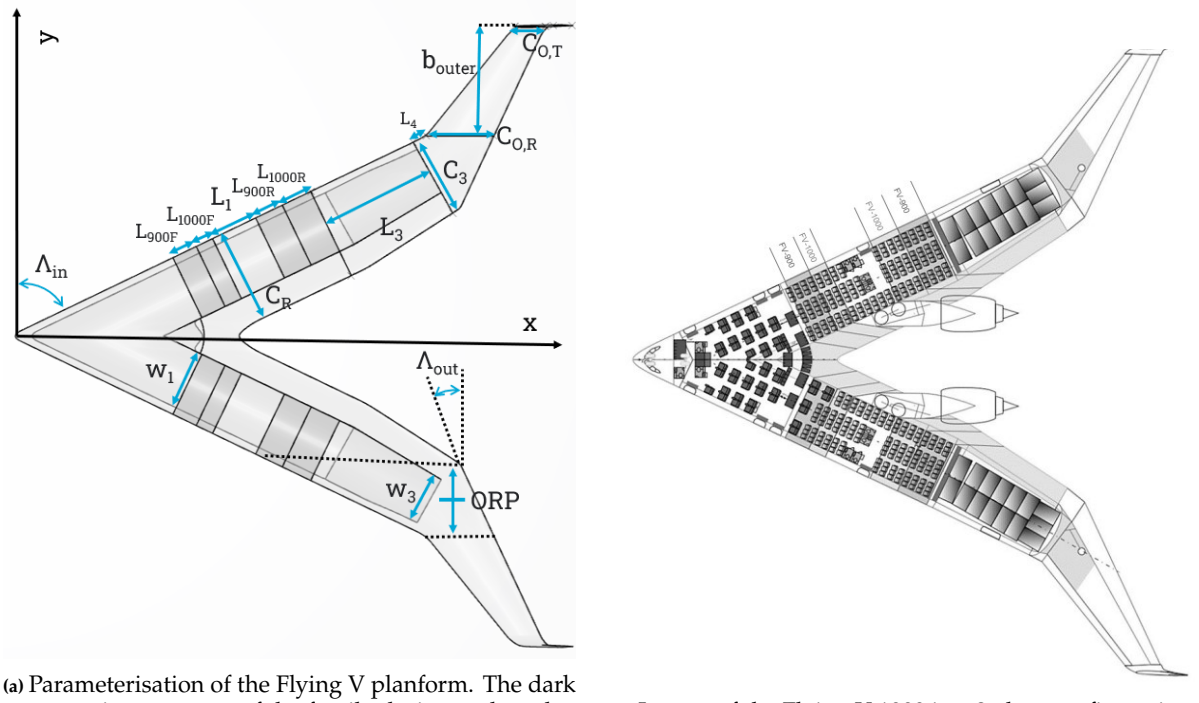

(a) Parameterisation of the Flying V planform. The dark grey sections are part of the family design and can be omitted in different versions.

(b) Layout of the Flying V 1000 in a 2-class configuration, seating 378 passengers [8]

Figure 3.1: Parametrization and layout of the Flying V planform

Hillen [23] redefined the design by taking into account manufacturability and cabin design flexibility. Hillen proposes a constant chord cabin section, for manufacturability reasons. This also introduces a second kink in the trailing edge, as the leading edge is kept straight. In the 2D cabin shape, parameter

[1] *https://parapy.nl/*

H_w is introduced, which fixes the position of the width of the fuselage, allowing more design freedom. Oosterom and Vos [45] investigated the creation of a Flying V family. This introduces sections in the oval cabin that can be omitted to create a smaller aircraft. These are visualised as the dark grey sections in Figure 3.1a. This research focuses on the largest version, the Flying V 1000. The parameterization used by Hillen and Oosterom showed certain shortcomings with regard to the aerodynamic design [61]. In the year of 2022, a novel parameterization for the Flying V was introduced by Benad. It is this parameterization which is used in the present work. In this new version of the Flying V, both the planform and payload capacity from Oosterom's design are retained, as is the family concept and the inboard wing parameterization introduced by Hillen. The most drastic change lies in an updated transition wing section in between the inboard and outboard wing. These changes are described in detail in [6]. The new parameterization is displayed in Figure 3.1a. A distinct feature of the new model is the oval retention parameter (ORP). The ORP determines where the oval cross-section ends and the interpolation to the outboard wing profiles starts. This parameter facilitates a trade-off choice between aerodynamic performance and cabin space. In the creation of the new parametric model, the parameters were set by Benad as an engineering judgment based on the knowledge of previous studies. This initial version is here referred to as the "baseline design".

Further details of the parameterization are as follows: The wing chord, defined orthogonally to the leading edge for the cabin/cargo section, is specified near the root (C_r), at station 3 (C_3) and at the inboard and outboard section of the outboard wing ($C_{O,R}$ and $C_{O,T}$). The cabin width, w_1 and w_3, are important in shaping the sections, as these parameters determine where the cabin section transitions to the trailing edge section, as seen in Figure 3.1a. Sweep angles Λ_{in} and Λ_{out} determine the overall sweep of the design.

The layout of the Flying V 1000 is visualised in Figure 3.4. The configuration is 2-class, seating 378 passengers. The business class is located near the nose of the aircraft with economy in the two wing sections. Cargo is stored further back, as the thickness-to-chord ratio in this region starts to decrease. Fuel is stored in the trailing edge and outboard wing.

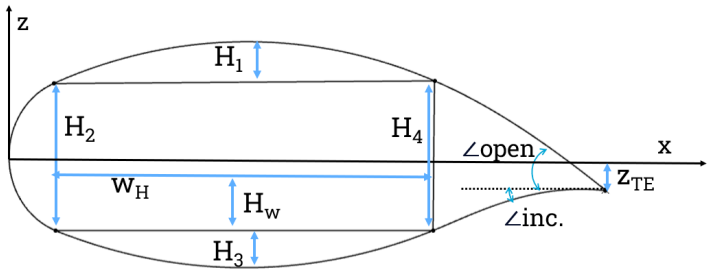

Figure 3.2: Cross-sectional parametrization of the Flying V

Figure 3.2 shows a cross-section of the cabin wing, orthogonal to the leading edge. Parameters H_1 and H_3 are important in defining the camber of the profile as more or less area can be added below or above the chord line. The trailing edge height, z_{TE} and the trailing edge angles, $\angle open$ and $\angle inc.$, also influence camber and aft-loading.

3.2. Numerical Background

To be able to simulate the Flying V in cruise conditions a reliable numerical set-up is required. This section aims to summarize the theory behind the chosen numerical setup options. The motivation of choices is discussed in section 3.5.

3.2.1. The Navier Stokes equations

The transonic conditions of the simulation require a coupled density-based approach, where time stepping is used to converge the simulation [19]. The Favre and Reynolds averaged Navier-Stokes equations [1] (continuity (equation 3.1), momentum (equation 3.2), energy (equation 3.3)) are solved as

a trade-off between accuracy and computational cost.

$$\frac{\partial \bar{\rho}}{\partial t} + \frac{\partial}{\partial x_i}\left(\bar{\rho}\tilde{u}_i\right) = 0 \tag{3.1}$$

A fundamental principle of fluid dynamics is the conservation of mass, expressed by the continuity equation (equation 3.1) [47]. This equation states that the mass that enters a certain system must either accumulate there ($\frac{\partial \rho}{\partial t}$) or be convected through the system and eventually leave the system $\frac{\partial}{\partial x_i}\rho u_i$.

$$\frac{\partial}{\partial t}\left(\bar{\rho}\tilde{u}_i\right) + \frac{\partial}{\partial x_j}\left(\bar{\rho}\tilde{u}_j\tilde{u}_i\right) = -\frac{\partial P}{\partial x_i} + \frac{\partial}{\partial x_j}\left[\bar{t}_{ji} - \overline{\rho u_j'' u_i''}\right] \tag{3.2}$$

Based on Newton's second law, the momentum equation (equation 3.2), relates the acceleration of the fluid to the surface and body forces [47]. The surface forces, of molecular origin, consist of the viscous component $\frac{\partial t_{ji}}{\partial x_j}$ and pressure component $\frac{\partial p}{\partial x_i}$. For external aerodynamic cases, body forces are either considered negligible.

$$\begin{aligned}\frac{\partial}{\partial t}\left[\bar{\rho}\left(\tilde{e} + \frac{\tilde{u}_i\tilde{u}_i}{2}\right) + \frac{\overline{\rho u_i'' u_i''}}{2}\right] + \frac{\partial}{\partial x_j}\left[\bar{\rho}\tilde{u}_j\left(\tilde{h} + \frac{\tilde{u}_i\tilde{u}_i}{2}\right) + \tilde{u}_j\frac{\overline{\rho u_i'' u_i''}}{2}\right] = \frac{\partial}{\partial x_j}\left[-q_{L_j} - \overline{\rho u_j'' h''} + \overline{t_{ji}u_i''} - \overline{\rho u_j''\frac{1}{2}u_i''u_i''}\right] \\ + \frac{\partial}{\partial x_j}\left[\tilde{u}_i\left(\bar{t}_{ij} - \overline{\rho u_i'' u_j''}\right)\right]\end{aligned} \tag{3.3}$$

$$q_j = -\kappa\frac{\partial T}{\partial x_j} = -\frac{\mu}{\mathrm{Pr}_L}\frac{\partial h}{\partial x_j} \tag{3.4}$$

As the density can vary with pressure in a compressible flow, an additional equation is required to compute the density. This is given by the conservation of energy (equation 3.3 [67]), where e is the specific internal energy, q_j the heat flux vector and $h = e + p/\rho$ is the specific enthalpy. The left side of the equation represents unsteady changes and convection of energy, and the right side conduction, diffusion and dissipation of energy. The heat flux can be estimated by Fourier's law (equation 3.4), where $\mathrm{Pr} = \frac{\nu}{\alpha}$ represents the Prandtl number.

3.2.2. Reynolds and Favre Averaging

As the computational costs for Direct Numerical Simulation, DNS, and Large Eddy Simulations, LES, are too great for large-scale, high Reynolds number simulations, the Reynolds Averaged Navier-Stokes or RANS equations will be solved. The RANS approach divides flow variables in its mean ($\overline{\phi}$) and fluctuating (ϕ') components (equation 3.5)[47]. The mean of a flow variable is given by time averaging, as shown in equation 3.6.

$$\phi_i(\mathbf{x}, t) = \overline{\phi_i(\mathbf{x})} + \phi_i'(\mathbf{x}, t) \tag{3.5}$$

$$\overline{\phi_i}(\mathbf{x}) = \lim_{T\to\infty}\frac{1}{T}\int_t^{t+T}\phi_i(\mathbf{x}, t)dt \tag{3.6}$$

In an incompressible flow, the velocity is transformed by equation 3.5 and the whole Navier-Stokes equation is averaged. For all linear terms, no unclosed terms arrive, as the average of the fluctuating quantity is zero. The non-linear $\rho\frac{\partial}{\partial x_i}\left(u_i u_j\right)$ term however leads to the unclosed $\overline{u_i'u_j'}$ term as seen in equation 3.7, also known as the Reynolds stress tensor[47]. This term is to be modelled. As the average of the average is the same average and $\overline{\overline{u_i}u_j'} = 0$:

$$\overline{u_i u_j} = \overline{(\overline{u_i} + u_i')(\overline{u_i} + u_i')} = \bar{u}_i\bar{u}_j + \overline{u_i'u_j'} \tag{3.7}$$

For the compressible NS equations, this approach leads to multiple unclosed terms, as now also the density has a fluctuating component ($\rho = \overline{\rho} + \rho'$):

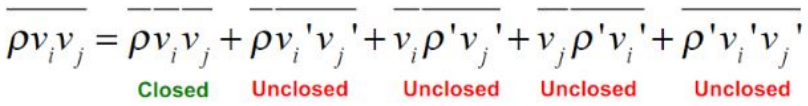

Figure 3.3: Unclosed terms in the compressible Navier-Stokes momentum equation[2]

Modelling all these terms becomes unpractical and unreliable. Favre [18] introduced the idea to mass average the velocity in the NS equations, given by equation 3.8. This way density fluctuations can be avoided. Now the fluctuation is given by equation 3.9

$$\tilde{f} = \frac{\langle \rho f \rangle}{\langle \rho \rangle} \tag{3.8}$$

$$f'' \equiv f - \tilde{f} \tag{3.9}$$

3.2.3. Closing the compressible RANS equations

After Reynolds and Favre averaging the Navier-Stokes equations, one unclosed term in the momentum and 5 unclosed terms in the Energy equation remain. The unclosed terms in the Energy equation seem like much to model, but many of these terms represent physical properties and are often already (partially) modelled by common turbulence models [67]. This section aims to describe the most common ways to close these terms.

$$\bar{\rho}\tau_{ij} \equiv \overline{-\rho u_i'' u_j''} \tag{3.10}$$

By averaging the compressible momentum equation the Favre-averaged Reynolds stress tensor,$\overline{-\rho u_i'' u_j''}$ appears. This is similar to the Reynolds Stress tensor $\rho\overline{u_i' u_j'}$ in incompressible flow. The two most common ways to model this term are either by Eddy viscosity models or Reynolds stress models [19]

Eddy Viscosity Models

The Reynolds stress tensor can be related to the mean flow properties using the Boussinesq approximation (equation 3.11 [67]). The unknown in this equation is the eddy viscosity, μ_T, which has to be modelled. The advantage of the Boussinesq approximation is that it takes the same form as the Navier-Stokes equation, allowing for a simple additional viscosity term. It was shown that the hypothesis is questionable for more complicated flows [47], but it is still widely used due to computational efficiency. Important for the compressible variant is the $-\frac{1}{3}\frac{\partial \tilde{u}_k}{\partial x_k}\delta_{ij}$ term, which tends to 0 in incompressible flow. Again Stokes' hypothesis is used for the bulk viscosity ($\zeta = -\frac{2}{3}\mu$). To guarantee that the trace of τ_{ij} satisfies the definition of the turbulent kinetic energy, the $-\frac{2}{3}\bar{\rho}k\delta_{ij}$ term is subtracted from the mean rate of strain term[67].

$$\bar{\rho}\tau_{ij} \equiv \overline{-\rho u_i'' u_j''} = 2\mu_T \left(S_{ij} - \frac{1}{3}\frac{\partial \tilde{u}_k}{\partial x_k}\delta_{ij} \right) - \frac{2}{3}\bar{\rho}k\delta_{ij} \tag{3.11}$$

Eddy viscosity models aim to estimate the eddy viscosity μ_T. Multiple levels of computational resources (algebraic, one-equation, two-equation) and multiple levels of physics/statistics/estimations are used in the different models. The Menter SST model used in the thesis is discussed next.

k-ω model and Menter SST

The starting point of two-equation eddy viscosity models is a dimensional analysis, relating ν_T (or μ_T in the compressible case) to turbulent flow variables. In the case of k-ϵ, these two flow variables are the turbulent kinetic energy, k and the dissipation rate, ϵ:

$$\nu_T \sim k^{1/2}\ell, \quad \epsilon \sim k^{3/2}/\ell \tag{3.12}$$

[2] *https://brightspace.tudelft.nl/d2l/le/content/397970/viewContent/2611947/View*

Where the $k-\epsilon$ models the dissipation ϵ, ω the dissipation per unit turbulence kinetic energy could be considered. For homogeneous turbulence, the two variables lead to the same results but for inhomogeneous turbulence, the diffusion term changes [47]. The following relations between eddy viscosity, characteristic length and dissipation are proposed:

$$\nu_T \sim k/\omega, \quad \ell \sim k^{1/2}/\omega, \quad \epsilon \sim \omega k \tag{3.13}$$

The turbulence kinetic energy transport equation (equation 3.14) is derived from the momentum equation. The model presented here is the compressible 2006 Wilcox $k-\omega$ model [67].

$$\frac{\partial}{\partial t}(\bar{\rho}k) + \frac{\partial}{\partial x_j}\left(\bar{\rho}\tilde{u}_j k\right) = \bar{\rho}_{\tau_{ij}}\frac{\partial \tilde{u}_i}{\partial x_j} - \beta^*\bar{\rho}k\omega + \frac{\partial}{\partial x_j}\left[\left(\mu + \sigma^*\frac{\bar{\rho}k}{\omega}\right)\frac{\partial k}{\partial x_j}\right] \tag{3.14}$$

Deriving ω from the momentum equation gives too many unclosed terms. Wilcox [67] constructed the transport equation for ω (equation 3.15) on an empirical basis, such that all relevant processes are represented (production, dissipation, diffusion etc.). For the constants used for the equation, the reader is referred to [67].

$$\frac{\partial}{\partial t}(\bar{\rho}\omega) + \frac{\partial}{\partial x_j}\left(\bar{\rho}\tilde{u}_j\omega\right) = \alpha\frac{\omega}{k}\rho\tau_{ij}\frac{\partial \bar{u}_i}{\partial x_j} - \beta\bar{\rho}\omega^2 + \sigma_d\frac{\bar{\rho}}{\omega}\frac{\partial k}{\partial x_j}\frac{\partial \omega}{\partial x_j} + \frac{\partial}{\partial x_j}\left[\left(\mu + \sigma\frac{\bar{\rho}k}{\omega}\right)\frac{\partial \omega}{\partial x_j}\right] \tag{3.15}$$

The main difference between this model and the k-ϵ model is that the k-ω model is superior in the treatment of the viscous near-wall region and can account here for streamwise pressure gradients, partly due to the increased performance in viscous diffusion [47]. However, away from the wall in the non-turbulent regime, k-ω becomes problematic. The model becomes dependent on the boundary conditions, which can become unphysical [47]. Menter [36] proposed the Menter SST model, blending the $k-\omega$ and $k-\epsilon$ models. Menter expresses the $k-\epsilon$ model in the form of ω and adds a term for the principal shear stress. The constants of the equation are then based, as seen in equation 3.16, on essentially the $y+$ value. ϕ is a vector of constants for the Menter SST model, ϕ_1 and ϕ_2 the constants of the $k-\omega$ and $k-\epsilon$ models. F_1 and F_2 determine the region of the flow. The Menter SST model gives significantly improved results for external aerodynamics [47]. It has to be noted that the Wilcox 2006 model also gives significantly improved results in non-turbulent regions compared to the 1994 model, due to tuning of the constants [67].

$$\phi = F_1\phi_1 + (1 - F_1)\,\phi_2 \tag{3.16}$$

3.2.4. Energy Equation Closures

With the Reynolds stress modelled as previously described, four unknowns remain in the Energy equation. As creating transport equations for these terms is computationally expensive, relating them to mean flow variables is more efficient. The most common ways to model these terms are discussed in this section.

Turbulence Kinetic Energy

The $\frac{1}{2}\overline{\rho u_i'' u_i''}$ term represents the turbulence kinetic energy per unit volume, k [67]. This is convenient, as many turbulence models compute k. Otherwise, other approximations are required based on the turbulence model.

$$\bar{\rho}k = \frac{1}{2}\overline{\rho u_i'' u_i''} \tag{3.17}$$

Turbulent Heat-Flux Vector

The Reynolds analogy is the basis for the most used closure of the turbulent heat-flux vector [67]. It assumes the turbulent heat flux to be proportional to the mean flow temperature gradient. The turbulent

Prandtl number Pr_T is flow dependent, but often assumed to be 0.89 [67].

$$q_{T_j} = \overline{\rho u_j'' h''} = -\frac{\mu_T c_p}{Pr_T}\frac{\partial \tilde{T}}{\partial x_j} = -\frac{\mu_T}{Pr_T}\frac{\partial \tilde{h}}{\partial x_j} \tag{3.18}$$

Molecular Diffusion and Turbulent Transport

Molecular diffusion and turbulent transport are usually small and are sometimes neglected for subsonic flows. The most common way to model them is by assuming these terms are proportional to the turbulent kinetic energy gradient, as seen in equation 3.19 [67].

$$\overline{t_{ji}u_i''} - \overline{\rho u_j''\frac{1}{2}u_i''u_i''} = \left(\mu + \frac{\mu_T}{\sigma_k}\right)\frac{\partial k}{\partial x_j} \tag{3.19}$$

3.2.5. Wall Behaviour

Close to the wall, in the buffer and viscous sublayer, certain effects become important. Pope [47] summarizes them as following:

- *Low Reynolds Number*: The turbulent Reynolds number tends to zero near the wall
- *High shear rate*: The maximum mean velocity gradient occurs near the wall
- *Two-component turbulence*: For small y, the u and w components of the turbulence start to dominate
- *Wall blocking* : The pressure field influences the flow due to the no-slip condition

Depending on the model used, corrections or whole models for the region close to the wall might be required. $k-\epsilon$ for example has a poor near-wall performance and requires some kind of wall function [47].

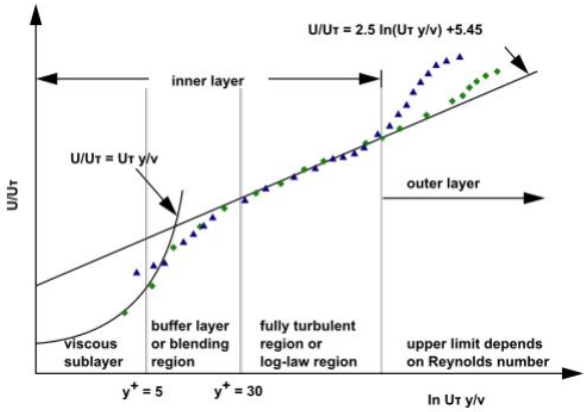

Figure 3.4: Subdivisions of near wall region [1]

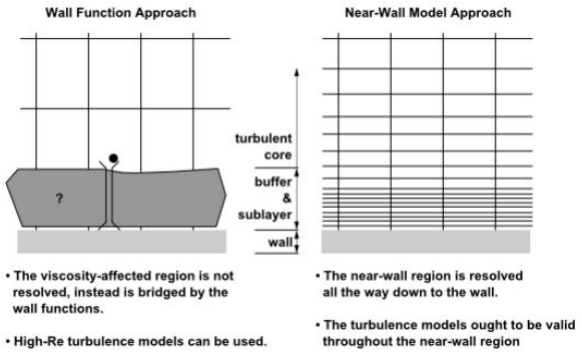

Figure 3.5: Near-Wall treatments [1]

DNS simulations and experiments have shown a similar general shape when non-dimensionalising the region in boundary layers close to the wall. In this region, the flow behaves (relatively) independently of the outside flow. Figure 3.4 shows the subdivisions of the near wall region. Close to the wall viscous diffusion dominates as the velocity at the wall tends to zero. This is known as the viscous sublayer. Further away from the wall turbulence starts to dominate in the log-law region. In between, there is the buffer layer where both phenomena play a role. This region is also the most challenging to model[47].

The surface shear stress at the wall is, apart from flow properties, determined by the mean flow gradient at the wall[47]. A flow close to separation will for example have a lower shear stress, due to the almost reversed flow at the wall.

$$\tau_w \equiv \rho v \left(\frac{\mathrm{d}\langle U\rangle}{\mathrm{d}y}\right)_{y=0} \tag{3.20}$$

From the shear stress, appropriate viscous scales can be set up. These are friction velocity u_τ and viscous length scale δ_v.

$$u_\tau \equiv \sqrt{\frac{\tau_w}{\rho}} \tag{3.21}$$

$$\delta_v \equiv v\sqrt{\frac{\rho}{\tau_w}} = \frac{v}{u_\tau} \tag{3.22}$$

With a viscous length scale defined, the y coordinate can also be non-dimensionalised, such that a wide range of flows can be compared. The resulting $y+$ can be seen as a local Reynold number and its magnitude determines the importance of viscous and turbulence processes [47].

$$y^+ \equiv \frac{y}{\delta_v} = \frac{u_\tau y}{v} \tag{3.23}$$

Also, the mean flow velocity can be normalized. The important point is that this normalized velocity depends solely on $y+$ for $y/\delta \ll 1$ [47].

$$u^+ \equiv \frac{\langle U \rangle}{u_\tau} \tag{3.24}$$

Assuming the log layer only depends on turbulent convection, the log law can be derived, used in the log layer. Where κ is the Von Kármán constant (0.41) and B a constant.

$$u^+ = \frac{1}{\kappa} \ln y^+ + B, \tag{3.25}$$

There are two main approaches to modelling the inner layer. One approach is to refine the mesh sufficiently to model the inner layer (standard $y+$ <1) and modify the turbulence model. Another approach is to not resolve the inner layer and use a semi-empirical wall function [1].

The downside of wall functions is the occurrence of numerical problems with derivatives and the following error in wall shear stress and heat transfer coefficient [67].

3.2.6. Discretization: Finite Volume Method

The partial differential equations described have to be discretized, such that the resulting matrix can be solved by computer algorithms. While both Finite Volume and Finite Element methods are suitable for solving complex fluid dynamics problems, ANSYS Fluent uses a finite volume method.

The finite volume method (FVM) uses the integral formulation of the Navier-Stokes equations. One advantage is the use of divergence theorem. Divergence operators on a cell volume can be expressed as fluxes leaving the surface area of that cell. This way divergence operators, like the continuity equation, become (close to) exact [9]. In a finite volume method, physical quantities can be stored in points, lines, edges and volumes. This brings additional advantages as certain physical properties are better conserved in lines/surfaces/volumes than points. Because of the conservation properties and the relative ease of implementing FVM in complex grids, it has become the dominant way of solving fluid problems [9].

A certain conservation equation is put in its integral formulation [1] (equation 3.26). Where ϕ is a certain scalar quantity, A the surface area vector, Γ the diffusion coefficient and S a certain source term.

$$\int_V \frac{\partial \rho\varphi}{\partial t} dV + \oint \rho\varphi\vec{v} \cdot d\vec{A} = \oint \Gamma_\varphi \nabla\varphi \cdot d\vec{A} + \int_V S_\varphi dV \tag{3.26}$$

For a certain cell, this is discretized in the form:

$$\frac{\partial \rho\varphi}{\partial t} V + \sum_f^{N_{\text{faces}}} \rho_f \vec{V}_f \varphi_f \cdot \vec{A}_f = \sum_f^{N_{\text{faces}}} \Gamma_\varphi \nabla\varphi_f \cdot \vec{A}_f + S_\varphi V \tag{3.27}$$

The $\frac{\partial \rho \varphi}{\partial t} V$ term has to be discretized in time. The convective term, $\sum_f^{N_{\text{faces}}} \rho_f \vec{V}_f \varphi_f \cdot \vec{A}_f$, is often still nonlinear. Equation 3.28 shows the linearized version of the $\rho_f \vec{V}_f \varphi_f$ term, where nb represents the neighbouring cells. The content of these matrices depends on the method used.

$$a_P \varphi = \sum_{nb} a_{nb} \varphi_{nb} + b \tag{3.28}$$

The momentum equation becomes [1], where I is the identity matrix and S is the source term :

$$a_p u = \sum_{nb} a_{nb} u_{nb} + \sum p_f A \cdot \hat{I} + S \tag{3.29}$$

3.2.7. Spacial Discretization

Depending on in which part of the mesh flow properties are stored, interpolation might be required to interpolate values from for example cell centre points to cell boundaries. Different methods of different orders are possible here, depending on which quantity (convective vs. diffusive flux) and other flow properties (shocks, discontinuities) appear in the flow. The viscous fluxes, because of their diffusive nature, are normally discretized using central differences. The diffusive nature of the viscous flux requires information from both cells to deal with high gradients[9]. For convective fluxes, upwind, central difference and high-resolution methods are all feasible.

First Order Upwind

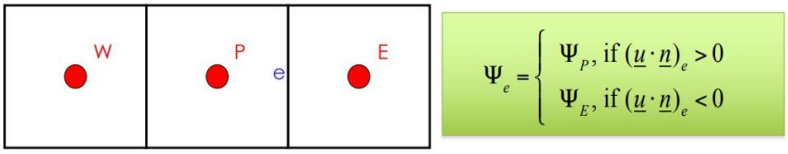

Figure 3.6: First order upwind scheme [3]

First-order upwind is a relatively simple interpolation, where the cell-centre value is assumed to hold true for the entire cell and the value at the cell boundary is equivalent to the centre value. This is computationally stable and efficient, but only recommended for flow that faces the cell direction (structured mesh, laminar flow)[2].

Higher Order Upwind

Higher-order methods can be set up by performing a Taylor series expansion around the centre cell node. For a second-order scheme, the first expansion term is used (equation 3.30). The gradient is required. Gradient computations are discussed in section 3.2.9.

$$\varphi_{fSOU} = \varphi + \nabla \varphi \cdot \vec{r} \tag{3.30}$$

For some simulations, higher-order schemes may not be feasible due to flow fluctuations. Blending methods are a compromise between first and higher-order methods, where a lower blending factor can stabilize the simulation by increasing the numerical diffusion, towards a first-order scheme [1]. This blending coefficient is chosen manually.

Central Differencing

The second-order central differencing scheme uses two cell nodes instead of 1, as shown in equation 3.31 [1]. Also here the gradient of the two cells is required. Central differencing methods normally converge

[3] *https://brightspace.tudelft.nl/d2l/le/content/397950/viewContent/2274109/View*

faster, at the cost of higher numerical diffusion [9]. For processes with a diffusive nature, like viscous diffusion, central difference methods are the superior option.

$$\varphi_{f,CD} = \frac{1}{2}(\varphi_0 + \varphi_1) + \frac{1}{2}\left(\nabla\varphi_0 \cdot \vec{r}_0 + \nabla\varphi_1 \cdot \vec{r}_1\right) \tag{3.31}$$

Stability problems/non-physical wiggles problems can occur in central differencing schemes. Using a deferred correction can avoid stability problems[1]:

$$\varphi_f = \underbrace{\varphi_{f,UP}}_{\text{implicit part}} + \underbrace{\left(\varphi_{f,CD} - \varphi_{f,UP}\right)}_{\text{explicit part}} \tag{3.32}$$

CD stands for central differencing and UP stands for upwind differencing. While the solution converges, the explicit part will become equal to the implicit part, and the final solution will be purely the second-order central differencing solution.

High Resolution and Higher Order Methods

For finer meshes and meshes with discontinuities, like shocks, higher order/high-resolution methods might be a good option. For both high-order schemes and higher-order methods, it is important that the mesh is fine enough: The Peclet number should be lower than 1 ($Pe = \frac{\rho u L}{\Gamma} < 1$) [1].

The **Third-order MUSCL scheme** [32] also blends a central difference and second-order upwind scheme. The blending factor θ is $1/3$. Typically a flux delimiter is introduced to $r_i = \frac{u_i - u_{i-1}}{u_{i+1} - u_i}$ reduce oscillations due to a discontinuity.

$$\varphi_f = \theta\varphi_{f,CD} + (1-\theta)\varphi_{f,SOU} \tag{3.33}$$

If stability becomes an issue in any of the higher-order schemes a relaxation term can be added to the equation leading to the following relation [1]:

$$\varphi_{\text{new}} = \varphi_{\text{old}} + f\left(\varphi_{\text{intermediate}} - \varphi_{\text{old}}\right) \tag{3.34}$$

Where f is the relaxation factor. This can be more efficient than blending with a first-order scheme [2]

3.2.8. Temporal Discretization

For transient simulations or time-stepping methods, the time component has to be discretized. This can be done either implicitly (equation 3.35) or explicitly (equation 3.36). In an implicit way, the flow variable nodes ϕ of a future time are considered, creating the need to solve or estimate the system of equations that arises. The advantage is the unconditionally stable nature of the problem [9]. With an explicit method the system of equations matrices do not have to be inverted for the time step, but the simulation might become unstable [9], requiring very small timesteps (determined by the CFL condition [1]).

$$\frac{\varphi^{n+1} - \varphi^n}{\Delta t} = F\left(\varphi^{n+1}\right) \tag{3.35}$$

$$\frac{\varphi^{n+1} - \varphi^n}{\Delta t} = F(\varphi) \tag{3.36}$$

3.2.9. Gradient Evaluation

The computation of gradients is important in the discretization of the Navier-Stokes equations. It is required to compute the gradients of velocity used for convection and the diffusive terms. Also in interpolation, the gradients are important. Again, many techniques exist, but this section focuses on the Least Squares Gradient Evaluation technique used in the thesis project.

Least Squares Gradient Evaluation

In the least squares method, a linear relation between two nodes is assumed, where r_i is the distance between two nodes [1]:

$$(\nabla\varphi)_{c0} \cdot \Delta r_i = (\varphi_{ci} - \varphi_{c0}) \tag{3.37}$$

A system of equations can be set up relating a centre cell to all its surrounding centre cells:

$$[J](\nabla\varphi)_{c0} = \Delta\varphi \tag{3.38}$$

Where J is a matrix based on the distances between cells. This system is overdetermined, so a least squares method is used to set up the gradients, based on the minimization of the problem. The least squares method is relatively cheaper than the node-based method with similar results [1].

3.2.10. Flow Solvers

There are two main approaches solving for the pressure when discretizing the Navier-Stokes equations. The pressure-based approach calculates the pressure by manipulating the momentum and continuity equations. Even though this was originally developed for incompressible flow (pressure is independent of temperature), compressible formulations are also possible [1]. The density-based approach determines the density from the continuity and energy equation and calculates the pressure using the equation of state [1]. This is intended for compressible flows, as it is both more expensive and numerical errors can occur when performing the density approach for incompressible flow.

Density Based Solvers

The continuity, momentum and energy equations can be combined in the following system [1]:

$$\frac{\partial}{\partial t}\int_V W dV + \oint [F - G] \cdot dA = \int_V H dV \tag{3.39}$$

With vectors W,F and G:

$$W = \begin{pmatrix} \rho \\ \rho u \\ \rho v \\ \rho w \\ \rho E \end{pmatrix}, F = \begin{Bmatrix} \rho v \\ \rho v u + p\hat{i} \\ \rho v v + p\hat{j} \\ \rho v w + p\hat{k} \\ \rho v E + pv \end{Bmatrix}, G = \begin{Bmatrix} 0 \\ \tau_{xi} \\ \tau_{yi} \\ \tau_{zi} \\ \tau_{ij} v_j + q \end{Bmatrix} \tag{3.40}$$

Vector H contains source terms, like energy and body forces.

This system of equations becomes stiff for low Mach number/incompressible flow, because of the large difference between the flow speed and the speed of sound. [1]. Density-based solvers can still be used for these low-speed scenarios but the system of equation 3.39 has to be **preconditioned**; that is modifying the time derivative term, by adding an additional matrix that scales the eigenvalues [1].

Convective Fluxes

Vector F in equation 3.39 represents an inviscid convective flux. As this flux tends to move with the flow direction an upwinding scheme can be beneficial [1]. A **Roe-Flux-Difference splitting scheme** [51] splits up F in the speeds and direction the characteristic information of the flux is travelling according to the eigenvalues. F is thus split at the face in a left, L, and right, R, side with the different eigenvalues contained in matrix $\hat{A}$ according to equation 3.41.

$$F = \frac{1}{2}(F_R + F_L) - \frac{1}{2}\Gamma|\hat{A}|\delta Q \tag{3.41}$$

Where Q is the vector $\{p, u, v, w, T\}^T$, δQ the spatial difference between Q_r and Q_L. F_r and F_L are computed using vectors Q_R and Q_L. Matrix $|\hat{A}|$ is defined as:

$$|\hat{A}| = M|\Lambda|M^{-1} \tag{3.42}$$

Where Λ is the diagonal matrix with eigenvalues and M is the modal matrix reflecting the eigenvectors.

3.2.11. Solving the system

All the methods described thus far result in a certain system of equations that has to be solved either implicitly or explicitly. The high number of cell nodes in the thesis project, combined with the high transonic conditions require a multigrid method.

Multigrid Methods

Due to differences in velocities (boundary layer vs stagnation vs free stream vs speed of sound) and differences in timescales of certain processes (the diffusion timescale is much larger than the wave propagation time scale at high RE) the resulting systems of equations for implicit methods and the scalar equations (e.g. turbulence) for explicit methods are stiff [67]. An efficient way to solve stiff systems is a multigrid method, where corrections on coarse levels are performed using the finer grid levels to accelerate convergence speed.

The basic principle of a multigrid method is to split up the solution of algebraic system $A\varphi + b = 0$ into an approximate part (ϕ_e) and a correction (ψ): Parameter d is the error of the approximate solution,ϕ_e, gives. Mathematical manipulation gives [1].

$$A\psi + d = 0 \tag{3.43}$$

Equation 3.43 is the correction equation which can be solved on the coarse grid. The defects are transferred down to the finer grids:

$$A^H\psi^H + Rd = 0 \tag{3.44}$$

Where H represent the coarse operators and matrix R transfers the defects down to finer levels. Finally, ϕ is updated with a correction for the finer levels, represented by matrix P:

$$\varphi^{\text{new}} = \varphi + P\psi^H \tag{3.45}$$

Algebraic Multigrid (AMG)

The algebraic multigrid method is called algebraic, because it does not redistribute the mesh or rediscretize the geometry. This has the advantage that it can be used for a wide array of cases. However, non-linearities are not carried over to the coarse mesh, which can be done with the Full-Approximate Storage (FAS) method [1].

Hutchinson and Raithby [25] proposed a method based on piecewise constant interpolation between the levels. The coarse cell has no geometrical features, but is a mathematical construct. This way the restriction matrix R, becomes the transpose of the correction matrix P[25].

$$P = R^T \tag{3.46}$$

The defect associated with the corrected fine level should vanish when transferring back to the coarse level. This gives the condition:

$$Rd^{new} = 0 \tag{3.47}$$

Transferring back to equation 3.44 leads to equation 3.48. Where the RAP term is the coarse level operator A^H.

$$RAP\psi^H + Rd = 0 \tag{3.48}$$

The order in which the switch between coarse and fine grid occurs, and filtering/corrections are applied is known as a cycle. The cycle used by the algebraic multigrid method is the F cycle [25], of which the procedure is laid out in equation 3.49

$$\text{pre sweep} \rightarrow \text{restrict} \rightarrow \text{W cycle} \rightarrow \text{V cycle} \rightarrow \text{prolongate} \rightarrow \text{post sweep} \tag{3.49}$$

A pre-sweep is related to the reduction of high-frequency components by iterating on a fine grid. Restriction is the switch to a coarser grid level. Next cycles, known as V and W cycles are performed. A V cycle goes from fine to coarse to fine again, while a W cycle can switch between coarse and fine grids at any step [25]. Prolongation refers to the transfer function to switch back to the fine grid again. Finally, the post relaxation gird occurs on the fine grid, to remove high-frequency errors [25].

A flexible cycle is also possible, where switches between levels are made based on the residual reduction rate [1].

3.3. Meshing Strategy

The creation of a good mesh that adheres to the requirements set by the discretization and turbulence options is an important feature of a good simulation. Regions of steep gradients, like boundary layers or regions of vortex interaction, should be refined to properly capture these phenomena. The three main mesh options are a structured mesh, where neighbouring cells have similar topological features, an unstructured mesh, where neighbouring cells can differ significantly topologically and a hybrid mesh blending the two approaches, often by means of a prism layer near the wall.

A structured mesh is the preferred option for this simulation, as the geometry is relatively simple and significant gains can be achieved with structured meshes compared to unstructured meshes [19].

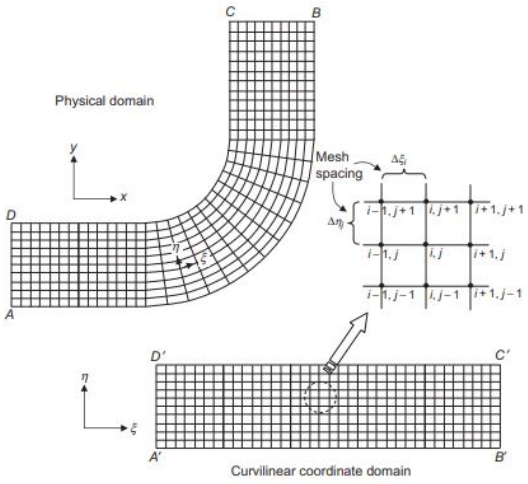

Figure 3.7: Example of a physical mesh and corresponding computational geometry [59]

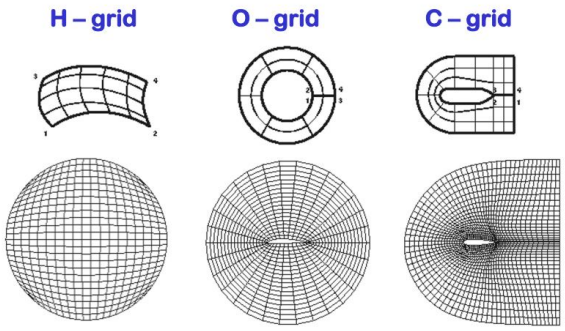

Figure 3.8: Different types of structured meshes[4]

The structured mesh, often consisting of hexahedrons, has a relatively straightforward ordering structure. The grid points are addressed by i,j and k numbers in the x,y,z Cartesian directions. However when dealing with changing meshes, like wall refinements or bends (figure 3.7), the storage of coordinate physical properties would lead to large memory requirements and solving times. The system is therefore solved in the curvilinear coordinate domain [59] (figure 3.7) and a transformation is applied (x,y -> ξ,η) to transform the physical problem to the computational domain. This can either be done by interpolation or by relating the coordinate systems with partial differential equations (like the Poisson equation) [59], with the grid points as boundary values. Using the elliptical approach the coordinates are related by:

[4] *https://brightspace.tudelft.nl/d2l/le/content/397950/viewContent/2274113/View*

$$\begin{aligned} \frac{\partial^2 \xi}{\partial x^2} + \frac{\partial^2 \xi}{\partial y^2} &= P(\xi, \eta) \\ \frac{\partial^2 \eta}{\partial x^2} + \frac{\partial^2 \eta}{\partial y^2} &= Q(\xi, \eta) \end{aligned} \tag{3.50}$$

In a practical sense, a structured mesh is often applied in block form. The mesh domain is connected using certain blocks, wherein each block cells have similar parameters. This allows different rules for different parts of the mesh, making it easier to create meshes for more complicated geometry.

These blocks are given characteristics, usually in the form of H, O or C- grids. Depending on the shape of the physical product, well-fitting shapes can be selected.

The mesh is subjected to the following criteria: The determinant is the most important factor in a structured mesh [3]. It is a measure of the smallest divided by the largest determinant in the Jacobian matrix. A determinant of 1 dictates a totally regular mesh element, a negative determinant implies an inverted edge. The minimum value should be 0.3[3]. Rumsey, in a NASA assessment of current CFD capabilities, recommends streamline spacing of the grid to be no more than 0.1% of the chord near the leading edge and 0.2% of the chord near the trailing edge [53]. In the wake, the grid should be aligned with the trailing edge bisection angle to align the grid with the flow direction [53]. Goetten et al. [21] recommend 80-100 cells in the chord direction on lifting surfaces if no transition model is used. The **skewness**, expressed by angle θ, is important to avoid numerical instabilities. Generally, $\theta < 30°$ or $\theta > 150°$ is recommended. Close to the wall θ should be close to 90 degrees [59].

One of the challenges of setting up a mesh is estimating the set-up of the prism layer beforehand. Spalart [58] recommends a prism layer growth rate of 1.25 when looking at different turbulence models and between 1.05 and 1.2 when taking into account numerical dissipation.

The wall-normal coordinate can be estimated, by estimating the skin friction. Equation 3.21 and 4.4 can be used to compute the wall-normal coordinate. Different empirical relations exist, most based on the Reynolds number. For high Reynolds numbers (based on a flat plate) Schlichting derived [54]:

$$C_f = \left[2\log_{10}(Re_x) - 0.65\right]^{-2.3} \quad \text{for} \quad Re_x < 10^9 \tag{3.51}$$

With this estimation of the skin friction coefficient, the wall-normal coordinate is determined. Re_x is based on the position on the chord of the wing, thus the estimated y+ will change over the chord. The height of the boundary layer can be approximated by [54]:

$$\delta_x = \frac{0.37x}{Re_x^{0.2}} \tag{3.52}$$

Goetten recommends a safety factor of 1.5 [21] on this δ_x value, due to the flat plate estimation.

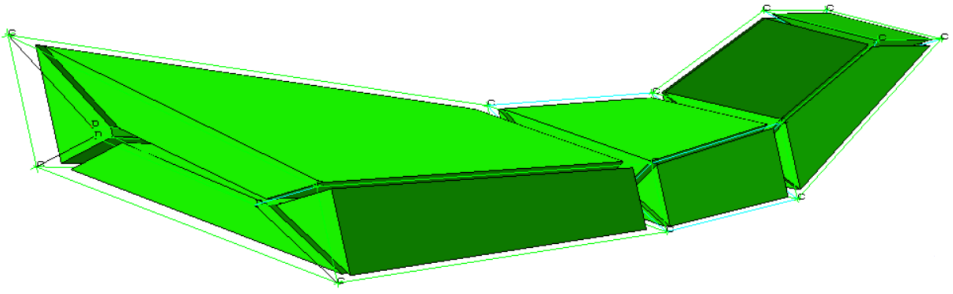

Figure 3.9: Blocking around the wing

Figure 3.9 shows the blocking around the Flying V wing. A similar structure extends to the spherical outer domain. The size of the blocking around the airfoil is chosen such that it is small enough to not have the small expansion ratio coming from the wall extend too long, but also create a smooth transition

without too much curvature to the outer blocking. This is a compromise between mesh quality and simulation cost. The wing is split up into three different blocking zones: outboard wing, inboard wing and wing-winglet junction. As the kinks in the wing coincide with the change in block zoning, the transitions lead to minimal skewness in the mesh elements. The blocks at the inboard and outboard wing are relatively straightforward as the geometry follows the general block size. The block around the winglet is relatively curved, as can also be seen in figure 3.10d. With a sufficiently large density of mesh elements, this curvature shouldn't lead to significantly skewed elements. The tip of the winglet has a block enclosing the three-dimensional geometry. This is a relatively critical block, as the small surface area of the winglet tip is expanded to the boundary. The curvature of the blocking lines is also relatively large here. Finally, these blocks require a smooth transition from the inner blocks to the boundary. Curves parallel to the inner blocks curving towards the boundary are constructed to facilitate this process. This naturally expands the size of the blocks, as seen in figure 4.5.

An O-mesh is the preferred option around the airfoil, as a blunt trailing edge is present in the Flying V parametrization. No singular point arises, which would occur with a sharp trailing edge combined with a C-mesh. The O-mesh will curve around the Flying V winglet (Figure 3.10), so special care is taken such that the curving of the mesh does not lead to excessively skewed elements.

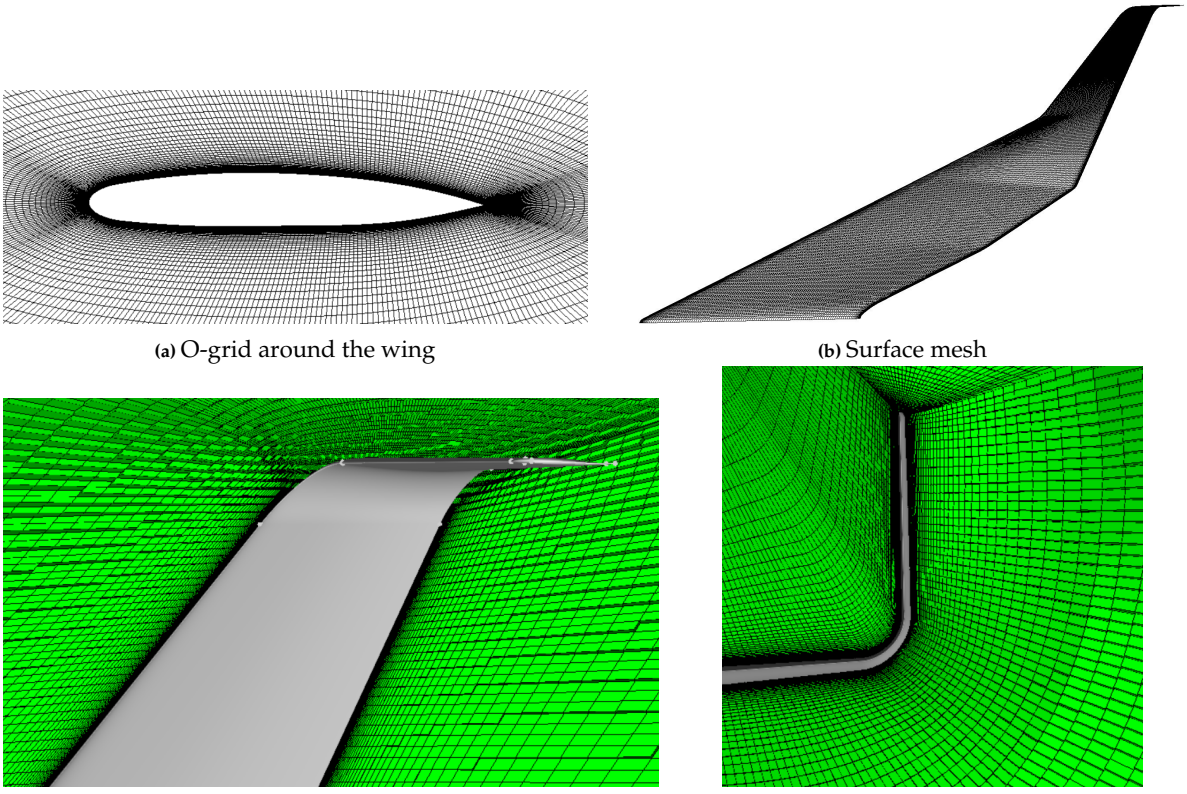

(a) O-grid around the wing

(b) Surface mesh

(c) Outboard wing, top view

(d) Outboard wing, front view

Figure 3.10: Mesh visualisation at 15 million domain nodes

Figure 3.10 visualizes the mesh. Figure 3.10a shows the O-grid at the root. The densification of the mesh towards the boundary is clearly visible. The node distribution parallel to the wall is constructed such that the wall and first node are as orthogonal as possible in the wall-normal coordinate. This bigeometric distribution also ensures a smooth transition between the leading/trailing edge and middle blocks. The mesh becomes significantly more dense at the trailing edge, as the continuity of a structured mesh requires the same number of nodes at the leading and trailing edge. The transition between inner and outer blocks is smooth, as it can not be distinguished in the picture. Figure 3.10b shows the surface mesh. As continuation is required, the mesh gets denser at the outboard wing. To better capture the curvature of the winglet, the spanwise mesh spacing is reduced at the wing-winglet junction. The increase in chordwise mesh density at the leading and trailing edge can also be seen.

3.4. Domain and Boundary Conditions

The computational domain is visualised in Figure 3.11. The domain is approximately 50 times the root chord of the airfoil to reduce artificial boundary errors, as recommended by Gotten [21]. A far-field pressure boundary condition is applied at the spherical boundaries, which approximates flow perturbations using the Euler equation Riemann invariants [1]. Non-slip boundary conditions are applied on the smooth half-wing. The no-slip condition is a Dirichlet boundary condition specifying 0 velocity at the wall. The wall is adiabatic. A symmetry condition is applied at the half-plane.

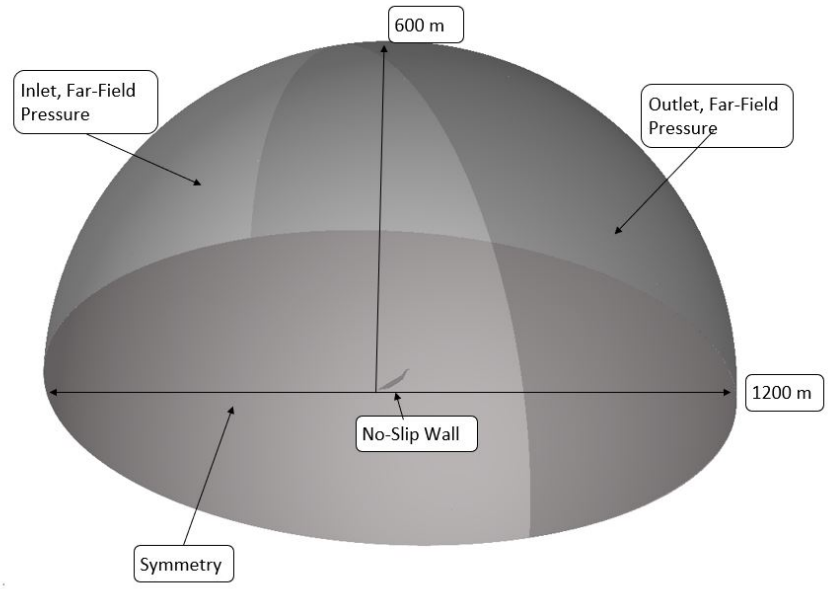

Figure 3.11: Grid computational domain with dimensions and boundary conditions

The Pressure Far-Field Boundary Condition aims to model a free-stream condition at infinity, with free-stream conditions specified (static pressure, Mach number, temperature, flow direction, turbulence parameters) [2]. This is classified as a characteristic boundary condition, as it uses characteristics to determine the flow variables[2].

The characteristics are based on Riemann invariants of a one-dimensional flow. Determining the eigenvectors of the Euler equations and setting up the integral curves of the characteristic family leads to the following two Riemann invariants (for subsonic flow) [9][2]:

$$\begin{aligned} R_\infty &= v_{n_\infty} - \frac{2c_\infty}{\gamma - 1} \\ R_i &= v_{n_i} + \frac{2c_i}{\gamma - 1} \end{aligned} \tag{3.53}$$

Where γ is the ratio of specific heats, c the speed of sound and v_n the normal velocity. Rearranging leads to:

$$\begin{aligned} v_n &= \frac{1}{2}(R_i + R_\infty) \\ c &= \frac{\gamma - 1}{4}(R_i - R_\infty) \end{aligned} \tag{3.54}$$

V_n and c are specified on the boundary. With V_n and c, the Riemann invariants are computed. Based on

the Riemann invariants, density, velocity, temperature, and pressure at the boundary face are computed [2]

Two equation models and the SA turbulence model are complete, they do not require input to compute boundary layer characteristics. They do need boundary conditions as a starting value of the transport equations. An often-used term is the turbulence intensity I, related to the magnitude of turbulence. For external free stream flows, the turbulence intensity is usually between 0.05 and 1 % [1].

$$I \equiv \frac{u'}{u_{avg}} \tag{3.55}$$

This turbulence intensity can be related to turbulence model transport equation variables, like k, ϵ, ω and μ_t.

$$k = \frac{3}{2}\left(u_{\text{avg}}\, I\right)^2, \tilde{v} = \frac{\mu_T}{\mu}\mu, \varepsilon = C_\mu \frac{k^2}{\frac{\mu_T}{\mu}\mu}, \omega = C_\mu \frac{k}{\frac{\mu_T}{\mu}\mu} \tag{3.56}$$

The turbulent viscosity ratio sets a certain eddy viscosity, based on the kinematic viscosity. The turbulence boundary conditions are set at 1 % turbulent intensity and a viscosity ratio of 10. As transition is not well predicted by the Menter SST model, these relatively high free stream values should ensure a realistic transition point.

3.5. Simulation Setup and Convergence Strategy

The flowfield is initialized using a hybrid initialization method, which couples a potential flow simulation with the boundary layer equations [1]. The simulation is started in first-order, as higher-order simulations require a good initial estimate, due to the dependence on higher-order terms. This is caused by the phenomenon illustrated by equation 3.57. With a decreasing element size, the higher-order terms dominate lower-order terms when a poor initial estimate of flow conditions is present. This leads to stability issues and possible non-convergence. A second strategy applied is underrelaxation of the time marching. A factor of 0.8 was found to be a good compromise between convergence and simulation cost.

$$\frac{\Delta^2\phi}{\Delta x^2}, \frac{\Delta^2\phi}{\Delta y^2} >> u\frac{\Delta\phi}{\Delta x}, v\frac{\Delta\phi}{\Delta y} \tag{3.57}$$

Next, the simulation is converged using the intended higher order scheme (3rd order MUSCL[1]), while progressively increasing the CFL number to speed up convergence. An implicit scheme is used to guarantee stability and reduce computational costs. The third-order MUSCL scheme was selected because of its stabilizing effect on shocks due to the flux delimiter present and because of its third-order nature. As it is predicted that shocks will play a large role in the flow phenomena of the simulation, the flux delimiter in the MUSCL scheme will decrease oscillations, with limited diffusive behaviour, as common with lower-order schemes. As the mesh is relatively dense, a third-order scheme should reduce the discretization error. Verification should show the influence of this third-order scheme.

The flux over cell boundaries is computed using the Roe Flux-Difference Splitting Scheme [51]. The highly compressible nature of the simulation is deemed to benefit from the Roe Flux-Difference Splitting Scheme approach of splitting up the fluxes in its characteristics. This should help reduce oscillations near shocks [51]. Gradients are computed using a least squares cell-based approach. Cell-based Green-Gauss can be a good option for structured meshes, but starts to decrease in accuracy when the mesh is skewed[1]. As a certain degree of skewness is present in the mesh, due to the leading edge sweep angle and curving of the mesh around the winglet, the slightly more expensive least squares cell-based approach is selected. The solving of the overdetermined system gives more accurate results for meshes with a less orthogonal orientation[1].

The low Reynolds Menter SST turbulence model is used for its good inner layer resolving qualities compared to the $k-\epsilon$ model [47]. In the transonic Flying V case, the Menter SST model was preferred over the Spalart-Allmaras (SA) model, as the SA model, even though it has been designed for transonic flow over wings, does not have much validation in the Reynolds number range of the Flying V, while

the Menter SST preserves more physical features [47]. An algebraic multigrid solver is used, in which corrections on coarse levels are performed using the finer grid levels to accelerate convergence speed, based on the work of [25]. This creates a close to linear relation between grid size and convergence speed [1].

The simulation is started at a CFL of 0.5 and in 5000 steps progressed to a CFL of 5. At this point a relatively stable solution is present and the CFL is ramped up in larger steps up to 200. A total of 15000 steps is required to converge the simulation. Convergence criteria are set at 1e-5 for the normalized flow criteria (continuity, velocity, energy, k, omega). The total cost of one simulation is estimated at around 2500 CPU hours.

The research will use ANSYS Fluent for the simulations and ANSYS ICEM for the meshing. ANSYS Fluent is a well-validated tool [1]. ANSYS ICEM is a tool especially suitable for structured meshes, which is the focus of this research. As the simulation is too large to run locally, the Aerospace faculty's high-performing cluster (HPC) is used for the simulations.

3.6. Optimization Workflow

At the start of the research project, reliability was identified as one of the key parameters of the project. As LES or DES simulations for this range of Reynolds numbers are infeasible, a high-fidelity RANS calculation is the preferred method of simulation. As the current parametrization consists of around 100 variables, a full gradient-based, algorithm-led optimization is deemed infeasible due to the associated costs. The research will apply a manual iteration approach, where physical insights dictate the direction of optimization. This approach offers an additional benefit by enabling a more direct consideration of trade-offs between aerodynamic improvements and potential volume and structural drawbacks.

As the centre of gravity can still differ in this conceptual stage, especially due to the placement of the engines, an important aerodynamic constraint is the proximity of the centre of pressure to the neutral point. With the centre of gravity in front of the neutral point, static longitudinal stability is assured, while minimizing trim drag. The requirement states: $(x_{np} - x_{cp})/MAC > 0.02$. The centre of pressure is an output of the simulation software. The aerodynamic centre is estimated using equation 3.58[29]. At least two angle-of-attack computations are required for this estimation, but linear regression can be used with multiple measurements to increase accuracy. Non-linearities due to the compressible nature of the flow might complicate the estimation of the neutral point.

$$\frac{x_{np} - x_{ref}}{c} = \frac{x_{ref}}{c} - \left(\frac{\partial C_{M_{ref}}}{\partial C_L} \right) \tag{3.58}$$

The simulation workflow is visualised in Figure 3.12. The first step is to analyse the results and implement changes in the CAD model. As the design of the Flying V is highly coupled, it is checked if the proposed aerodynamic changes leave sufficient volume/dimensions in the wing section and if the structural changes are acceptable (stage 3). The inboard wing is constrained by its dimensions and volume, which is required to carry passengers/cargo. The outboard wing is characterized by thickness-to-chord ratio constraints of 10% and 8 % at the respective root and tip sections. The output of stage 2 serves as the input for the meshing and solver input (stage 4). The blocking of the structured mesh is reassigned, such that the iterations have similar meshes. Again the mesh criteria are checked and the node distribution is slightly altered to take into account the changed geometry. The resulting Fluent case serves as input for the aerodynamic solver (stage 5), run on the HPC. This step normally requires 2 iterations to get the right lift coefficient. The lift slope changes slightly between the iterations, such that usually the estimated lift coefficient of the second iteration agrees with the estimated required angle of attack. Stage 6 consists of the post-processing of the simulation data. ANSYS CFD-POST is used to generate visual data and to export data of wing section 2.5m apart to a csv file. A python script is used to translate this data into pressure, lift and drag distributions. The lift and drag distributions are calculated based on pressure and skin friction coefficient of section elements. Finally, the neutral point and centre of pressure constraint is checked.

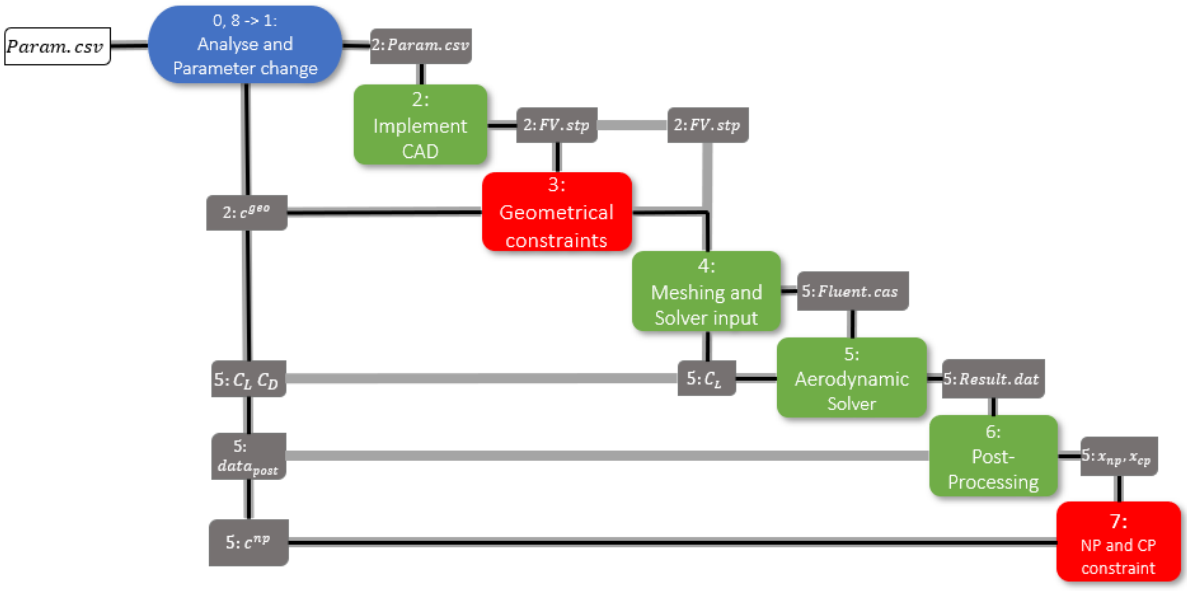

Figure 3.12: The research's optimization workflow

3.7. Two-Dimensional Optimization

As the inboard wing is composed of many parameters, described in section 3.1, this parametrization allows for detailed changes of the inboard wing profiles. The outboard wing profiles are described by the CST coefficients of an airfoil and its incidence angle. An optimized outboard wing profile is thus highly dependent on the airfoil shape. Well-validated, open-source airfoils in the M = 0.85 regime, with the right design section lift-coefficient and thickness-to-chord ratio are scarce. A gradient-based, algorithm-led optimization of these airfoils can help improve the performance of the outboard wing considerably. As a full-scale, three-dimensional optimization is deemed infeasible due to its cost, a two-dimensional optimization of these sections can improve the design of the three-dimensional wing. For a high aspect ratio wing the flow away from the root and tip can be partly considered two-dimensional [29].

It should be noted that the sweep of the outboard wing will introduce cross-flow, limiting the two-dimensional nature of the flow. The relatively low aspect ratio of the outboard wing (AR = +/-3) will also reduce the dominance of two-dimensional features. Interference with the inboard wing and winglet influences the performance of the three-dimensional wing. Despite these limitations, a two-dimensional optimization can still be a cost-effective way of increasing the outboard wing efficiency, as other airfoils will not be optimized for the wing's conditions.

Both the root and the tip airfoil are optimized, as the wing is interpolated between these two airfoils. The design lift coefficient is based on the optimal lift distribution found in the three-dimensional manual optimization. The airfoil is discretized using 12 Class and Shape functions (CST) coefficients. CST functions are an efficient way of parameterizing airfoil shapes, as they allow for a relatively large amount of design freedom, without being prone to significant parameterization errors [11]. The shape of the airfoil is determined by a combination of a class function, C(x/c), a shape function, S(x/c) and a term taking into account the trailing edge thickness (equation 3.59 [11]). The class function (equation 3.60 [11]) determines the general shape, where for an airfoil N1 = 0.5 and N2 = 1. The shape function determines the more detailed features of the y/c distribution. Kulfan and Bussoletti [31] proposed the use of Bernstein polynomials for the shape functions. The CST coefficients represent the contribution of every Bernstein polynomial used.

$$\frac{y}{c} = C\left(\frac{x}{c}\right) S\left(\frac{x}{c}\right) + \frac{x}{c}\frac{\Delta z_{te}}{c} \tag{3.59}$$

$$C\left(\frac{x}{c}\right) \equiv \left(\frac{x}{c}\right)^{N_1} \left[1 - \frac{x}{c}\right]^{N_2} \tag{3.60}$$

The two-dimensional Navier-Stokes equations (equation 3.2) are used to estimate the aerodynamic performance of the airfoil. The computational mesh is automatically generated for each iteration. The Mesh generation algorithm is based on the mesh-generation toolbox created by Hofer [24]. The toolbox is however intended for internal flows. The toolbox was altered to allow for a significant increase of the boundary size, to allow far-field boundary conditions. This required a change in the part of the algorithm that calculates the transition of mesh parts. This is now based on the y+ and boundary box size to ensure smoothness. The bigeometric growth rates on the outer mesh blocks are replaced by geometric1 growth rates to ensure a continuous growth of cell size of 1.3 towards the boundary. A mesh density factor was introduced to allow for an easy densification of the mesh. This increases the number of nodes evenly over the mesh and increases/decreases the growth rates of cells.

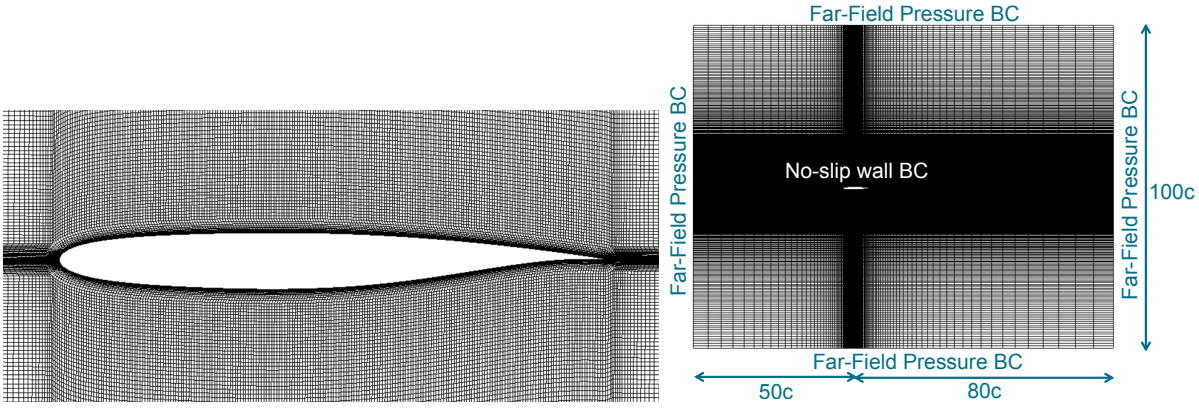

(a) Visualisation of the mesh around the airfoil

(b) Simulation domain and boundary conditions

Figure 3.13: Mesh visualisation at 140,000 cells

The domain is split up into an outer blocking and a blocking at the airfoil, allowing the setting of boundary layer mesh characteristics. The mesh consists of an O-mesh in the blocking at the airfoil wall and an H-mesh in the outer blocking, as seen in figure 3.13b. The y+ value is kept below 0.5, with a growth rate of 1.2. The H-mesh in the outer blocking allows for a rectangular domain, which decreases the chance of error in the meshing process due to its simplicity. A downside of the rectangular domain is the streamlines that can enter and leave the straight boundaries in near proximity, something that is avoided in circular meshes. A large domain size (130c x 100c) is chosen to limit this streamline interference. At this size, there is no change observed in lift and drag coefficient when the domain size is increased further. The dense mesh near the airfoil leads to blocks with a relatively high aspect ratio near the boundaries orthogonal and parallel to the airfoil. This however should not affect the performance of the solver, as the velocity gradients in the outer region are minimal [59].

The discretization/simulation options are kept similar to the 3D simulation. The implicit, density-based solver is used due to the transonic nature of the flow. This solves the NS-equations (continuity, momentum, energy) in a coupled way. The flux over cell boundaries is computed using the Roe Flux-Difference Splitting Scheme [51] and gradients are computed using the least square-based approach [1]. As shown in figure 3.14, the third-order MUSCL scheme showed a large dispersive error, which was not occurring in 3D. Therefore the second order upwind scheme is used. As a potentially large number of iterations will be performed, the Spallart-Allmaras [57] turbulence model is preferred over Menter SST [36]. This reduces the cost of the simulation as only one transport equation is used to compute the eddy viscosity. A hybrid initialization is used to generate the initial flowfield. The algebraic multigrid solver is used to solve the system of equations.

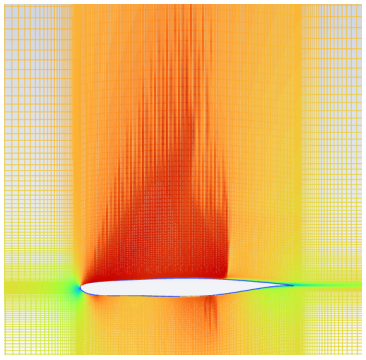

Figure 3.14: Dispersive error in the simulation using a 3rd order MUSCL scheme

Matlab's fmincon function is used to facilitate the optimization process. The initial design vector consists of the 12 CST coefficients of the NACA SC(2)-0610 airfoil [22]. This airfoil has the target thickness-to-chord ratio of the root airfoil and a slightly higher design lift coefficient. The experimental drag divergence Mach number lies around M=0.8, lower than the design conditions of this optimization. The lift coefficient is however lower than the design condition of the NACA airfoil. This should partly compensate for the higher Mach number. The optimizer should find a way to reduce compressibility losses stemming from these design conditions.

Matlab's sequential quadratic programming (SQP), based on the work of Powell [48], is used. Its ability to handle large-scale problems, while being a Medium-Scale algorithm, thus saving on memory requirements, which can be important on the HPC, makes it a good choice [26]. Furthermore, the SQP algorithm can handle non-linear constraints well [26]. The possibility of non-convergence of the CFD simulation requires a good way to handle these artificial non-linearities.

The SQP algorithm aims to find the minimum of equation 3.61 [48]. F(x) represents the objective function, λ_i the Lagrange multiplier and $g_i(x)$ the constraints. The Lagrange multiplier is introduced to incorporate constraints into the objective function. A second-order Taylor expansion around the current iteration linearizes the non-linear constraints. This expression is known as the Quadratic Programming (QP) Subproblem and is minimized using an active set strategy [26]. The solution for the subproblem gives a search direction. The current iterations and lagrangian polynomials are subsequently updated [48] (equation 3.62).

$$L(x, \lambda) = f(x) + \sum_{i=1}^{m} \lambda_i \cdot g_i(x) \tag{3.61}$$

$$x_{k+1} = x_k + \alpha_k d_k \tag{3.62}$$

Figure 3.15 shows the workflow of the optimization. The optimizer has 12 design variables, the CST coefficients. These coefficients are passed to the Geometry and mesh tool. This tool first converts the CST coefficients to Cartesian coordinates and checks whether the geometry is valid (No overlapping). The geometry is built up in ICEM, the appropriate y+ value is calculated and the mesh spacing is assigned. Finally, the tool exports the generated mesh to a Fluent mesh. The Aerodynamic solver runs the CFD calculation and outputs the lift coefficient, drag coefficient and minimum pressure coefficient. The objective function outputs the lift-to-drag ratio and makes sure the simulation is converged by checking the convergence criteria history.

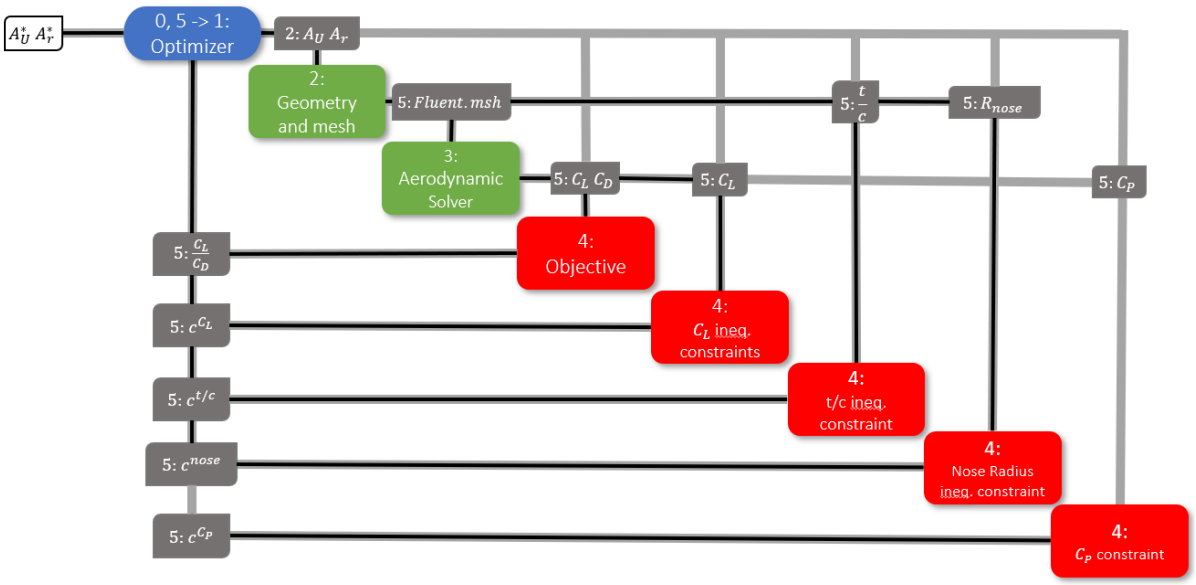

Figure 3.15: Workflow chart of the two dimensional airfoil optimization

Four different constraints ensure the validity of the designed airfoil. These constraints are described in table 3.1.

Constraint	Wing Root	Wing tip	Description
c_l ineq.	0.55>c_l>0.48	0.6>c_l>0.52	The section lift coefficient should be in an acceptable range, based on the lift distribution on the Flying V outboard wing
t/c ineq.	t/c >0.1	t/c >0.08	This is a high level requirement, based on structural mass of the wing and low speed characteristics
R_{nose} ineq	R>0.025c	R>0.02c	The nose radius should not be too small, as this leads to large suction peaks at higher angles of attack
C_p ineq	C_p >-0.85	C_p >-0.85	A pressure coefficient of -0.85 relates to a Mach number of 1.3. These speeds shouldn't be surpassed as buffeting could start to occur [43].

Table 3.1: Inequality constraints of the 2D optimization of the airfoil

3.8. Design Principles

The last section of the Methodology focuses on the physical design principles of transonic wings. The manual iteration approach requires an understanding of the basic principles, such that based on observed behaviour, appropriate design changes can be made. This section tries to summarize the most important principles.

3.8.1. Compressibility Effects on Pressure

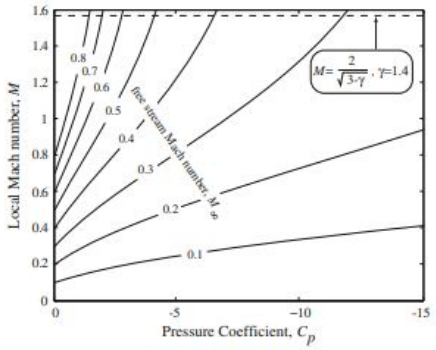

Figure 3.16: Effect of free stream Mach number on local Mach number increase [64]

From the isentropic relationships, figure 3.16, can be constructed [64]. It shows the effect compressibility has on the rise in local Mach number. When increasing the free stream Mach number the local Mach number, based on a certain pressure coefficient, rises sharply. Another effect important for transonic aircraft is that the region of influence increases with increasing Mach number. Streamlines further away from the body are affected with increasing Mach number.

An important concept in transonic design is the critical Mach number (M_{crit}) and the critical pressure coefficient ($C_{p_{crit}}$), where sonic flow first appears on an airfoil. Equation 3.63 shows the relation between $C_{p_{crit}}$ and M_{crit} [64]. With compressibility corrections, the critical pressure coefficient and Mach number can be estimated, based on the incompressible $C_{p_{min}}$

$$C_{P_{\text{crit}}} = \frac{2}{\gamma M_{\text{crit}}} \left[\left(\frac{1 + \frac{\gamma-1}{2} M_{\text{crit}}^2}{\frac{\gamma+1}{2}} \right)^{\frac{\gamma}{\gamma-1}} - 1 \right] \tag{3.63}$$

The drag divergence Mach number, M_{dd}, is often defined as the Mach number where gradient $\partial C_d / \partial \text{M}$ reaches a value of 0.1 [65]. At this point, strong separation starts to occur and the lower side of the airfoil is in near supercritical condition. Increasing the Mach number further will also lead to a significant loss in lift [65].

3.8.2. Interaction of Shock Wave and Boundary Layer

One of the characteristic behaviours of transonic flows is shock waves. As the no-slip condition has to be satisfied at the wall, the shock wave will not propagate through the entire boundary layer, but interacts with it.

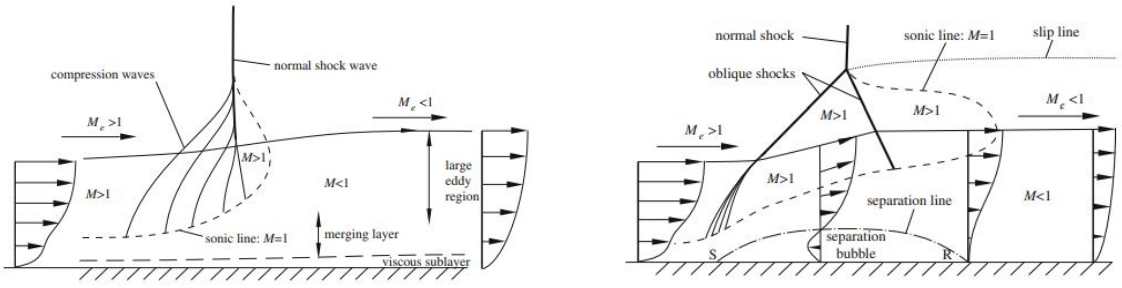

(a) Weak interaction of a shock wave and boundary layer

(b) Strong interaction of a shock wave and boundary layer

Figure 3.17: Interaction of shock wave and boundary layer [64]

Figure 3.17a shows the *weak interaction* between shock wave and boundary layer. The shock wave does

not extend into the boundary layer, but is instead formed by a series of compression waves. The outer flow experiences a large pressure gradient in the shock, which would lead to separation in the boundary layer. The boundary layer, however, encounters a significantly smaller pressure gradient due to a series of compression waves. The shock wave interaction thickens the boundary layer, increasing the shape factor and decreasing the skin friction coefficient [64].

In a *strong interaction* the shock wave itself descends further into the boundary layer. Due to the large pressure gradient closer to the wall, the flow separates at point S, forming a separation bubble. This in turn causes a strong streamline curvature, leading to the compression waves that form the oblique shock in the first place. A second oblique shock is formed to turn the flow back to the wall direction. The shocks merge in the triple point, where the shock becomes normal (or slightly oblique). At the second oblique shock, the streamlines expand, aiding the reattachment of the flow. The boundary layer is now prone to separation and when increasing the shock strength further, the flow can fully separate at the shock foot [64].

Wave Drag

Wave drag is the drag originating from shock waves. Shock waves both transfer energy from the flow to the outer region, of which the loss of energy can be seen as drag and when strong enough, can cause shock-induced separation, leading to large pressure losses.

$$\frac{D_w}{q_0} \approx \int_0^1 \int_0^1 S''(x)S''(\xi) \log \frac{1}{x-\xi} \mathrm{d}x \, \mathrm{d}\xi \tag{3.64}$$

For a non-lifting body, the Whitcomb area rule, named after Richard Whitcomb, states that the wave drag of a certain mostly depends on the cross-sectional area distribution of that body. Equation 3.64 [44], representing the wave drag of a certain body, shows it depends on the second derivative of the area of that body.

3.8.3. Interference Drag

When two bodies are in each other's vicinity, they can mutually interfere, increasing supervelocities and increasing drag. This phenomenon is known as interference drag. The merging of boundary layers can also lead to separation.

The sharper the intersection between certain bodies is, the higher the supervelocities become. One way of reducing the supervelocities and avoiding undesirable boundary layer merging is the creation of a fillet to smoothen out the transition.

In transonic flow, these phenomena are magnified. The region of influence of a body is larger and shockwaves can occur due to interference. When these shock waves lead to separation, the drag-divergence Mach number can be affected [64]. In transonic aerodynamics, area ruling can lead to a good fairing design, minimizing interference.

3.8.4. Two Dimensional Transonic Features

In high aspect ratio wings, sections of the wing can be approximated in a two-dimensional way, as two-dimensional effects dominate the flow phenomena [64]. In aircraft design, this leads to the well-known airfoil, of which the design is critical in wing design. Basic airfoil theory is assumed to be known to the reader, thus this section will focus on transonic airfoil design.

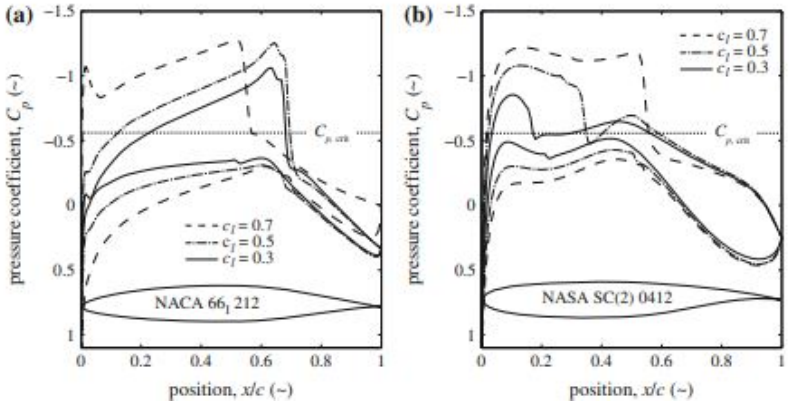

Figure 3.18: Comparison of 6 digit NACA and transonic airfoil[64]

Traditional airfoils start creating strong shock waves in transonic conditions. Therefore in the 1950s a new generation of transonic airfoils, called supercritical airfoils, was designed under the supervision of W.T. Whitcomb [64]. Figure 3.18 compares supercritical airfoil SC(2) 0412 with a Natural Laminar Flow (NLF) airfoil. The Mach number on the supercritical airfoil's upper side is kept within limits, leading to reduced shock strength. A portion of the lift is created by the concave surface at the TE of the lower side. This phenomenon is called *aft loading* [64]. This section of the lower surface often follows a curvature according to the Stratford criteria [22] and supersonic flow should be avoided here. The supercritical airfoil delays shock-induced separation to significantly higher Mach numbers. Most important for the M_{dd} are the thickness-to-chord ratio and design lift coefficient. The following empirical relation is given for supercritical airfoils [64]:

$$M_{\mathrm{dd}} + t/c + 0.10c_l^{1.5} = M^\star \text{ with } M^\star = 0.935 \tag{3.65}$$

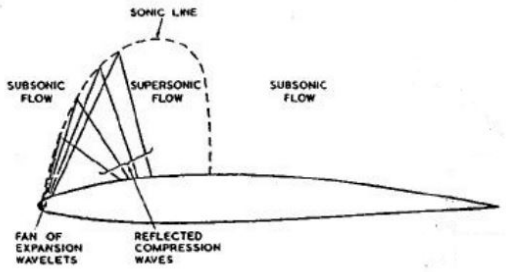

Figure 3.19: Compression and expansion waves on a supercritical airfoil[43]

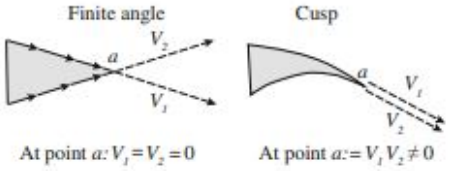

Figure 3.20: Trailing edge shapes[64]

In the design of the upper surface of supercritical airfoils compression and expansion waves are balanced such that a relatively flat pressure distribution arises, with some isentropic recompression [43] (figure 3.18 and 3.19). This reduces the shock strength, while keeping the boundary layer stable. Two main factors come into play: the upper surface curvature and nose radius. The nose radius of a transonic airfoil is normally relatively large, to allow for a rapid expansion of the flow. This in turn allows for the expansion waves to be reflected back as compression waves [43]. The curvature on the upper side should be restricted to reduce the strength of the expansion waves originating from the surface [43]. The combination of upper surface curvature and nose leading edge design should be such that the coalescence of compression waves does not lead to a strong shock, but a weak one [64]. This design does lead to a strong pressure peak in subcritical conditions [66].

Another feature of transonic airfoils is the slight plateau in pressure distribution right after the shock (figure 3.18). This plateau allows for the mixing of the boundary layer, before being subjected to the

adverse pressure gradient, making it more separation resistant [66]. The pressure plateau, at sonic speeds, also stops disturbances from moving upstream, decreasing shock wave strength [22]. This is realized by an increase in curvature after the design shock position.

The trailing edge of transonic airfoils is also an important design parameter. Transonic airfoils are characterized by strong adverse pressure gradients [64]. Altering the trailing edge by means of a cusp or bluntness can decrease this pressure gradient. The cusp, as shown in figure 3.20, allows for the (theoretically inviscid) trailing edge velocity to be larger than zero, reducing the pressure at the trailing edge. Structurally, this solution is questionable. A blunt trailing edge can help alleviate some of the loads. A blunt trailing edge can also be aerodynamically advantageous, as the separation zone, which does increase base drag, can allow for some of the surface pressure recovery, relieving the adverse pressure gradient [64]. This effect is mainly seen in a TE thickness around 0.7% c [22].

Several transonic airfoil designs aim to remove the shock altogether. Shock-Free airfoils are carefully designed, such that compression waves do not intersect and the flow is compressed isentropically [64]. In practice, these airfoils are rarely used due to their sensitivity to external conditions. Another approach is to keep the Mach number close to its critical condition (M=1), known as sonic rooftop airfoils. This also avoids shocks, but leads to thin structures. These are used in practice, like on the Airbus A300B [64]. Advantages of supercritical airfoils over sonic roof-top airfoils are a larger relative thickness, larger possible wing loading and a larger leading edge radius, improving $C_{L_{max}}$ [43].

The **Reynolds number** has a significantly stronger effect in transonic airfoils than in subsonic [43] for two reasons:

- When the boundary layer is still laminar up to the shock, a lambda shock is likely to form, not penetrating the boundary layer. A turbulent boundary layer is more likely to interact with a normal shock, increasing the likelihood of separation [43].
- Increasing the Reynolds number decreases the displacement thickness, increasing effective curvature. This moves the shock aft, increasing shock strength and adverse pressure gradient [43]. This also increases the negative pitching moment. More momentum is concentrated near the wall, thus the boundary layer does become less prone to separation.

3.8.5. High-Speed Stall and Buffeting

When shock strength becomes strong enough to cause separation, aerodynamic vibrations become a likely occurrence. This phenomenon is known as high-speed buffeting. High-speed stall is therefore characterized by buffeting. The onset of high-speed buffeting is caused by the separation bubble at a shock reaching the trailing edge [43]. Buffeting can have fatal consequences, so certification demands a design lift coefficient 30% below the buffeting onset lift coefficient for any Mach number [64].

3.8.6. Three Dimensional Transonic Features

So far two methods reducing wave drag and transonic effects have been discussed: airfoil design and area ruling. The third way to reduce wave drag is wing sweep. By sweeping the wing, the section in the flow direction changes. This apparent thinner section is more suited for higher Mach numbers. By applying sweep, instead of reshaping the section itself, major structural penalties and reduced fuel storage are avoided [64].

Wing Sweep Theory

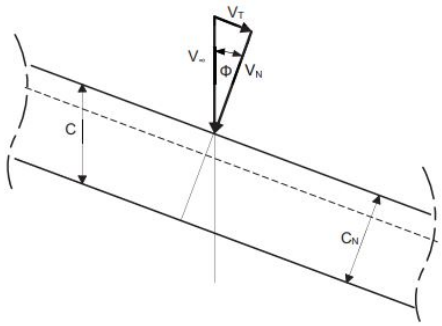

Figure 3.21: Wing sweep angle[65]

Wing sweep theory is based on an infinite swept wing, without taper ratio. The free stream velocity can be decomposed into two components: a vector tangential and a vector normal to the leading edge of the wing, V_N and V_T. Relating the change in velocity to the lift formula leads to the following relations [65]:

$$C_{p,N} = C_p \cdot \frac{1}{\cos^2 \varphi} \tag{3.66}$$

$$C_{l,N} = C_l \cdot \frac{1}{\cos^2 \varphi} \tag{3.67}$$

$$\alpha_N = \alpha \cdot \frac{1}{\cos \varphi} \tag{3.68}$$

Swept Wing Aerodynamics

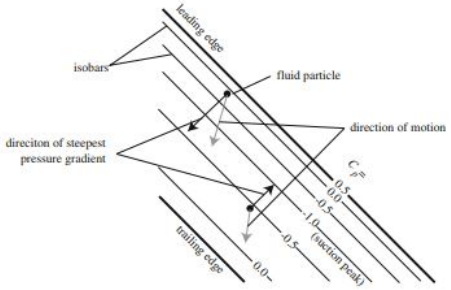

Figure 3.22: Pressure gradients on a swept wing [64]

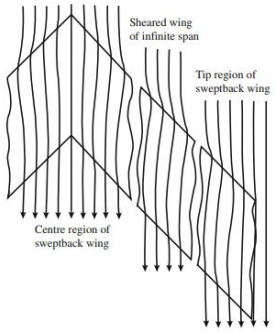

Figure 3.23: Flow pattern on a swept wing [64]

Wing sweep theory does, however, not represent the real flow phenomena on the wing. Figure 5.14 [64], shows the flow direction, aligned with the freestream flow and the direction of steepest pressure gradient, aligned with the airfoil shape normal to the leading edge. These pressure gradients influence the inviscid streamlines. A favourable pressure gradient will direct the flow inwards, an adverse pressure gradient outwards [64]. Figure 3.23 shows the s-shaped path effect this has on a swept wing.

Wings are, however, finite. The root and tip influence the flow behaviour of the wing. As the centre of a swept wing is at a different longitudinal position, than the root and tip, the wing effectively generates upwash on itself. For an aft-swept wing, this increases the angle of attack towards the tip, as shown in figure 3.24.

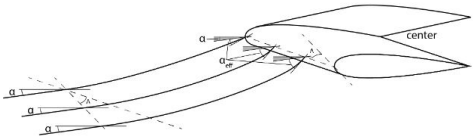

Figure 3.24: Induced angles of attack on a swept wing[43]

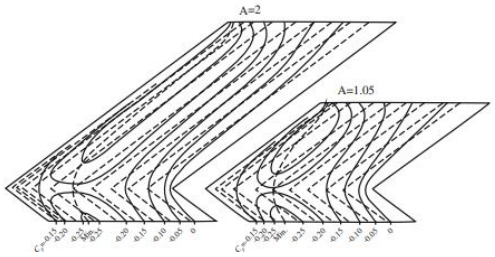

Figure 3.25: Pressure isobars of a swept wing[64]

At the root of the airfoil, due to a symmetry condition of forces, the isobars of both wing parts have to align in a tangential manner, as shown in figure 3.25. This *root effect* shifts the suction peak more aft and reduces the magnitude of the suction peak. Also, a stronger adverse pressure gradient is present. The suction on the aft part of the airfoil results in a net drag effect [64]. At the tip, the isobars curve forward, influenced by the three dimensional flow field [64]. This in turn shifts the suction peak forward and increases its strength.

These phenomena can be counteracted by taking these phenomena into account in airfoil and planform design. At the root, the camber can be decreased, position of maximum thickness moved forward, the incidence angle can be changed and the thickness of the wing increased to create similar pressure distributions and realign the isobars. Due to the larger chord at the root, given the taper ratio, these modifications might lead to too much lift inboard for an elliptical distribution. The increase in lift can be negated by changing the thickness distribution of the lower side of the airfoil [43].

At the tip, opposite measures can be taken to reduce tip effects. Moving the position of t/c_{max} aft has negative consequences for stall behaviour due to the sharpening of the nose [64]. Modifying the 3D geometry, like the introduction of a Küchemann tip [64] can help realign isobars.

Viscous Effects

The misalignment of pressure gradient and flow direction, as seen in figure 5.14, has a profound effect on another part of the flow: the boundary layer. This low-momentum part of the flow has a relatively larger streamline deflection than the inviscid part of the flow [64]. The direction of this cross-flow component depends on the pressure gradient of the inviscid part of the flow.

Figure 3.26: Boundary layer cross-flow on wind tunnel model [64]

Figure 3.26 shows the effect cross-flow has on a transonic wing featuring an outboard shock-wave. Cross-flow can be seen from the root onwards. Due to the large pressure loss at the shock wave,

cross-flow is amplified towards the tip. The larger distance this boundary layer has travelled, together with the lower Reynolds numbers at the tip due to the taper ratio, lead to the tip being more prone to flow separation [64]. Tip stall in a swept wing can change the neutral point of the aircraft, resulting in a pitch-up moment. To increase the $C_{L_{max}}$ and to keep the aircraft safe, design implications are required to postpone tip stall. At the root, the wing becomes resistant to separation, because of the cross-flow thinning of the boundary layer [43].

Another phenomenon of swept wings is instabilities that promote transition. Where in a flat plate Tollmien-Schlichting waves are dominant, in a swept wing attachment-line instabilities, cross-flow instabilities and centrifugal instabilities start playing a role [64]. In a swept wing the attachment line is not a stagnation point, but the flow moves parallel to the leading edge. Interaction with disturbances here can lead to early transition, known as attachment-line instability [64]. A second cause for instabilities is cross-flow instability. The inflection point in the cross-flow direction leads to cross-flow vortex structures, which when breaking down can cause transition. This depends on the turbulence levels of the flow and roughness of the walls [64]. Finally, centrifugal instabilities, occurring when a curved streamline increases in r but decreases in $|rV|$ causing streamline vortices, are also transition mechanisms.

Design Considerations on Finite Wings

Obert [43] summarizes the design considerations for a finite wing in the following way

- **Maximum local Mach number at each wing station** The local Mach number should not exceed 1.2 to prevent excessive drag creep. Boundary layer separation occurs between a local Mach number of 1.35 and 1.45, depending on shock position and Reynolds number [43].
- **Aft pressure gradient** The position of the shock should not be too much aft to avoid a too strong pressure gradient and trailing edge separation [43]
- **Spanwise lift distribution** An elliptical lift distribution should be obtained, with near straight pressure isobars [43]
- **Pitching moment coefficient** The pitching moment coefficient should be reasonable. As the outboard wing of a tapered wing has a larger wing loading, the moment coefficient on the inboard wing can be more easily reduced [43].

4

Verification and Validation

Verification and Validation are an integral part of any simulation-based optimization process to guarantee the reliability of the simulations. Tu et al. [59] describe verification as the degree to which the model does what the user developed it to do and validation of the degree to which the model agrees with reality. This chapter presents the verification, consisting of a grid convergence study, model uncertainty quantification, grid quality study, validation of the simulation method and verification and validation of the two-dimensional optimization numerical setup.

4.1. Verification

Verification aims to quantify the discretization error and uncertainties in the simulation. This is done in three parts: a grid convergence study, model uncertainty quantification and grid quality study.

4.1.1. Grid Convergence Study

A grid convergence study aims to determine the ordered discretization error of a set of simulations. The temporal and spatial discretization errors should converge to zero asymptotically, as the grid and timestep are refined. The goal of the study is to estimate the perceived order of the method and determine a suitable number of grid cells at which the simulation can reliably be run, while minimizing the simulation costs. The NPARC verification procedure is followed [42], of which the methods are largely based on the book by Roach [50]. Richardson extrapolation [50] can be used to estimate the order of the method. This requires three solutions in the asymptotic range of convergence on three different grid spacings. With the order of convergence of the simulation known, the required number of grid cells can be estimated based on a required grid convergence index (GCI), which gives an indication of the magnitude of the normalized discretization error (equation 4.2). F_a represents a safety factor, ϵ is the relative error, r the grid refinement ratio and p the order of convergence of the method.

$$\frac{f_3 - f_2}{r_{23}^{p_o} - 1} = r_{12}^{p_o} \left(\frac{f_2 - f_1}{r_{12}^{p_o} - 1} \right) \tag{4.1}$$

$$\mathrm{GCI}_{fine} = \frac{F_a |\epsilon|}{(r^p - 1)} \tag{4.2}$$

$$r^* = \left(\frac{\mathrm{GCI}^*}{\mathrm{GCI}_{23}} \right)^{1/p} \tag{4.3}$$

The first three runs which showed to be in the asymptotic region are the runs of 1M, 2.5M and 5M nodes. Using equation 4.1 [42], the perceived order of spatial convergence is estimated to be 3.5. This is reasonably close to the 3rd order MUSCL method that is used as the spatial discretization scheme in the simulation. As refining a grid consistently in a structured mesh is relatively hard, as nodes are specified by the user in each block or subsection of the simulation domain, some inconsistency in the perceived order of convergence is expected.

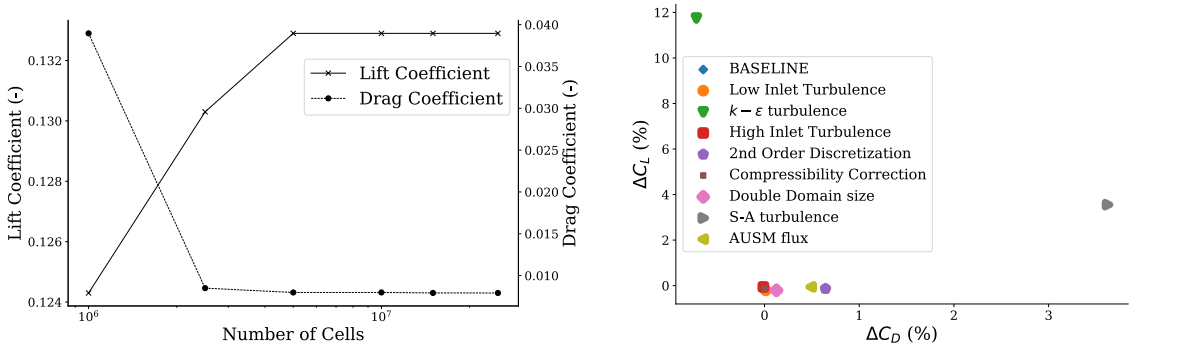

(a) Flying V baseline wing mesh convergence study

(b) Flying V sensitivity study (Baseline: C_L=0.26, C_D=122 drag counts

Figure 4.1: Flying V Mesh convergence and sensitivity studies

The 5 million nodes mesh gives a GCI of 0.8%. Based on the examples and guidelines given in [42] and [50], together with the focus on reliability in the thesis project, a GCI of 0.01% is deemed acceptable, corresponding to a mesh density of 15 million nodes. The computed GCI from the simulated case is 0.0092%, thus acceptable. The reason for this relatively low GCI lies in the fact that this thesis will focus on manual optimization steps, instead of having an optimizer exploring the design space. This leads to a significantly reduced number of total simulations performed and allows for stricter requirements on the accuracy of the simulation, especially in this complicated fluid domain. Figure 4.1a shows the full spatial convergence study.

4.1.2. Model Uncertainty Quantification

As the simulation depends on a number of assumptions and model choices, it is important to quantify the effect these choices have on the simulation results. Figure 4.1b shows the percentage difference between the simulation options. Table 4.1 explains the parameters explored.

Index name	Uncertainty	Specifics
$k-\epsilon$ turbulence	Turbulence model	Realizible $k-\epsilon$ turbulence model, including a wall model
S-A turbulence	Turbulence model	Spalart-Allmaras vorticity based turbulence model
Compressibility Correction	Turbulence model	Menter SST turbulence model with a compressibility correction
Low Inlet Turbulence	Turbulence model	Low intensity turbulence inflow conditions
High Inlet Turbulence	Turbulence model	High intensity turbulence inflow conditions
2nd Order Discretization	Discretization scheme	Second order upwind scheme
AUSM flux	Discretization scheme	AUSM flux type
Double Domain size	Domain	Size of the domain doubled for artificial boundary influence

Table 4.1: Uncertainty parameters

Figure 4.1b shows a relatively large dependence on the turbulence model used. The $k-\epsilon$ results can be questioned, as the high Reynolds model, in combination with a wall model might not perform well near the wall in complicated flows [67]. The 3-4% difference in results of the Spalart-Allmaras model should be considered as an uncertainty margin. This is quite a significant margin based solely on the turbulence model. The other model choices show a smaller impact on simulation results. Using a second-order scheme changes the drag coefficient by approximately 0.7%. This is relatively close to the baseline. A second-order scheme is expected to have a slightly higher discretization error. The AUSM flux splitting scheme shows similar behaviour. The AUSM splits the flux into convective and

pressure parts and based on this calculates the flux between two cells [1]. A small difference with the Roe flux splitting scheme was expected. Finally, it can be concluded that the domain is large enough, as increasing the domain size has limited influence on the simulation results. The inflow turbulence has limited influence on the results, presumably because the turbulence is dissipated due to the large domain once it reaches the airfoil.

4.1.3. Grid Quality

Simultaneously to the grid convergence study, the quality of the generated meshes has to be ensured. Especially while refining a mesh, erroneous elements can cause instability, non-convergence and a higher cost of simulation. An overall poor-quality mesh can lead to unreliable results. A certain number of objective grid quality parameters can be set up to evaluate the quality of the mesh. The mesh quality criteria in a hexahedral structured mesh differ from the criteria of a tetrahedral unstructured mesh due to the nature of the orientation of the cells [9]. The lack of gradients in a certain region can make larger aspect ratios numerically acceptable, just like a lack of pressure gradient in the y direction makes the large aspect ratios near walls acceptable [21]. Thus in areas aligned with the flow, sufficiently away from the body, larger aspect ratios are not likely to cause convergence issues. Tetrahedral unstructured meshes are far less likely to align with the flow compared to hexahedral structured meshes. The Flying V mesh, for example, aims to save computational cost by increasing the aspect ratio near the domain boundary, as shown in figure 4.5. This saves cells in the boundary normal direction.

Three important indications of a good structured mesh are the determinant [3] indicating the quality of a cell, the minimal or skew angle [21], indicating the orientation of the cell and the y^+ value, important for the turbulence model[47].

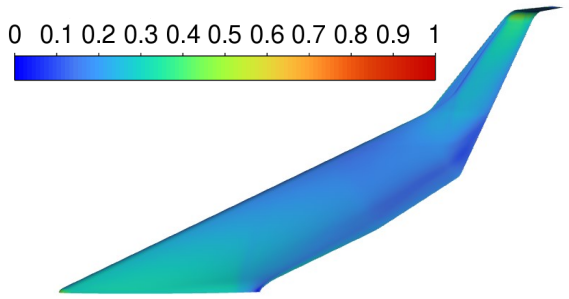

Figure 4.2: y^+ distribution on the upper surface of the Flying V half wing (Mach =0.85, Re = 88.3 million, C_L = 0.26)

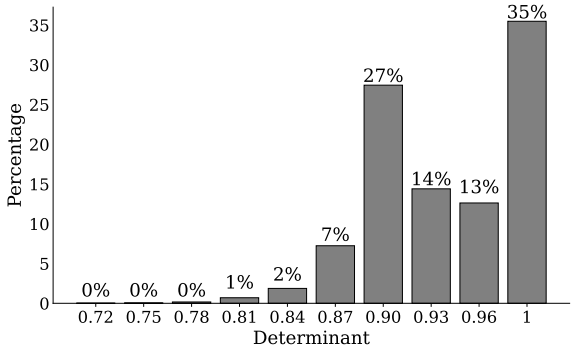

Figure 4.3: Flying V mesh determinant distribution

$$y^+ = \frac{y u_\tau}{\nu} \tag{4.4}$$

Figure 4.2 shows the y^+ distribution on the wing. The y^+ parameter (equation 4.4) normalizes the wall-normal coordinate with respect to the friction velocity ($u_\tau = \sqrt{\frac{\tau_w}{\rho}}$) such that regions of the boundary layer can be characterised based on y^+ value. This value should be below one to sufficiently capture the viscous sublayer near the wall [47]. The wall-normal distance of the first cell is set equally (at 0.008 mm) at every stage of the wing, so the difference in y^+ will be caused by changes in wall shear stress, thus velocity gradient, and density, thus velocity. This is evident in the increase of y^+ right after the shock at the outboard wing. The shock will cause a sudden thickening of the boundary layer, which will reduce the velocity gradient at the wall. A region of relatively higher values of y^+ is also observed at the root. This is possibly caused by the lower wing loading and relatively low local lift coefficient (c_l = 0.18). The lower local lift coefficient leads to lower supervelocities and thus a higher local density. This decreases the friction velocity and could explain the higher values of y^+ near the root.

Overall the y^+ value is well below one. The viscous sublayer should be well represented, combined with the growth rate of the first cell of 1.25. This is the maximum ratio advised for Navier-Stokes-based RANS codes by Spalart [58]. The highest y^+ value observed is 0.61 and occurs at the winglet junction,

possibly due to the double shock occurring at this section. With changing flow conditions in different designs the y^+ value should stay below one.

Another important aspect of the quality of a structured mesh is the determinant. It gives an indication of the quality of the cell, whether the edges of the cell are orientated properly or not. Section 3.2 describes how the determinant is calculated. A minimum value of 0.3 is recommended [2]. A determinant close to zero indicates a block close to inversion. Figure 4.3 shows the determinant distribution of the Flying V mesh. Overall, the determinant is close to 1, indicating that most blocks resemble a hyperrectangle. The largest deterioration of the mesh occurs near the tip of the winglet. At this section the mesh has to both, curve back towards the z-x plane, orthogonal to the wing root section, and the blocks start to expand towards the outer boundary. This can also be seen in figure 3.10d. Especially the blocks near the boundary are the most critical here. Their determinant value is still deemed sufficient.

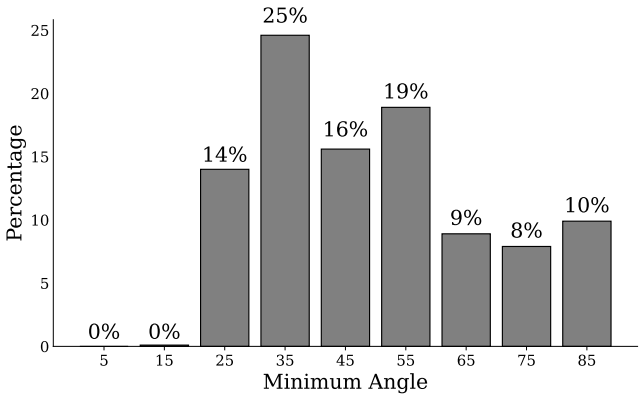

Figure 4.4: Flying V mesh min angle

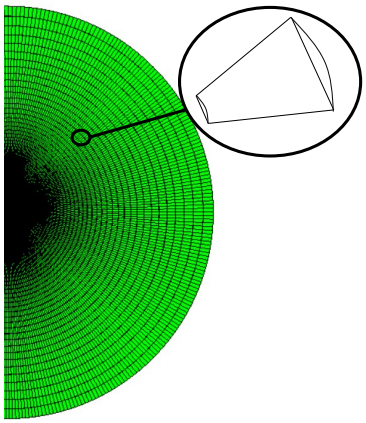

Figure 4.5: Flying V boundary mesh alignment

The final criterion of a structured mesh is the minimum angle. The term 'minimum angle' concerns the smallest angle formed by any of the faces of a hexagonal cell [3]. The minimum angle that ANSYS Fluent can handle is 8 degrees [3], however a value of 30 degrees is desirable from a convergence perspective. Figure 4.4 shows the minimum angle distribution of the Flying V mesh. The relatively high deviation from the ideal 90-degree hexagonal element can be explained by the spherical shape of the domain, the high sweep of the wing and the curvature of the mesh around the winglet. The spherical domain effect is illustrated in figure 4.5. As the mesh has to follow the curvature of the boundary, the angles of the hexagon will never be 90 degrees, as it has to follow the external geometry. This behaviour is amplified near the wing, as the shape of the bounding box becomes elliptical. The choice of boundary shape will always lead to similar behaviour, but the improvements in the far-field pressure boundary condition behaviour due to a spherical shape were deemed to outweigh the relatively worse orientation of the blocks.

The high sweep of the wing causes a mismatch of the orientation of the mesh cells and wing leading edge, as can be seen in figure 3.10c. This leads to a relatively skewed mesh element and is the most important reason for the skewness of the mesh. The blocks are however aligned with the flow and except for cross-flow, don't experience significant gradients in the skewed area. No major performance penalties were observed.

Figure 3.10d shows the curving of the mesh around the winglet. In this region, especially near the trailing and leading edge of the winglet tip, the highest deterioration of the mesh occurs, seen in figure 4.4 as the 14% of the nodes below an angle of 35 degrees. The combination of mesh curvature of both the winglet and the contraction of the mesh makes it hard to avoid this phenomenon. No significant problems were observed during post-processing.

The choice for a structured mesh, in combination with a spherical domain leads to a relatively poorer skewness distribution than an unstructured mesh in a conical domain would. The alignment of the mesh with the flow, the structured nature and the smooth transition from boundary layer to outer mesh do however compensate for this behaviour and, as shown in the Validation section, lead to satisfactory

results.

4.2. Validation

The simulation set-up described in section 3.5 is validated using the industry-standard experimental data of the ONERA M6 wing. The experimental data is obtained by Schmitt, V. and F. Charpin [55] at a Mach number of 0.8395, angle of attack of 3.06 degrees and Reynolds number of 11.72 million. Even though the ONERA M6 wing differs from the Flying V, the same transonic behaviour, e.g. isentropic compression, shocks, boundary layer thickening, can be observed, covering the most important aspects of the simulation. The mesh is constructed according to the methodology described in chapter 3 and consists of 4 million cells.

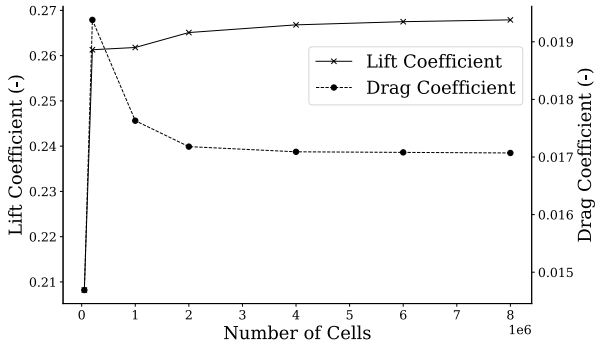

Figure 4.6: ONERA M6 wing mesh convergence study

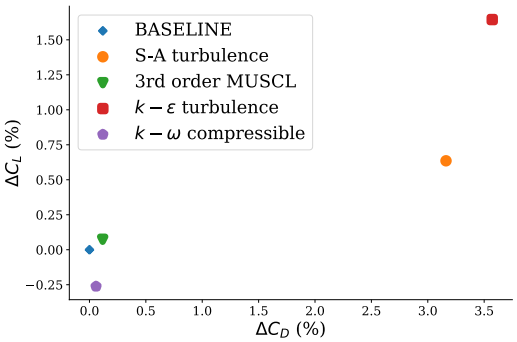

Figure 4.7: ONERA M6 wing sensitivity study

Figure 4.6 shows the grid convergence study of the ONERA M6 validation wing. At around 4 million cells the grid convergence index reaches 0.01%, the same level as the Flying V wing. The 4 million cell mesh is used for the validation. Figure 4.7 shows the sensitivity study performed on the ONERA M6 wing. The largest difference is again seen in the turbulence modelling. The $k-\epsilon$ model shows the largest change, but the high-Reynolds turbulence model might not produce valid results in this flow region. The Spalart-Allmaras turbulence model again shows a 3-4% difference with the Menter SST model. As the S-A model is a valid model for this flow regime, this is again taken as an uncertainty margin. The second-order scheme only shows small changes.

Figure 4.8 shows the comparison of pressure distribution of the validation simulation and experimental data by Schmitt, V. and Charpin, F. [55]. The numerical and experimental data correlate well, also compared to other studies using the ONERA M6 validation data ([61],[16][38][14]). Near the root (figure 4.8a) the pressure peak is captured well, but the numerical code overpredicts the expansion and subsequent shock magnitude. This could be caused by an underprediction of the boundary layer thickness. The same behaviour is however not seen at different spanwise stations. As the wing in the experiment has a wing fence near the root, this might influence the experimental data. Different authors ([16][38][14]) show similar behaviour of overpredicting the shock strength at the root, strengthening this presumption. The lower side of the airfoil does show good correlation.

At the centre section of the wing (figure 4.8c and 4.8d) numerical and experimental data correlate well, except for the steepness of the shock. The effect is slightly more pronounced at the 80% span than at the 65% span location. This might be caused by a certain amount of numerical diffusion, as the mesh will not be as dense as the thin shock. This is expected and accepted as otherwise a non-realistically dense mesh would be required. The third-order MUSCL scheme is designed for these relatively coarser meshes. The delimiter in the scheme will cause some numerical diffusion, which we see here. This is also seen by other authors ([61],[16][38][14]). The stronger shock at the tip (figure 4.8d), caused by the tip effect, is captured well. The pressure peak correlates well with the experimental data.

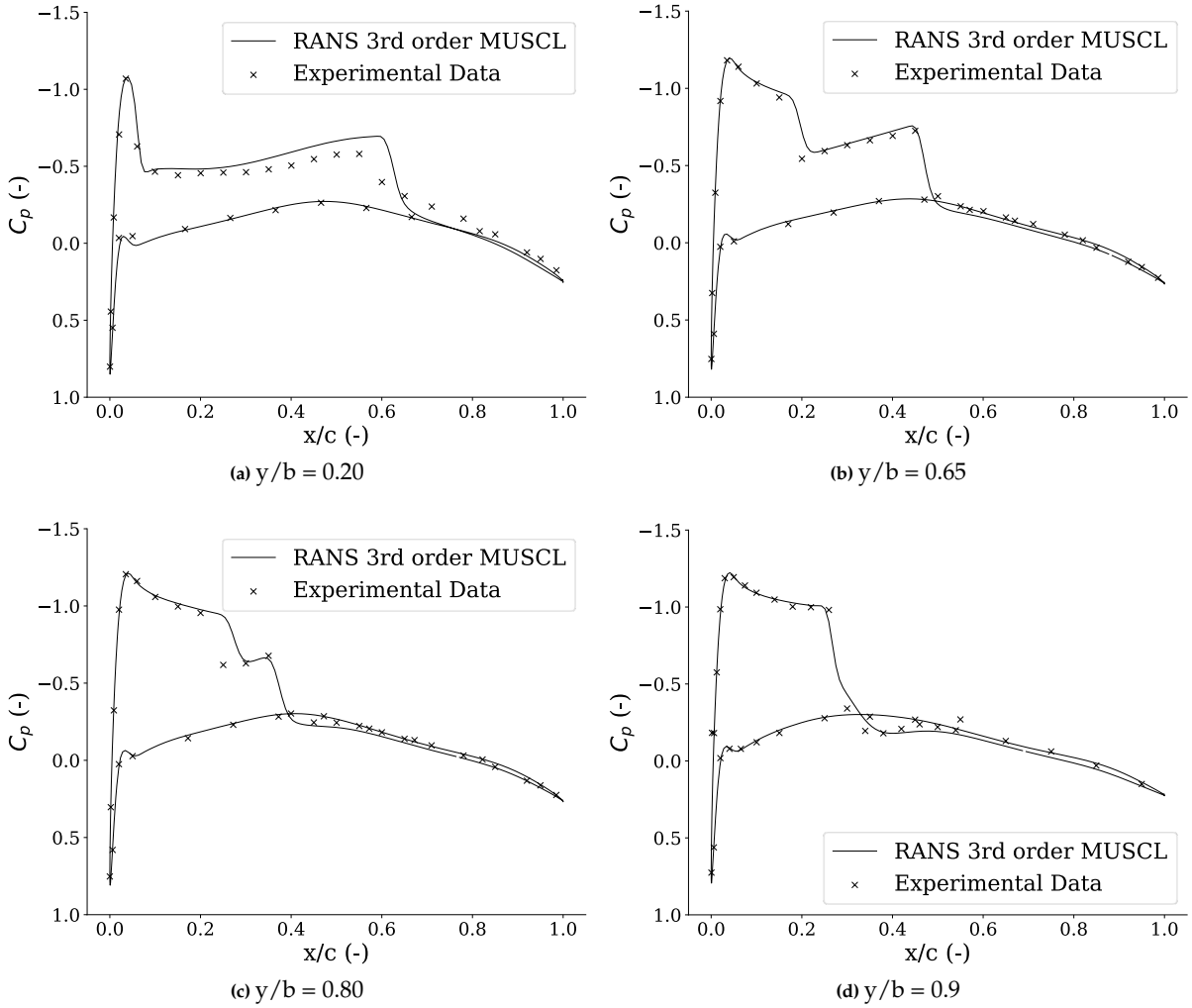

(a) y/b = 0.20 **(b)** y/b = 0.65

(c) y/b = 0.80 **(d)** y/b = 0.9

Figure 4.8: Pressure distribution validation on the ONERA M6 wing (Mach = 0.8395, AOA = 3.06 degrees, Re = 11.72 million)

Table 4.2 compares the aerodynamic coefficients of different numerical studies to the results of this Validation study. The drag coefficient is displayed in drag counts. The different studies show the inherent uncertainty margin in performing RANS simulations. The FLUENT validation study is within the range of all studies performed. The relatively fine, structured mesh used in the Validation study also captures certain shocks, like the shock at y/b=0.8, which were not captured in the lower fidelity Flying V aerodynamic studies [16][61]. The range of outcomes from different authors should be taken into account in the uncertainty margin of this study.

	Turbulence model	Spatial discretization	C_L (-)	C_D (drag counts)
Study	SST	MUSCL + Roe FDS	0.268	171
Araya[4]	SA	Central dif. + JST	0.260	175
Araya [4]	$k-\omega$	Central dif. + JST	0.262	179
Araya [4]	SST	Central dif. + JST	0.253	189
Crovato et al.[14]	Baldwin-Lomax	Green gauss + JST	0.272	174
Le Moigne, Qin [38]	SA	MUSCL+Riemann	0.270	168
Nielsen, Anderson [39]	SA	2nd ord. upwing+ Riemann	0.253	181

Table 4.2: Simulation set-up validation using numerical data of the ONERA M6 wing (Mach = 0.8395, AOA = 3.06 degrees, Re = 11.72 million)

4.3. Two-Dimensional Verification & Validation

Next to the main simulation, the reliability of the two-dimensional simulation is confirmed through verification and validation. Figure 4.9a shows the mesh convergence study performed on a NACA SC(2)-061 airfoil. The mesh is refined by consistently changing the growth ratio of the cells normal to the airfoil, outside of the boundary layer. As the y^+ value is kept constant, this might explain the relatively quick convergence of the drag coefficient, while generally the lift coefficient tends to have a quicker convergence. The perceived order of convergence is estimated, using Richardson extrapolation, to be 2.18, reasonably close to the chosen order of 2 (second order upwind). The GCI of the finest mesh is estimated to be 0.1%, which with the goal of many iterations in mind, is deemed acceptable.

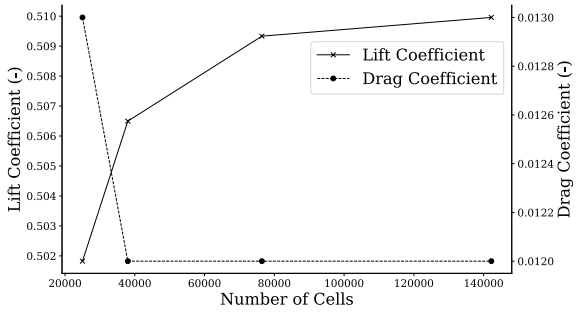

(a) Grid convergence study, NACA SC(2)-061 airfoil (Mach =0.83, Re = 22 million)

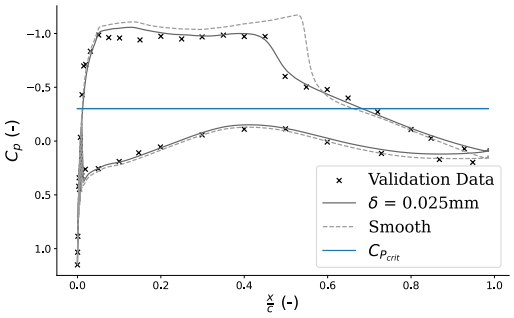

(b) MBB-A3 Validation data (Mach = 0.76, Re = 6.01 million, C_L= 0.626)

Figure 4.9: Two-dimensional airfoil simulation verification and validation

The method is validated using the MBB-A3 supercritical airfoil, using data gathered by the Politecnico di Torino team in the Bedford windtunnel [15]. The test is performed at an angle of attack of 2.21 degrees, Mach number of 0.76 and Reynolds number of 6.01 million. Windtunnel data of higher Mach numbers is available, but MBB-A3 supercritical airfoil and other open-source well validated airfoils [15], as well as the NACA supercritical airfoil series [22], reach there drag divergence Mach number between M =0.78-0.8, making validation non-trivial.

Figure 4.9 shows the validation results. Initially the zero-roughness wall boundary condition led to an overprediction of the expansion area and shock-strength. This indicates an underprediction of the boundary layer thickness, increasing the airfoil camber. Michael and Sharif [37] showed similar results in the validation of the RAE-2822 airfoil. They showed that adding a certain roughness to the wall can cause earlier transition and thickens the boundary, such that the shortfall in turbulence modelling based on the Boussinesq approximation can be compensated. Figure 4.10 shows the effects of adding 0.025 mm of roughness on transition, indicated by the black lines. The position where transition starts to occur, marked by a turbulent viscosity higher than 0.02, changes from $x/c = +/-0.6$ to $x/c = +/-0.2$. The thicker, turbulent boundary that ensues, leads to a significant improvement in the agreement of numerical and experimental data. The experimental lift coefficient of 0.626[15] agrees well with the numerical lift coefficient of 0.620. The roughness did increase the drag coefficient such that the drag coefficient of 195 drag counts is significantly higher than the experimental 87 drag counts[15]. It is assumed the increase in drag coefficient is caused by the roughness and influences the skin friction coefficient. As the pressure distribution does correlate well with the experimental data, the optimization results are assumed realistic. The drag coefficient might be higher than the values expected on the three-dimensional wing.

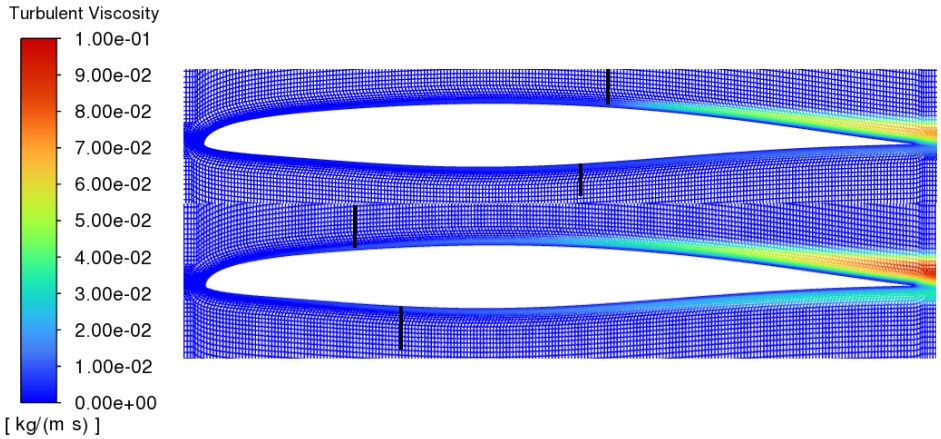

Figure 4.10: Turbulent viscosity of a smooth (upper) and 0.025mm rough (lower) wall

The findings of the validation are implemented in the optimization. As the Reynolds number differs by a factor of 3.5 compared to the Flying V simulation, the roughness is scaled with the Reynolds number, such that the roughness penetrates approximately to the same relative y^+ value in the boundary layer. An estimation of the effect of Reynolds number on the skin friction coefficient shows a correlation of $C_f \sim Re^{-1/5}$ (equation 3.52). The friction velocity correlates to the skin friction coefficient as: $u_\tau \sim C_f^{1/2}$ (equation 3.21) and y plus correlates linearly with the friction velocity (equation 4.4). With these correlations equation 4.5 is set up and the roughness height is subsequently scaled. This leads to a roughness height of 0.00219 mm for the Flying V airfoil.

$$\delta_{Re_2} = \delta_{Re_1} \frac{Re_2}{Re_1}^{-1/10} \tag{4.5}$$

5

Results and Discussion

With the set-up of the simulation validated, the Flying V in its current parametrization can be optimized. The optimization procedure is described in chapter 3. As this study focuses on cruise performance, the Flying V is optimized at cruise conditions. The top-level requirements of a Mach number of 0.85 and cruise altitude of 13 km lead to a design Reynolds number of 88.3 million. Based on the drag polar and top-level requirements, the geometry is optimized for a cruise lift coefficient of 0.26. The angle of attack is obtained through an iterative process.

Flight Conditions		Reference Values	
Cruise altitude	13 km	$\bar{c}$	19 m
Mach number	0.85	S_{ref}	880 m^2
Reynolds number	88.3e6	T	216.6 K
C_L	0.26	μ	1.432e-5 Pa·s

Table 5.1: Flight conditions and reference values for the Fluent simulations

The research is divided into three different phases. As the planform is based on numeral previous Flying V studies, the first phase focuses on the optimization of Flying V sections, leaving the planform unaltered. The objective is to find a balance between an elliptical lift distribution, wave drag, section performance and longitudinal static stability, which maximizes the L/D. With the insights from phase 1, phase 2 aims to make relatively small planform changes to redistribute wing area. Local lift coefficients on sections that suffer high compressibility losses can be reduced to relieve these sections. Other sections could have some increased loading. These area distributions should provide a more efficient lift distribution. Phase 3 focuses on the airfoils of the outboard wing. As open-source airfoils in the right flow regime are scarce, a two-dimensional optimization aims to create a new set of airfoils, suitable for the flow regime. The three-dimensional nature of the flow at the outboard wing will change the characteristics of the airfoil. Therefore multiple iterations are performed to obtain the optimal twist distribution of the new airfoils. The lift and drag polars and the drag divergence plot of the final design are presented.

5.1. Phase 1: Section Optimization

Four iterations steps are summarized in this section:

Iteration	Description
1.1 Baseline	The baseline design is based on previous Flying V work, with the new parametrization.
1.2 Improved Airfoils	The original NACA supercritical airfoils of the outboard wing had suboptimal performance. Based on the work of Faggiano[16] the airfoils of the outboard wing are changed. Also, the transition section profile is improved upon.
1.3 Section Optimized	Based on the results of iteration *1.2.Improved airfoils*, the lift at the root is lowered, the camber and aft-loading of the middle wing increased, profiles smoothened and incidence angles of the outboard wing are increased.
1.4 Elliptical Lift	This iteration tries to create an elliptical lift distribution based on the incidence angle and camber of different sections.

Table 5.2: Flying V iterations summarized

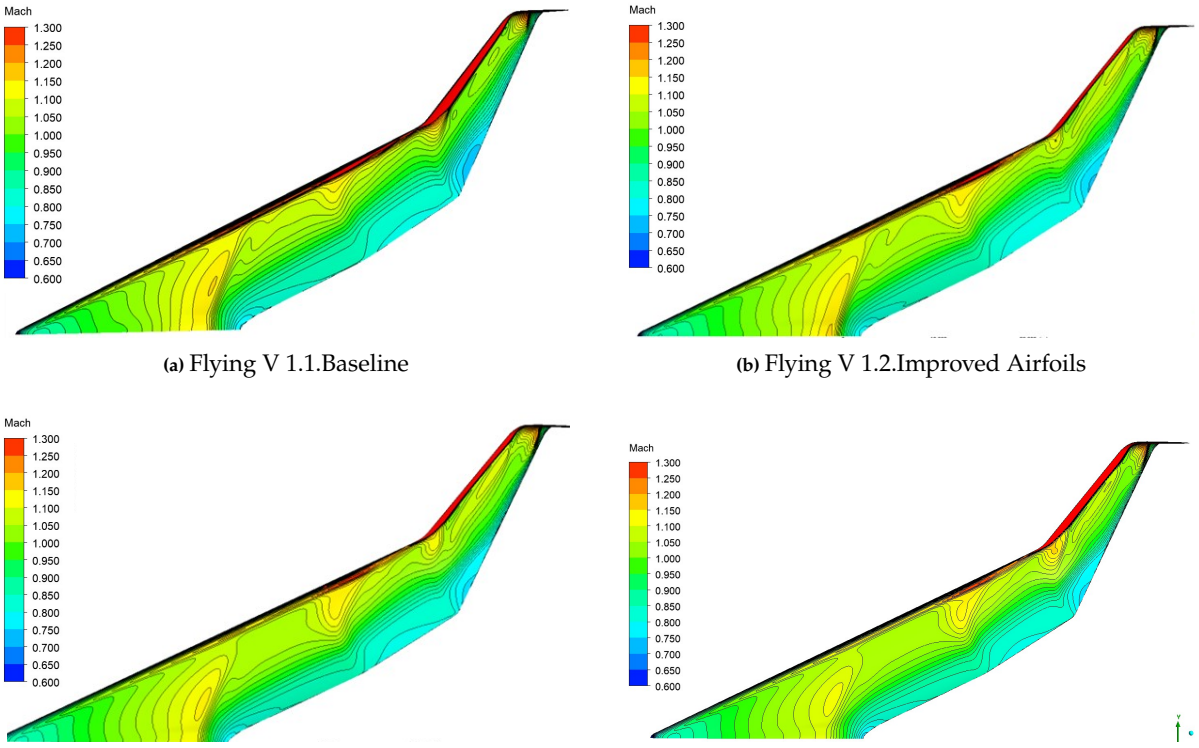

(a) Flying V 1.1.Baseline

(b) Flying V 1.2.Improved Airfoils

(c) Flying V 1.3.Section Optimized

(d) Flying V 1.4.Elliptical Lift

Figure 5.1: Mach contours of different Flying V iterations (Mach =0.85, Re = 88.3 million, C_L = 0.26)

Figure 5.1 shows the Mach number isosurfaces on the wing. The relatively large supersonic area on the outboard wing of the baseline design leads to a relatively high wave drag, decreasing cruise performance. A clear root effect is visible, as the Mach isobars curve towards the root. This leads to shock formation near the trailing edge. Another important point is the large thickening of the boundary layer at the sections with the highest thickness-to-chord ratio (0.4<y/b<0.6). This effectively decambers the upper part of the section, decreasing lift near the trailing edge. The pressure distribution plots show this effect as upper and lower C_p curves tend to merge (Figure 5.4b). Interference effects are recognizable at the wing-winglet junction.

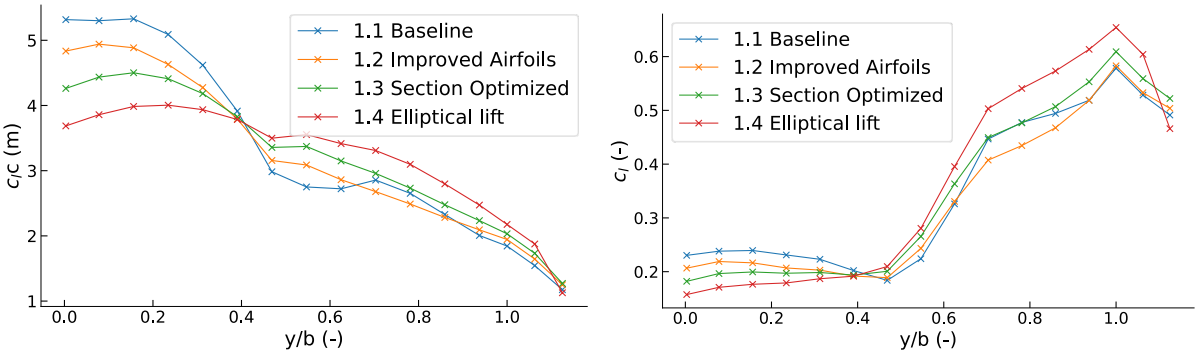

(a) Spanwise lift distributions

(b) Section lift distributions

Figure 5.2: Spanwise lift and section lift distributions of the different iterations (Mach =0.85, Re = 88.3 million, C_L = 0.26)

Figure 5.2 shows the spanwise lift and lift distributions of the iterations. The winglet is included in the lift distribution so y/b exceeds 1. The baseline design shows a decrease in spanwise lift at the transition section of cabin and outboard wing. This can partially be explained by the boundary layer thickening due to the high t/c ratio in this section, which is not taken into account by inviscid codes and partially by a lack of camber and aft-loading in this section (Figure 5.4c). Design of this section is limited by cabin/cargo space structural and volume constraints. An example of the boundary layer thickening is shown in figure 5.3b, visualizing the decambering of the section due to the thick boundary layer.

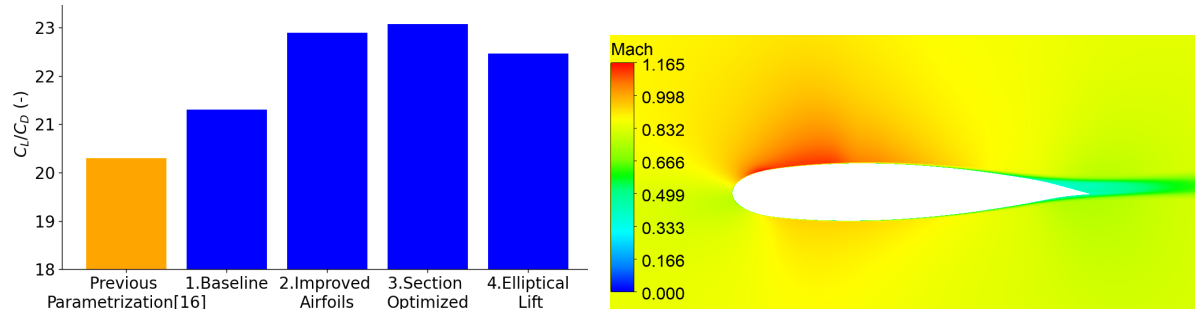

(a) Lift-to-drag ratios of the different iterations

(b) Example of boundary layer thickening at y/b = 0.4

Figure 5.3: Boundary layer thickening and lift-to-drag ratios (Mach =0.85, Re = 88.3 million, C_L = 0.26)

5.1.1. 1.1.Baseline to 1.2.Improved Airfoils Design

As relatively significant shock losses on the outboard wing and a reduction of lift in the mid-section are present in the baseline design, multiple steps are taken to mitigate these issues. The baseline outboard wing sections consist of NACA supercritical airfoils, defined by a set of CST coefficients. To reduce the supersonic region, more suitable airfoils for the required lift coefficient can improve performance. These airfoils were found in the original Flying V aerodynamic optimization performed by Faggiano [16]. These sections were optimized starting from the NACA supercritical sections, using an Euler code. These airfoils are designed for a lift coefficient ranging from 0.45 to 0.5, which is approximately the range in which the baseline design operates. The results of this implementation can clearly be seen in Figure 5.1b. The supersonic region on the outboard wing has decreased significantly, while the lift coefficient outboard slightly increased. The airfoils have their maximum thickness-to-chord ratio further aft and show a sharper nose radius. This leads to an airfoil with a more 'peaky' supersonic bubble, but also a reduced shock strength and some further expansion after the shock.

Certain changes to the wing were made to increase lift in the mid and transition sections. First of all the camber was increased by lowering the trailing edge, increasing H_3, the upper surface height and lowering H_1, the lower surface height. Increasing the camber was possible due to the absence of strong shocks in this region, especially near the trailing edge. Secondly, the aft loading of the wing is increased by changing the trailing edge open and incidence angles. This has the additional advantage that the

angled trailing edge aids in the pressure recovery of the upper surface. Finally, these sections were optimized for smoothness.

A significant increase in lift-to-drag ratio is observed with the mentioned changes. Wave drag losses are decreased, while the Oswald factor is increased due to a more elliptical lift distribution. It can be observed that lift at the root is still relatively high, which is a focus point of following iterations.

5.1.2. 1.2.Improved Airfoils to 1.3.Section Optimized Design

The focus point of iteration *1.3.Section optimized* is a more elliptical lift distribution, while maintaining section performance. The root trailing edge height was increased to reduce the camber and incidence angle of the root. To maintain the same lift coefficient, C_L, for the same angle of attack, lift over the mid-and outboard wing has to be increased. The incidence angle of the inboard section of the outboard wing and the aft loading at the oval retention parameter are increased (figure 5.4c). Furthermore, the camber of the mid-wing is increased (Figure 5.4b).

The changes led to a further 1.5% improvement in L/D. Figure 5.2a shows the reduction of lift at the root and an almost linear increase in lift at the mid-and outboard wing. This should improve the Oswald efficiency factor, which is important for a low aspect ratio wing like the Flying V. Important to notice is the fact that the section lift coefficient outboard of the outboard wing starts exceeding a value of 0.5, which exceeds the design conditions of the airfoil. This can also be perceived in the pressure distribution of the section (figure 5.4d). A lower pressure coefficient, thus a higher Mach number near the leading edge is observed. The stronger shock compared to iteration *1.2.Improved airfoils* leads to higher wave drag, decreasing performance.

The root, as seen in Figure 5.4a, still shows a clear root effect as the pressure peak is shifted significantly aft. The coupled nature of the parametrization makes it difficult to implement classical root changes, such as a reduction in camber, coupled with an increase in incidence angle, as the shape is constrained by volume and shape requirements.

The transition between cabin and outboard wing is visible between Figure 5.4b and Figure 5.4c. The shape at y/b=0.4 is relatively complicated to control as it cuts through different profile sections. The section shape, together with the boundary layer thickening, as visualised in Figure 5.3b, leads to only small improvements in the pressure distributions between the iterations. The pressure at lower and upper side is almost identical near the trailing edge. Significant improvements are however made more outboard of the transition zone. At y/b = 0.6 the profile starts to show transonic profile characteristics with aft loading and a relatively thin, angled trailing edge. Iteration *1.3.Section Optimized* shows improved aft loading and upper section loading without wave drag penalties. The section lift coefficient increased by 0.9.

Another important improvement is the cruise angle of attack. The baseline model has an angle of attack of 5.2 degrees for the required C_L of 0.26. By increasing the mid/outboard wing section lift relatively more than the implemented decrease of lift at the root, the cruise angle of attack was reduced to 3.5 degrees in iteration *1.3.Section optimized*. This reduces the required rotation angle at take-off, thus lowering landing gear size and weight.

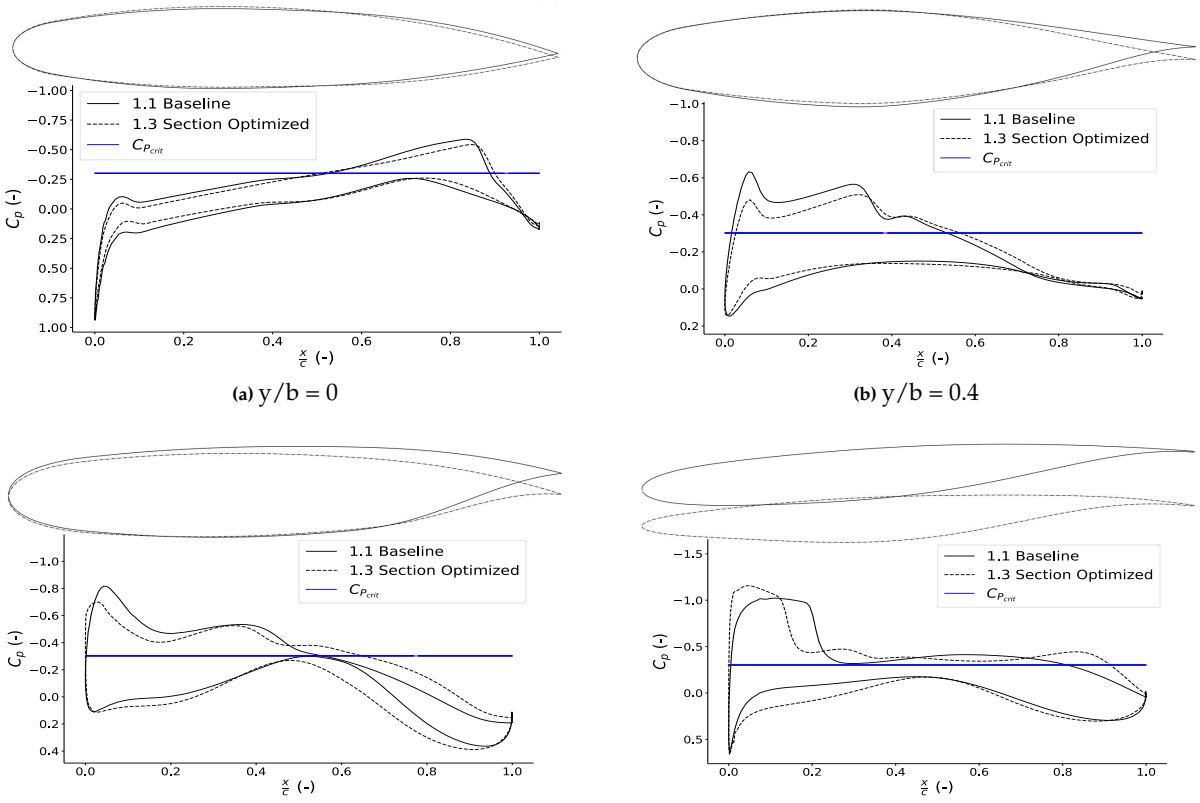

(a) y/b = 0 **(b)** y/b = 0.4

(c) y/b = 0.6 **(d)** y/b = 0.94

Figure 5.4: *1.Baseline* and *3.Section Optimized* sections and pressure distributions (Mach =0.85, Re = 88.3 million, $C_L = 0.26$)

5.1.3. 1.3.Section Optimized Design to 1.4.Elliptical Lift

Iteration *1.4.Elliptical Lift* aims to create an elliptical lift distribution. A further increase in outboard wing incidence angles and increase in camber on the mid-wing is required for an elliptical lift distribution. Without planform changes the section lift coefficient starts to exceed the limitations of the outboard wing airfoils, explaining the reduction in L/D associated with this iteration. The section lift coefficient exceeds 0.6 at the outboard section, 20% higher than the design lift coefficient at a Mach number of 0.85. This leads to a relatively strong shock and degraded performance. At the root, a reduction of lift is perceived. As the TE profile is interpolated between y/b=0 and y/b = 0.35, it is not straightforward to tweak individual parts of the lift distribution.

5.2. Phase 2: Planform Optimization

Phase one aimed to optimize the different sections of the Flying V outer mold line, resulting in an improvement of L/D. The planform dimensions are the result of the continuous effort over the past years, summarized by Vos en Benad in [8]. Significant planform changes are not the goal of this study, but the high-fidelity method can give insight into some minor changes.

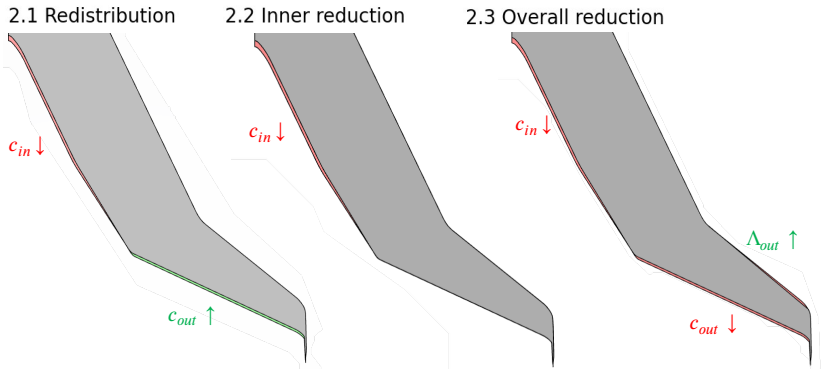

Figure 5.5: Planform change strategies to optimize the L/D

The three strategies to planform change are illustrated in figure 5.5. The main goals are to reduce the wetted area of the aircraft and to change the distribution of area to facilitate a more efficient section lift distribution.

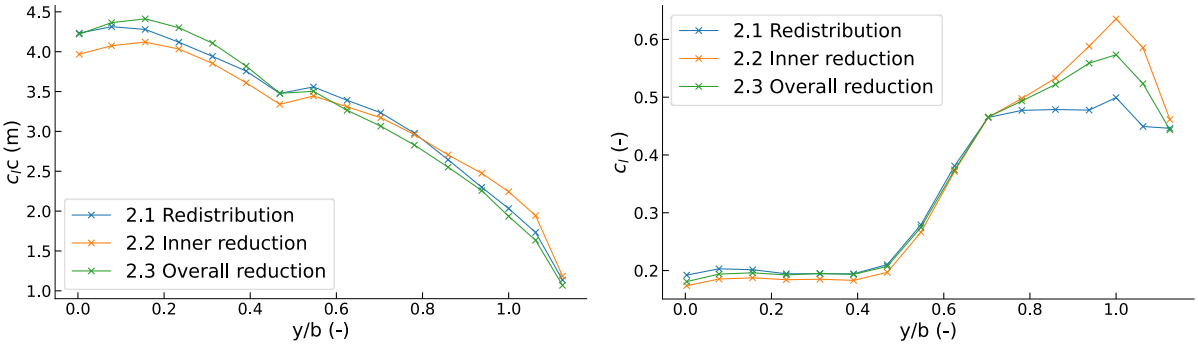

(a) Spanwise lift distributions

(b) Section lift distributions

Figure 5.6: Spanwise lift and section lift distributions of the different iterations (Mach =0.85, Re = 88.3 million, $C_L = 0.26$)

	Baseline	2.1	2.2	2.3
Half Wing Area (m^2)	453.0	451.3	446.6	451.2

Table 5.3: Changes in wing area of the designs

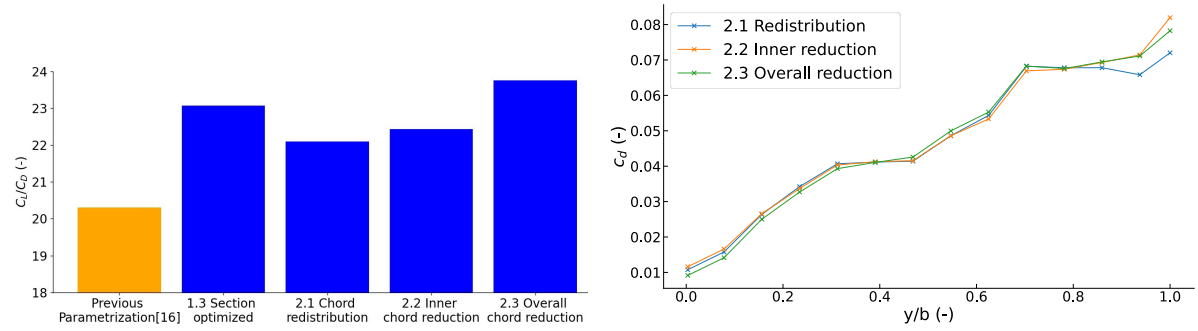

(a) Lift-to-drag ratio of the second phase

(b) Section drag coefficient

Figure 5.7: Boundary layer thickening and lift-to-drag ratios (Mach =0.85, Re = 88.3 million, $C_L = 0.26$)

5.2.1. Design 2.1.Chord Redistribution

As relatively strong shocks are observed at the outboard wing, shown in figure 5.4d and a lack of (stronger) shocks is present on the inboard wing, a slight decrease in chord near the inboard wing and

increase in chord near the outboard wing could increase efficiency. This is visualised in the leftmost wing of figure 5.5. The largest thickness-to-chord ratio occurs at the transition section. Because of the boundary layer thickening issues described in section 5.1, the chord length is not decreased near the transition section, which can be seen as a slight tapering of the chord length decrease in figure 5.5.

The most optimal design, shown in figure 5.6, has a reduction of root chord length of 20 cm and an increase of outer chord length of 15cm. The results show a clear reduction of lift near the root with an increase of lift in especially the middle section. The increase in outboard wing chord length allowed for a significant reduction in outboard wing local lift coefficient. A plateau of wing coefficient was chosen at the outboard wing, partly because the optimal design of Faggiano [16] showed a c_l plateau, and partly to relieve loads at the tip/winglet, where a double shock is present. Analysis indicates that this leads to a relatively high amount of wave drag in this specific area. The spanwise lift distribution hints at a more elliptical lift distribution, pointing at a promising design.

The lift-to-drag ratio of the design was however reduced to 22.1. The section drag coefficient (figure 5.7b) does indicate a lower drag coefficient around the winglet. The change in drag coefficient is however significantly less than the decrease in lift coefficient. The airfoils are either at a more off-design condition here or other non-linear effects are coming into play. The drag coefficient has also slightly increased over the inboard wing, due to the relatively smaller chord length.

5.2.2. Design 2.2.Inboard Chord Reduction

As design *2.1.Chord redistribution* only slightly decreases the wetted area, the second approach is to decrease the chord of the inboard wing only. The unaltered chord length of the outboard wing necessitates a slightly elevated section lift coefficient, as the reduction in wing area requires an increase in angle of attack. Again the length at the transition section is unaltered, as the thickness-to-chord ratio is at a maximum in this area. The chord is reduced by 25 centimeters at the root, tapering off to 0 at the trailing edge kink, as seen in figure 5.5. To compensate for the reduction in chord length, the trailing edge is lowered to increase camber.

The reduction in root chord requires a slightly higher angle of attack of 3.8 degrees. The increase of angle of attack increased the lift at the tip as seen in figure 5.6. The higher angle of attack also leads to large supervelocities at the winglet. Overall this reduced the lift-to-drag ratio to 21.9.

5.2.3. Design 2.3.Overall Chord Reduction

An overall reduction of wetted area, as visualised in the rightmost wing of figure 5.5, is attempted to increase overall efficiency. An overall reduction in wing area will lead to a slightly higher section lift coefficient across the wing. The outboard wing, leading edge sweep angle is slightly increased to keep a constant trailing edge sweep angle, important for the control surfaces. An increase in leading edge sweep angle might also decrease the large suction peak perceived.

As larger changes in chord length did not seem to increase the L/D, this iteration only changes the chord length in the order of magnitude of centimeters. The most efficient design was an overall reduction of 2.5 cm in chord length, except for the trailing edge kink, shaving off approximately 2 m^2 of wetted area. The L/D of this iteration increased to 23.7, which is a significant improvement. The incidence angles of the winglet were also reduced in this iteration, which will have played a part in the increase of L/D. The lift in the middle of the wing is slightly increased, with a decrease in lift at the root. This should give a little more elliptical lift distribution, without greater wave drag, which did occur in previous iterations. The improvement of the wing-winglet junctions is explored later in the thesis.

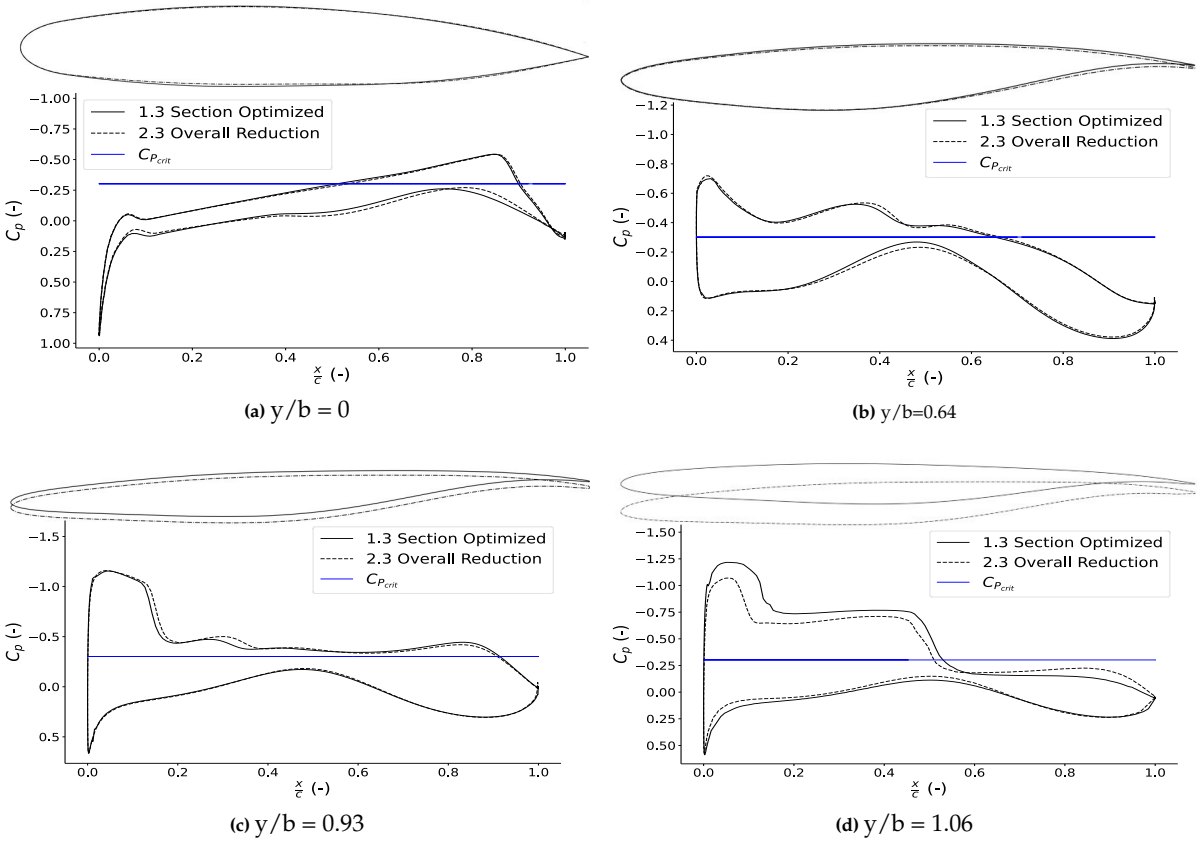

(a) y/b = 0 **(b)** y/b=0.64

(c) y/b = 0.93 **(d)** y/b = 1.06

Figure 5.8: *1.3.Section Optimized* and *2.3.Overall reduction* sections and pressure distributions (Mach =0.85, Re = 88.3 million, C_L = 0.26)

Figure 5.16 shows a comparison of pressure distributions of iteration 1.3 and 2.3. The slight decrease in chord length slightly increases the effective camber. Figure 5.8b shows this phenomenon and the lift in the middle section of the airfoil is increased. At the root (figure 5.8a) the main difference is a slight redistribution of lift distribution towards the middle of the airfoil. Near the tip (figure 5.8c) isentropic recompression weakens the shock compared to design 1.3. The unloading of the winglet root has a clear effect on the pressure distribution. As wing-winglet junction interference plays a large role here, the highest Mach numbers are observed in this area. The reduction of winglet incidence angle significantly reduces the perceived Mach number. It is still high, at M = 1.41, so buffeting is a possibility. The second shock could not be mitigated, as the interference remains strong. Overall the decrease in wave drag likely had a significant role in the increase in L/D.

5.3. Wing-Winglet Junction

As shown in section 5.2.3, the wing-winglet junction has a significant influence on the overall efficiency of the design. This section aims to investigate the effects of different sections and incidence angles at the winglet on the efficiency of the Flying V.

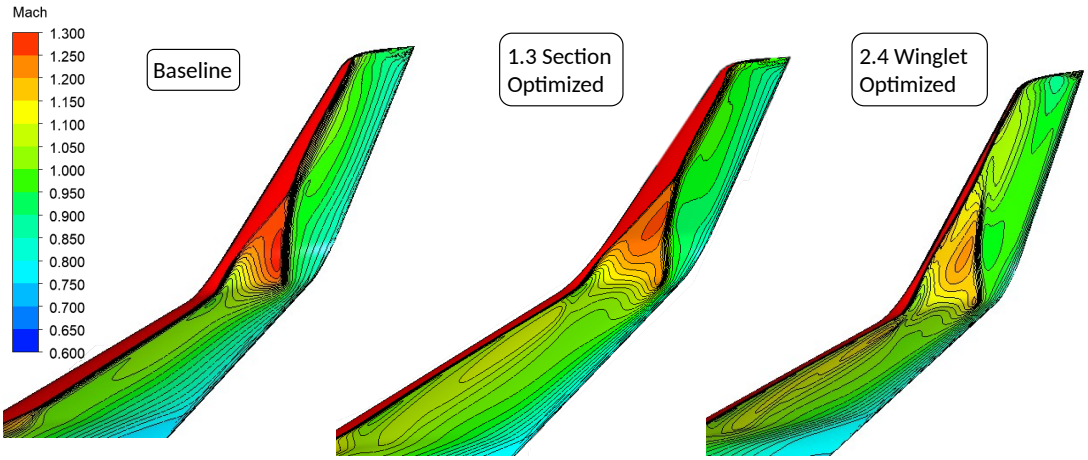

Figure 5.9: Mach number contour of the wing-winglet interaction

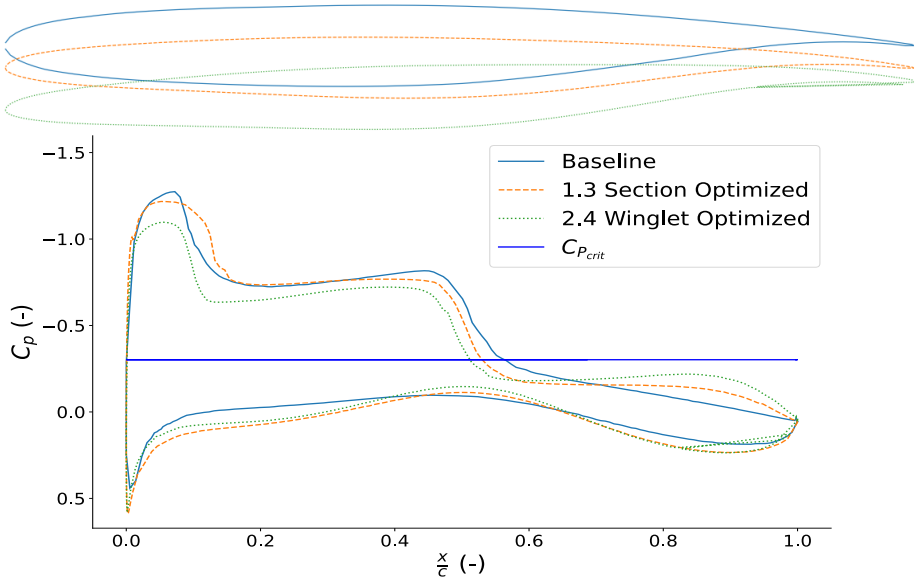

Figure 5.10: Airfoils and pressure distribution at the wing-winglet junction

Figure 5.10 shows the pressure distribution at the wing-winglet junction. While the Faggiano airfoil (*1.3 Section Optimized*) shows more isentropic recompression and a weakening of the first shock, compared to the baseline, an optimization of the incidence and dihedral angle, combined with a 0.01c thick trailing edge improves performance. The strength of the second shock is weakened less by the changes, but no longer interacts with the first shock towards the winglet tip, as seen in figure 5.9. Even though the RANS simulation only shows a relatively small separation bubble, the Mach numbers above 1.5 for the first and above 1.3 for the second shock of the baseline design are likely to cause buffeting. The Mach number of the first shock is still between 1.3 and 1.4 depending on the position of the optimized design, so buffeting should be investigated further. The second shock shows reduced Mach numbers ranging from 1.1 to 1.2. Still, this is an area of concern as the boundary layer might be exhausted by the first shock. The optimized winglet (iteration 2.4) increased the L/D from 23.7 to 23.9.

5.4. Phase 3: Airfoil Gradient-Based Optimization

The previous iterations proved the importance of the design of the outboard wing. Only a limited range of airfoils operating efficiently at M=0.85 are, however, available in literature. The Faggiano airfoils used in phases 1 and 2 are optimized using an Euler code, for a different Flying V geometry [16]. An

optimized airfoil for these flight conditions could improve performance. This section presents the results of the two-dimensional airfoil optimization.

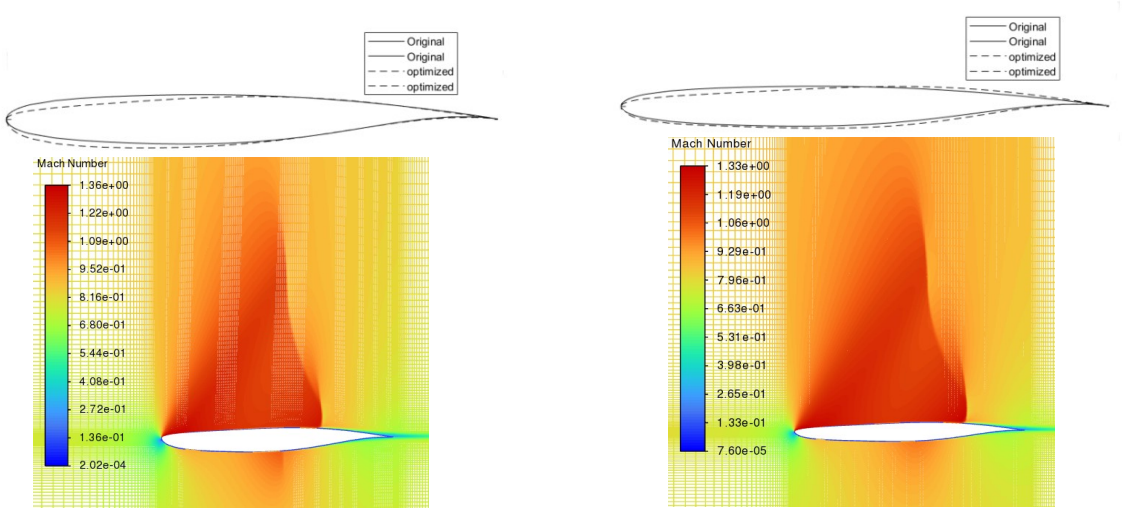

(a) Root airfoil (Mach =0.83, Re = 34.7 million, c_l = 0.48) **(b)** Tip airfoil (Mach =0.83, Re = 13.5 million, c_l = 0.52)

Figure 5.11: Airfoil visualisation and Mach contour of the optimized airfoils

Figure 5.11 shows the results of the two-dimensional optimization. The simulation is run at a slightly lower Mach number than the cruise speed, at M = 0.83. The 10% thick NACA SC(2)-0410 airfoil, seeding airfoil for the root, reaches its drag divergence Mach number here for a c_l of 0.48. With a higher Mach number, no valid results could be obtained. An initial L/D of 17.8 was reached. This is relatively low compared to the L/D ratios of excess of 50 that can be reached in two dimensions [15], but the NACA airfoil is approximately at/above its Mach drag divergence Mach number so efficiency is decreasing. The tip airfoil with its lower thickness to chord ratio of 8 % performs slightly better at an L/D of 20.2.

The L/D of the root airfoil was increased from 17.8 to 32.9. The large increase can mainly be explained due to the lack of trailing edge separation in the new design, which was occurring in the baseline. As seen in figure 5.12a, the nose radius constraint is satisfied, but not in the way that was envisioned. The constraint that enforces a certain thickness near the nose allowed the nose radius on the upper surface to become sharp. This might work well for this flight condition, but likely leads to issues at off-design conditions. A relatively flat upper surface up to the shock allows for some isentropic recompression. After the shock the aft-camber is increased, generating extra lift. Aft-loading is kept relatively constant. Curious is the shock that exists on the lower side. This is not seen in any of the three-dimensional simulations performed, but will influence the efficiency in two dimensions.

The tip airfoil shows similar design characteristics as the root airfoil. The L/D was increased from 20.2 to 36.6. The nose radius is less sharp at the upper side than the root airfoil, creating a more versatile design. The reduced t/c helps to mitigate the shock that is present at the root. The maximum perceived Mach number is also lower than the thicker airfoil. The off-design performance of both airfoils is questionable

Figure 5.12a shows the pressure distributions of both designs. Until x/c = 0.5 the flow is isentropically recompressed. After this point, the flow is expanded again as the airfoil's aft-camber starts to increase. A clear difference between the airfoils can be seen at the lower side, where the larger t/c is mainly shown in the reduced pressure on the lower side of the root airfoil. It reaches the critical Mach number at x/c = 0.5 and even a small shock is present. This can also partly explain the higher efficiency of the tip airfoil.

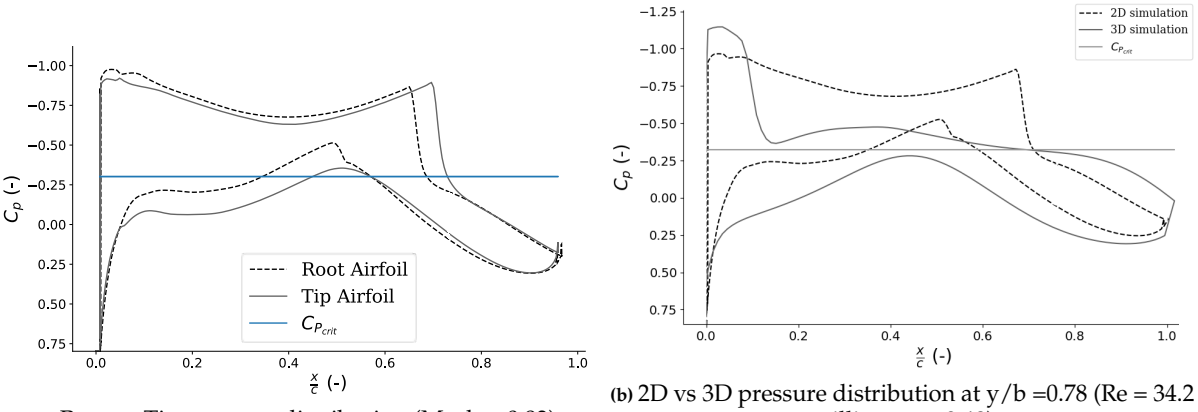

(a) Root vs Tip pressure distribution (Mach = 0.83)

(b) 2D vs 3D pressure distribution at y/b =0.78 (Re = 34.2 million, c_l = 0.48)

Figure 5.12: Pressure distributions of the new airfoils

The second part of this section concerns the implementation of the new airfoils on the Flying V. As three-dimensional effects, like sweep and the tip vortex, influence the local angle of attack. The sections are matched in c_l, not incidence angle. Figure 5.12b shows the pressure distribution near the root of the outboard wing (y/b =0.78). A large discrepancy is seen between the pressure distributions. The suction peak in the three-dimensional simulation is significantly higher, leading to a strong shock towards the leading edge instead of the inflection point of the airfoil. Also, the lower side shows remarkably different behaviour in three dimensions, as the pressure is higher and decreases more gradually. The same behaviour can be seen when comparing the pressure distributions of the Faggiano and NACA airfoils in two and three dimensions. The large expansion and subsequently strong shock can be seen in figure 5.13a as the dark red area followed by the shock. Of the five iterations performed, with five different optimized airfoils, the maximum L/D reached was 22.9, compared to 23.9 reached in the previous optimization. The conclusion that can be drawn is that three-dimensional effects dominate the flow physics of the outboard wing. The performed two-dimensional optimization does not make sense if the pressure distributions do not correlate with the three-dimensional conditions. These findings were confirmed by comparing the two-dimensional and three-dimensional performance of the Faggiano and NACA airfoils. The reduced Mach number of the 2D optimization will also have an effect.

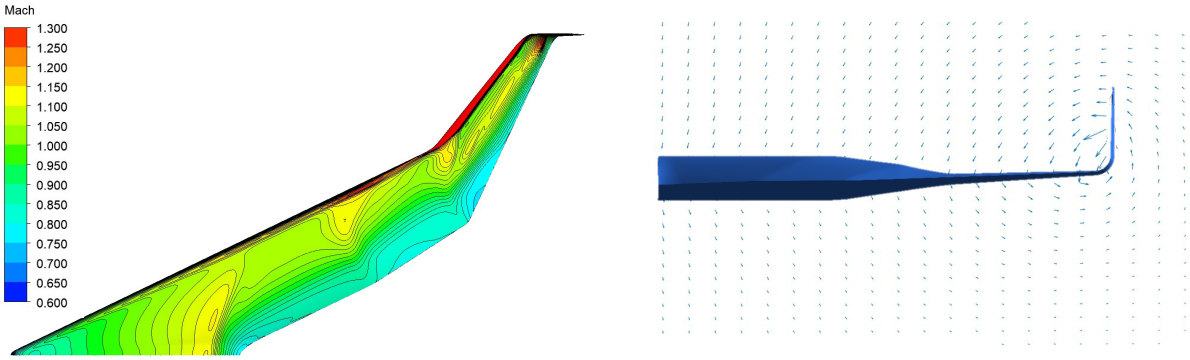

(a) Mach number contour with the new airfoils (Mach =0.85, Re = 88.3 million, C_L = 0.26)

(b) Velocity vector field behind the winglet, with a maximum velocity of 55.5 m/s

Figure 5.13: Mach number contour and velocity vector field with the Obert airfoils

There are different ways in which the outboard wing is influenced by three-dimensional effects. At the outboard wing root a strong vertical tapering occurs, as the t/c decreases from inboard to outboard wing. This can be seen in figure 5.13a as a distortion of Mach isobars near the leading edge kink. The subsequent spanwise changes in pressure create a spanwise pressure gradient creating three-dimensional effects. This makes the two-dimensional assumption less valid.

The low aspect ratio of the wing of 3.59 and measured from the leading edge kink of the outboard wing

2.27 means the tip vortex has a large influence on the entire wing. This is visualised in figure 5.13b. The entire outboard wing sees a change in flow angle, also in the spanwise direction. This influences the two-dimensional characteristics of the flow. Towards the tip a distortion of the Mach isobars is visible. A combination of the tip effect and wing-winglet junction leads to more three-dimensional influence on the flow region.

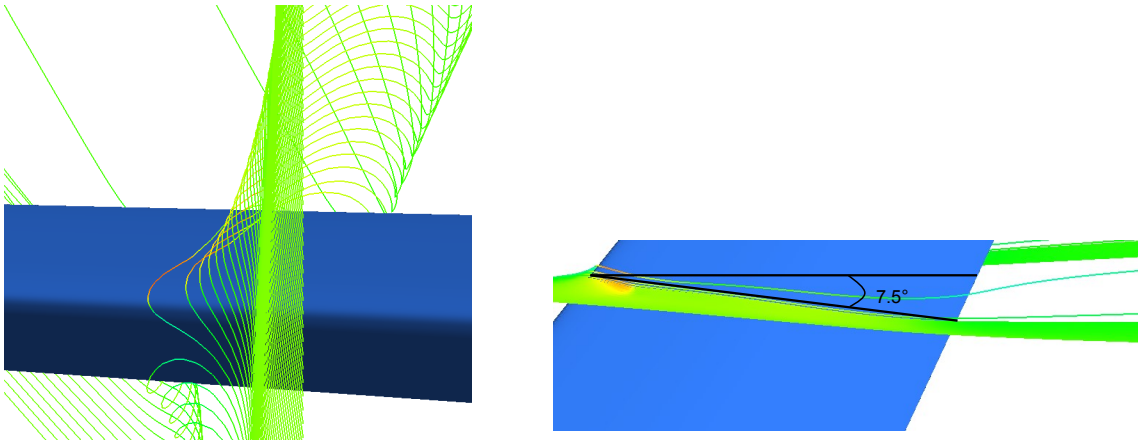

(a) Front view of cross-flow (y/b = 0.8)

(b) Top view of cross-flow (y/b = 0.8)

Figure 5.14: Cross-flow on the outboard wing (Mach =0.85, Re = 88.3 million, C_L = 0.26)

Cross-flow also influences the two-dimensional characteristics of the wing. Figure 5.14 shows streamlines in cruise conditions. The effects of cross-flow on a standard wing are mainly important at high-lift conditions, where boundary layer cross-flow can lead to separation [43]. Figure 5.14b shows a 7.5 degree angle between the free stream and the flow on the wing. The 7.5 degrees alone do not explain the discrepancy between two-dimensional and three-dimensional simulation conditions, but will contribute. Near the leading edge, significant spanwise streamline curvature could contribute to the large suction peak shown in figure 5.12b. The consequent larger shock changes the pressure distribution over the whole wing.

The three effects described try to explain the discrepancy in pressure distributions.

5.4.1. A Different Set of Airfoils

As the results of the two-dimensional optimization are suboptimal and large pressure peaks on the outboard wing are still present, a different set of airfoils is tried. The airfoils are taken from Obert [43] and recreated using Bezier curves. The sections are based on the design of modern transonic airliners. The main goal of this part of the optimization is to reduce the Mach numbers on the outboard wing.

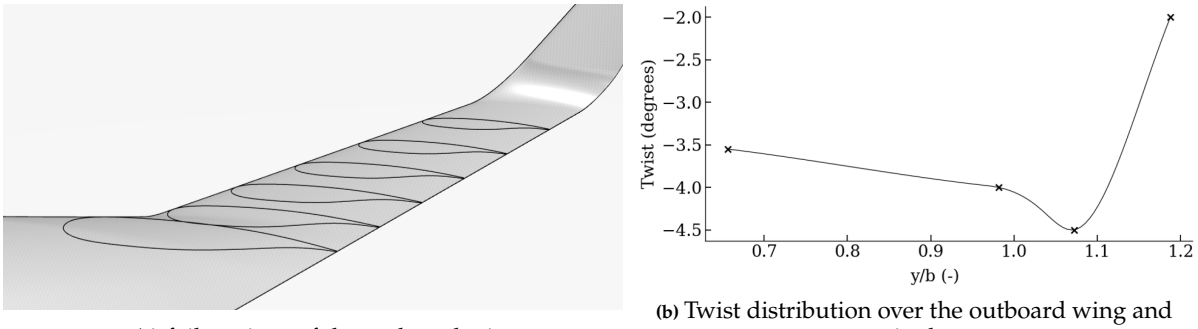

(a) Airfoil sections of the outboard wing

(b) Twist distribution over the outboard wing and winglet

Figure 5.15: Outboard wing characteristics including the Obert airfoils

Figure 5.15a shows the airfoils implemented on the outboard wing, on the most efficient iteration.

This is also the final version of this thesis/the most efficient design. The airfoils show supercritical characteristics. The curvature on the upper side is relatively small and the nose radius is relatively large. The trailing edge features a blunt cusp. Aft-loading is present to compensate for the reduced upper surface curvature. The thickness-to-chord ratio starts at 10% and ends at 8% at the wing tip. Figure 5.15b shows the twist distribution of the outboard wing. The winglet starts at y/b=1. The twist is decreased over the wing, even though the lift coefficient is relatively constant. The sweep of the wing will increase the effective angle of attack towards the tip (figure 3.24). Peculiar in the twist distribution is the decrease in twist at the winglet root (y/b=1.08). Interference effects play a large role here, thus decreasing the supervelocities on the winglet section proved to decrease wave drag. The choice was made to unload the winglet more than the outboard wing, as otherwise the lift distribution is altered on the whole outboard wing. A sharp increase in twist angle is seen towards the winglet tip. This increase in loading at the winglet tip increased the L/D of the aircraft by 0.1. Presumably induced drag is decreased, due to a higher downwash of the winglet, countering the tip vortex.

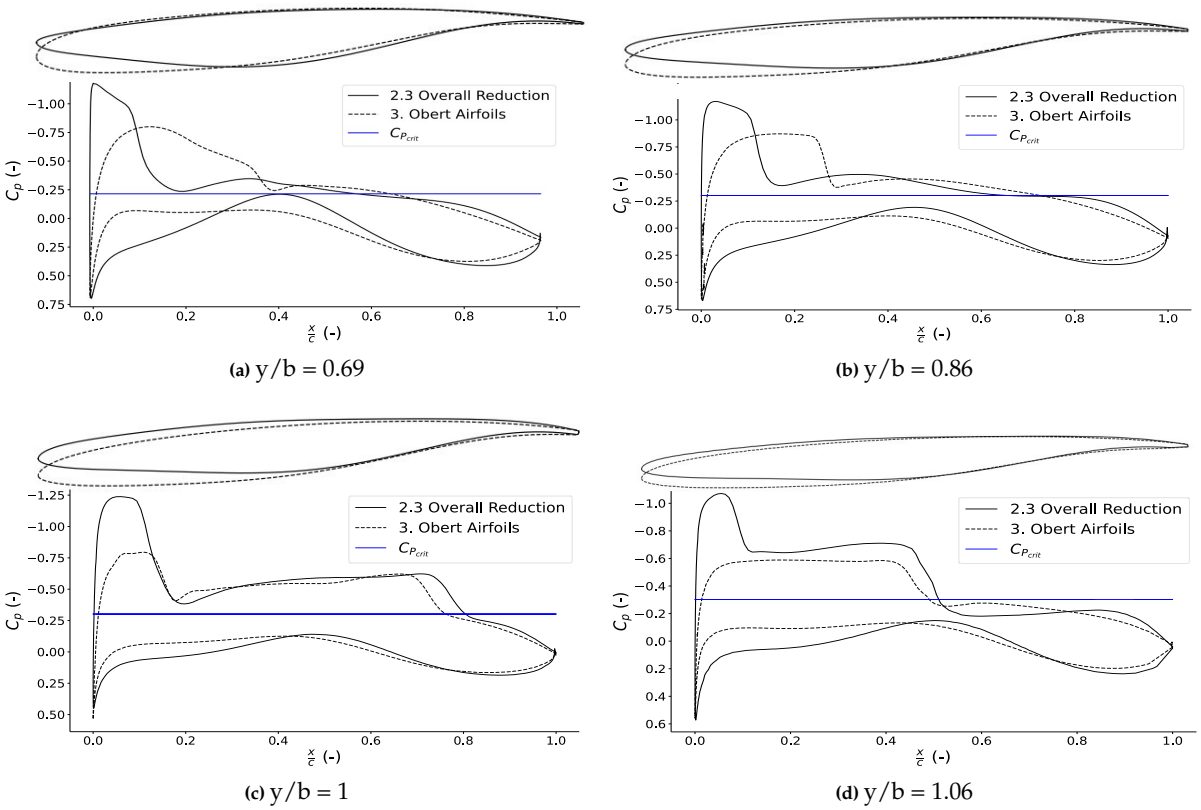

(a) y/b = 0.69 **(b)** y/b = 0.86

(c) y/b = 1 **(d)** y/b = 1.06

Figure 5.16: *2.4.Winglet Optimized* (solid) and *3. Obert Airfoil* (dashed) sections and pressure distributions of the outboard wing (Mach =0.85, Re = 88.3 million, C_L = 0.26)

Figure 5.16 shows the pressure distribution and changes in airfoil shape between iteration phases 2 and 3. The suction peak associated with the sharp nose radius of Faggiano's airfoils is reduced significantly. At the outboard wing root (figure 5.16a) the large suction peak, followed by a strong shock is replaced by an extensive region of isentropic recompression. The maximum Mach number reached is also reduced significantly, to 1.36. The transition from oval section to the sharp nose seen at y/b= 0.69 led to this high-pressure gradient. The rounded nose facilitates a much-improved transition. The front loading which characterized Faggiano's airfoil is absent in the new sections. This is compensated by the extended suction region caused by the isentropic recompression. In the middle section of the outboard wing (figure 5.16b) a stronger shock is present. The shock strength is reduced compared to the Faggiano airfoil. A similar lack of front loading can be seen. The Mach number before the shock reaches 1.3, which is within the buffeting limits described by Obert [43]. At the wing-winglet junction (figure 5.16c) a significant decrease in shock strength of the first shock is seen. The second shock moves forward. Finally on the winglet near the root (figure 5.16d), the double shock is avoided. The thin airfoil leads to a

pressure distribution with a large region of isentropic recompression and a weak shock. The redesigned outboard wing shows a significantly reduced magnitude of Mach numbers and should increase the performance near the high-speed aerodynamic limits.

This iteration (*3. Obert Airfoil*) improves the L/D from 23.9 to 24.2. The Mach number remains high at the leading edge kink. Analysis shows that in this region the flow is isentropically recompressed, however, limiting the risk of buffeting. The performance of this iteration is further explored in section 5.6.2.

5.5. Flying V Root Tail

A strong root effect, concentrating the pressure isobars near the trailing edge, is present on the Flying V. The large sweep angle is the main cause of this root effect. Inspired by the YB-35/49 [1] (figure 5.17a), a tail section at the trailing edge of the root could realign the isobars and reduce the shock strength. Furthermore, the added volume can be useful, for, for example, the auxiliary power unit.

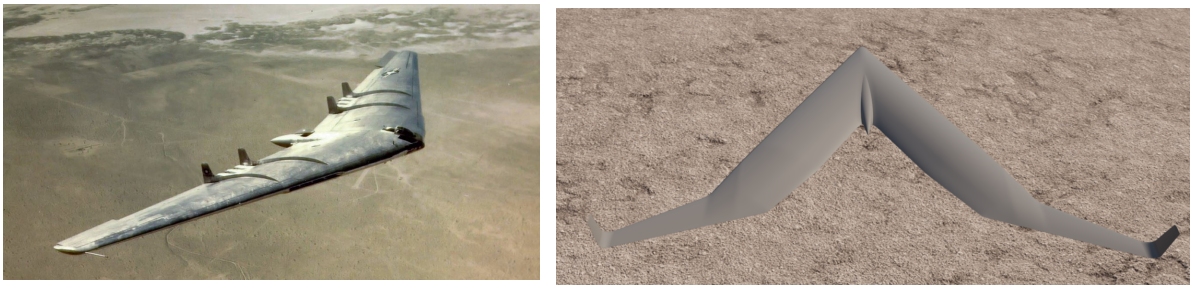

(a) YB-49 bomber prototype[1]

(b) Flying V, tail configuration

Figure 5.17: YB-49 and Flying V showcasing a tail at the root

Figure 5.17b shows a similar tail implemented on the Flying V. The tail trailing edge is positioned slightly higher than the original trailing edge. This, combined with the larger airfoil length, locally decreases the camber. This can be seen in the shock strength. In figure 5.18a the Mach isobars are spaced further apart. In figure 5.18b, the pressure distribution shows a smaller suction peak near the trailing edge for the tail configuration. This also reduces the strength of the shock. This tail configuration decreased the drag coefficient with 0.4 drag counts. With the increase in weight due to the structure the overall efficiency gains will be small, but the extended volume can be a useful addition and the reduced suction peak could mitigate operating limit root issues. A more detailed study of the tail geometry is required to see the impact of the tail on the structure and to optimize the design aerodynamically further.

[1]https://en.wikipedia.org/wiki/Northrop YB-49

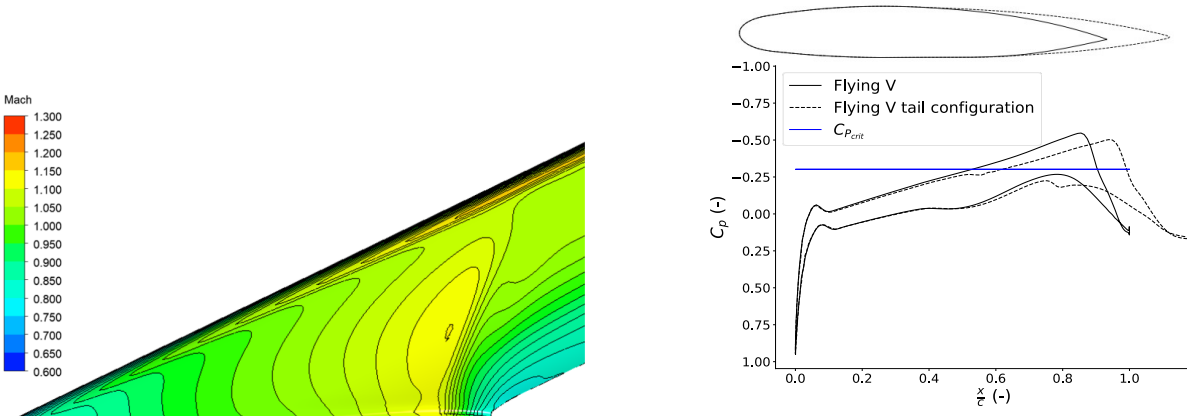

(a) Flying V, tail configuration Mach contours

(b) Flying V, tail configuration root pressure distribution

Figure 5.18: Flying V tail configuration(Mach =0.85, Re = 88.3 million, C_L = 0.26)

5.6. Aerodynamic Characteristics of the Final Design

Design *3.Obert airfoil* shows the highest L/D with acceptable flight characteristics. This section gives an overview of the aerodynamic characteristics of this design. The final L/D achieved is 24.2.

5.6.1. Cruise Characteristics

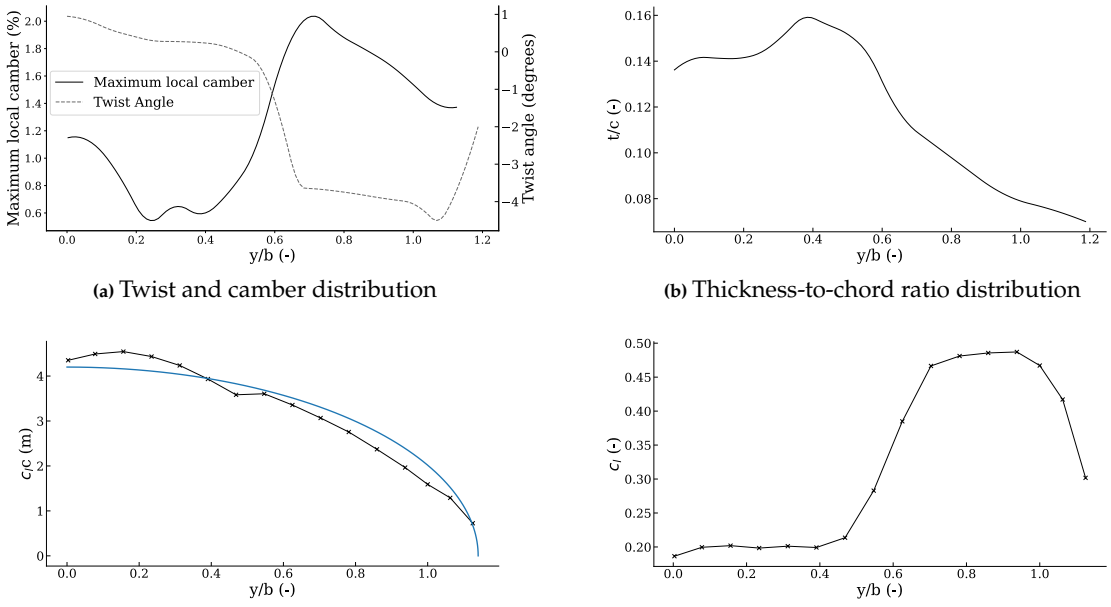

(a) Twist and camber distribution

(b) Thickness-to-chord ratio distribution

(c) Spanwise lift distribution

(d) Section lift distribution

Figure 5.19: Wing twist, t/c and lift distributions of the final design (Mach =0.85, Re = 88.3 million, C_L = 0.26)

Figure 5.19 shows the camber, twist, thickness-to-chord ratio, lift and spanwise lift distributions of the final iteration. The maximum local camber is defined as the maximum distance between camber and chordline, divided by the chord length. An opposite trend in camber and twist angle is seen over the wingspan. As the camber is increased in the airfoil sections, the twist angle is decreased. A steep increase in camber can be perceived at the transition section. This results in an increase in local c_l. The thickness-to-chord ratio also starts to increase in the transition region. The blue line in the spanwise lift chart represents an elliptical lift distribution. Compared to previous iterations, the outboard wing is

loaded relatively lower. The outboard wing shows a relatively triangular lift distribution. Even though a slightly less elliptical lift distribution is achieved, the reduced local lift coefficients help reduce wave drag and excessive magnitude of Mach numbers on the outboard wing. This is partly compensated by a higher lift at the root, where the flow conditions are less critical. The highest thickness-to-chord ratio is reached at approximately y/b = 0.45. A slight drop of lift is observed at this section.

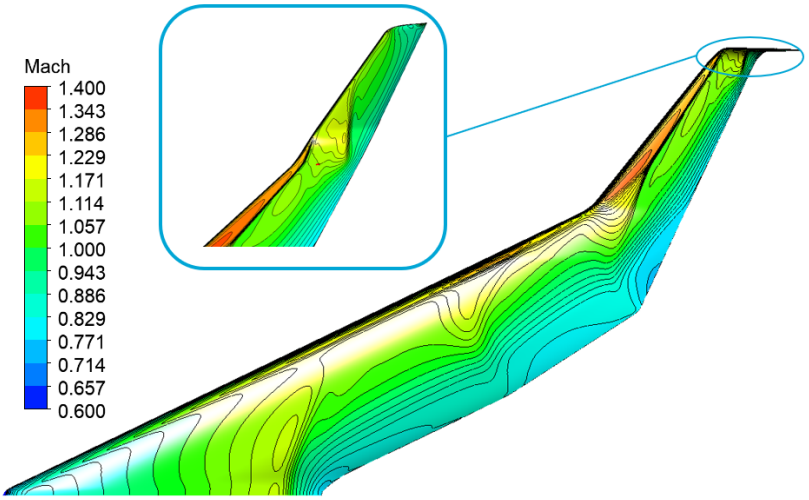

Figure 5.20: Mach number contour of the final design (Mach =0.85, Re = 88.3 million, $C_L = 0.26$)

Figure 5.20 shows the Mach number contour of the final wing. The scale is extended to a Mach number of 1.4 to better visualize the outboard wing, compared to the other Mach number plots. At the root reduced Mach numbers and a reduced shock strength are observed due to the lower loading and section optimization. The middle wing shows reduced pressure peaks and an increase in aft loading. A reduction in Mach numbers on the outboard wing is observed and double shocks on the winglet are mostly avoided. The highest Mach numbers at the leading edge kink are mostly isentropically recompressed.

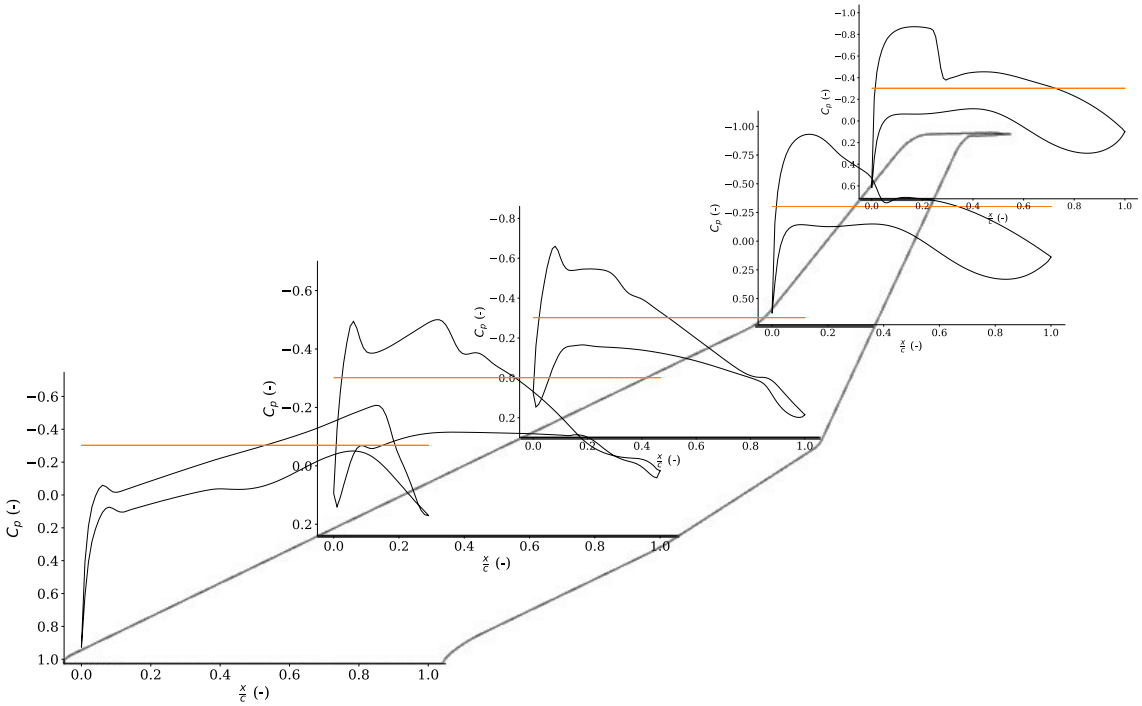

Figure 5.21: Visualisation of pressure distributions (Mach =0.85, Re = 88.3 million, $C_L = 0.26$)

Figure 5.21 shows the pressure distributions at certain wing spanwise sections. Pressure distributions over the full wing can be found in appendix B. At the root, the aforementioned root effect leads to a shock near the trailing edge. The middle sections of the wing show a pressure peak, followed by a region of relatively constant pressure/Mach numbers. The boundary layer thickening, as shown in figure 5.3b, results in similar pressures on the upper and lower surfaces near the trailing edge. This is also reflected in the drag distribution (figure 5.22b). The thick, more highly loaded sections of the wing produce significantly more drag than the inner or outer parts of the wing. The relatively large area of lower pressure, which near the trailing edge has a component in the flight direction, causes significant pressure drag. The large t/c ratio increases the component of the pressure in the flight direction further. The final design does show improvements in this region compared to the baseline. The outboard wing shows supercritical airfoil characteristics, as discussed.

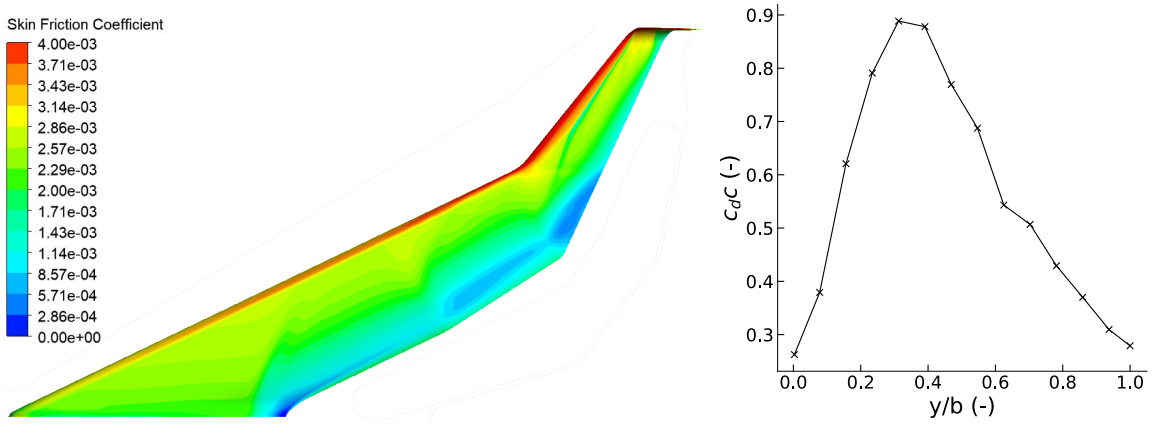

(a) Skin friction coefficient contour of the final design

(b) Drag distribution

Figure 5.22: Flying V Skin friction contour and drag distribution(Mach =0.85, Re = 88.3 million, C_L = 0.26)

The skin friction coefficient contour (figure 5.22a) shows a large skin friction coefficient near the leading edge, which agrees with the thin boundary layer in this region. The skin friction coefficient quickly reduces after a shock due to the thickening of the boundary layer. The boundary layer thickening at the transition section of the wing, near the trailing edge kink, is also clearly visible. It is characterized by a low skin friction coefficient. Simulations at lower Reynolds numbers showed the occurrence of separation in this transition part of the wing. A critical section is the root, where the skin friction coefficient nears 0. Caused by the aft-shock, this remains an area of attention. The Flying V root tail configuration reduces this phenomenon.

5.6.2. Flight Performance and Off-Design Characteristics

	C_L	C_D	C_{Do}	AR	e	S_{ref}	$(C_L/C_D)_{max}$	$C_{L_{opt}}$	AOA_{cruise}	$M_{loc_{max}}$
Flying V Baseline	0.26	122	72	3.59	0.78	906	21.3	0.26	5.3	1.54
Flying V Final Design	0.26	107	62	3.59	0.84	902	24.2	0.27	3.6	1.36

Table 5.4: Comparison of aerodynamic and planform characteristics of the baseline and final design. Drag coefficients are in drag counts

Table 5.4 shows a summary of planform and aerodynamic characteristics of the baseline and final design. The final design has a significantly lower zero drag coefficient. This can partly be explained by the fact that at zero lift a larger supersonic region on the lower side of the outer airfoil can be perceived on the baseline, creating drag. This is caused by the relatively low loading of the outboard wing on the baseline design and the airfoil shape. The final design shows a slightly higher Oswald efficiency factor. This can be explained by the more elliptical lift distribution. The Oswald efficiency factor was

computed based on a quadratic lift polar, using least-squares regression to compute the slope $\frac{dC_d}{d(C_L^2)}$. It should be noted that the Oswald efficiency factor showed changing behaviour with different ranges of lift coefficients. The non-linearities due to the transonic nature of the flow might cause discrepancies.

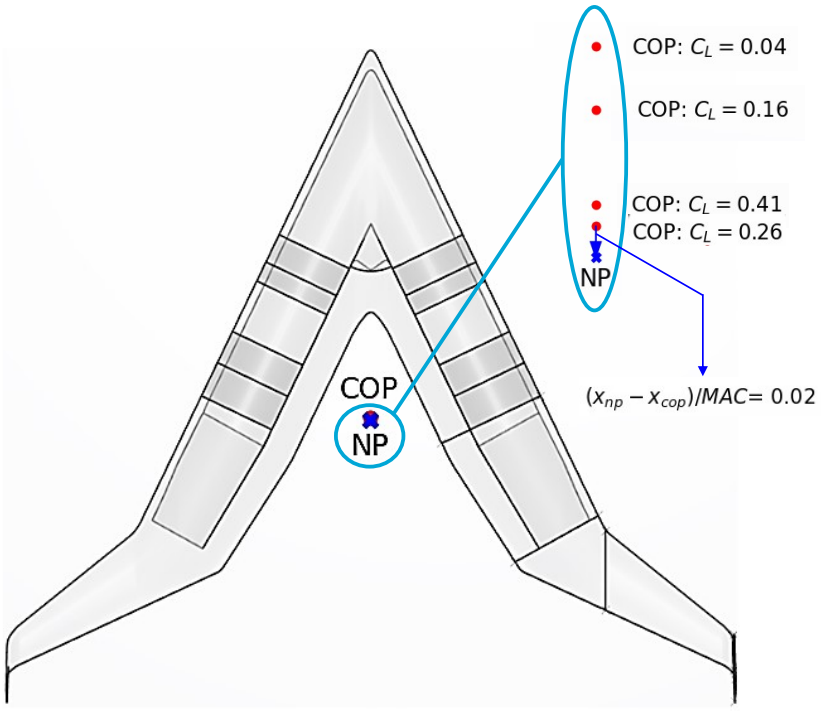

Figure 5.23: Center of pressure (COP) and neutral point (NP) (Mach =0.85, Re = 88.3 million)

Next to the aerodynamic efficiency, static longitudinal stability should be ensured, while minimizing trim drag. This requirement is quantified as equation 3.58. This ensures the neutral point is behind the centre of pressure. The centre of gravity can be designed such that it coincides with the centre of pressure, ensuring static longitudinal stability and minimizing trim drag. Figure 5.23 shows the centre of pressure and neutral point at different angles of attack in cruise conditions. The center of pressure moves backwards at increasing angle of attack, until non-linear behaviour starts occurring in the $C_L - \alpha$ curve. The centre of pressure starts moving forward again at this point. This indicates the outboard wing starts stalling first. The wing has been designed such that the centre of pressure, at the design lift coefficient of 0.26, is 2% of the mean aerodynamic chord length in front of the neutral point, which is a required static margin. The neutral point and centre of pressure in design condition are located 32.7 and 32.4 meters from the nose of the aircraft respectively.

Figure 5.24 shows the off-design performance of the Flying V. The lift curve (figure 5.24a) shows linear behaviour up to an angle of attack of 5 degrees. It was already shown that the centre of pressure starts to move forward around this angle of attack. The lift-to-drag ratio (figure 5.24b) also decreases rapidly in this angle of attack range. The maximum lift-to-drag ratio reached is 24.25 at an angle of attack of 3.79 with a C_L of 0.27. There is a plateau around the maximum L/D, so a wider range of lift coefficients remains efficient. The drag polar (figure 5.24c) shows parabolic behaviour, but wave drag also plays a role in the drag polar. The drag divergence curve is presented in figure 5.24d. The drag divergence Mach number is taken as the Mach number where $dC_D/dM = 0.10$, used by Airbus and Douglas[64]. This occurs at a Mach number of 0.925. A plateau in drag coefficient is seen between Mach numbers of 0.75 and 0.85. Around the design Mach number the drag coefficient starts to rise as wave drag starts to increase. At a Mach number of 0.7, the drag coefficient rises slightly. This is caused by the increased angle of attack at lower Mach numbers, which leads to relatively high pressure peaks and stronger shocks.

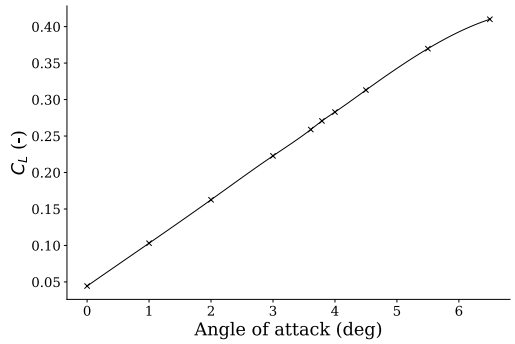

(a) Lift curve (Mach = 0.85, Re= 88.3e6)

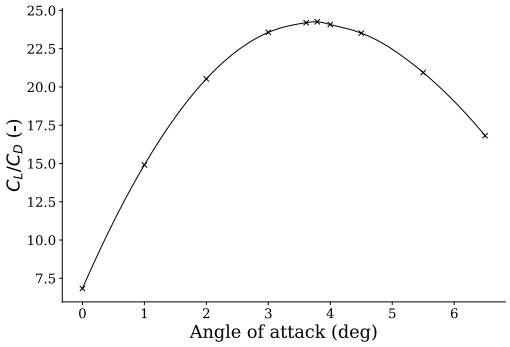

(b) Lift-to-drag ratio at different angles of attack (Mach = 0.85, Re= 88.3e6)

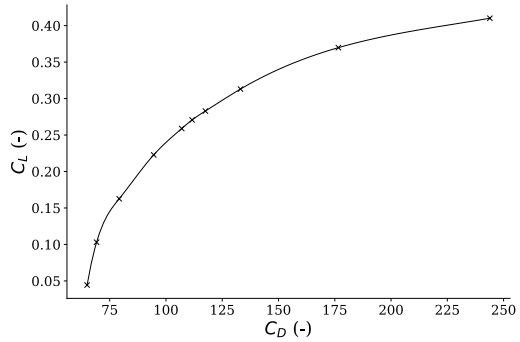

(c) Drag polar (Mach = 0.85, Re= 88.3e6)

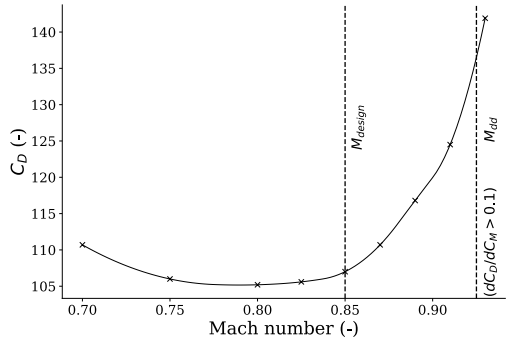

(d) Drag divergence curve ($C_L = 0.26$)

Figure 5.24: Off-design curves at different flight conditions. The drag coefficient is reported in drag counts

It should be noted that the RANS simulations used to generate the off-design data do not predict unsteady effects such as high-speed buffeting. The real drag divergence and stall angles might be limited by unsteady effects. The simulations also become less reliable when large regions of separation occur, so the (high-speed) stall results are an estimation that should be confirmed in later work.

6

Conclusion and Recommendations

6.1. Conclusion

With the airline industry almost recovered from the COVID-19 pandemic, the focus on the long-term future can be regained. With expectations of a doubling in passenger traffic in 2040, this growth leads to significant environmental challenges. Part of the solution lies in a more efficient aircraft shape, increasing the lift-to-drag ratio (L/D). Benad envisioned a flying-wing aircraft where payload and fuel both reside in a V-shaped, crescent wing with large winglets that double as vertical tail planes: the Flying V. As the passengers sit in the V-shaped wing, the lift-producing area is increased significantly with respect to a traditional aircraft, while the wetted area is reduced. Based on the previous Flying V studies, a new parametrization of the Flying V was constructed by Benad. A need for detailed aerodynamic optimization has arisen to maximize the efficiency of this design. This thesis project aims to maximize the lift-to-drag ratio of the Flying V in cruise conditions by means of a high-fidelity CFD investigation.

The design parameters that describe the outer mold line of the Flying V are manually modified and the aerodynamic performance of the aircraft is assessed by means of computational fluid dynamics. The aircraft is parameterized in CATIA, based on previously performed work. The CATIA model ensures a smooth transition between different wing sections. The oval retention parameter (ORT) is introduced, which dictates the position where the oval inner structure stops and the interpolation to the airfoil section starts. The Reynolds-averaged Navier–Stokes equations (RANS) equations are solved to obtain the numerical results. A structured mesh consisting of 15 million nodes with a grid convergence index of 0.01% discretizes the fluid domain. The solver includes a 3rd-order MUSCL spatial discretization, where fluxes are computed using the Roe Flux-Difference Splitting Scheme. The low-Reynolds, Menter SST turbulence model is used. Next to the three-dimensional optimization, a two-dimensional gradient-based airfoil optimization is set up to generate airfoils suitable for the outboard wing. The numerical set-up is validated using ONERA M6 validation data.

The baseline design showed excessive wave drag on the outboard wing and a lack of spanwise lift at the mid-wing. Three design phases were conducted. In phase 1, several iterations were conducted, during which the inboard, mid and outboard wing sections were optimized, focusing both on elliptical lift and section performance. A lack of lift in the middle section was resolved by an increase in camber and aft-loading. Improved airfoil sections on the outboard wing were better capable of efficiently generating the required lift coefficient for more elliptical lift. The lift-to-drag ratio obtained was 23.1 at an angle of attack of 3.5 degrees. The second phase consisted of a planform optimization, where small changes were performed to redistribute and reduce wing area. This increased the lift-to-drag ratio to 23.7. In the third phase, the airfoil optimization proved to not increase the L/D. Airfoils obtained from Obert proved to increase efficiency and reduce Mach numbers on the outboard wing. An optimization of winglet incidence angles and profiles largely removed the double shock witnessed in the baseline and reduced the maximum Mach number at the wing-winglet junction to 1.255. The maximum lift-to-drag ratio obtained was 24.2 at an angle of attack of 3.6 degrees, compared to 21.3 and 5.2 degrees of the baseline (Mach = 0.85, C_L =0.26, Re = 88.3 million). The drag divergence Mach number is estimated at 0.925.

6.2. Recommendations for Future Work

This study showed relatively significant improvements using a manual iteration approach. Additional research is however required to further optimize the design and ensure the design is safe and efficient over a wide range of flight conditions. In particular, the middle section of the wing, outboard of the trailing edge kink, shows a high drag coefficient distribution and low skin-friction coefficient. Future

studies should investigate the unsteady effects of the boundary layer thickening, as the RANS simulation does not include these effects. If unsteady effects prove to be significant, planform changes might be required to reduce the thickness-to-chord ratio in this area, or the local loading might have to be reduced.

To further improve the design, the outboard wing might benefit from parametrization changes. Airfoils and incidence angles are only specified at the root and tip in the current parametrization. This leads to a linear twist distribution on the outer wing. This study showed the importance of the wing-winglet junction in terms of wave drag. This limits the acceptable local lift coefficient at the tip. As a consequence, the outboard wing shows a more triangular than elliptical lift distribution. Defining more outboard wing sections to depart from a linear twist distribution, might help increase the efficiency of the outboard wing. It might also be beneficial to position the airfoils orthogonal to the leading edge of the wing instead of parallel to the flow. The effect of sweep can more easily be researched where classical airfoils are used orthogonal to the leading edge. Furthermore, the airfoil profiles selected are not necessarily optimized for the flight conditions described in the results section. An (algorithm-led) redesign of the profiles and incidence angles could improve performance of the outboard wing. The two-dimensional optimisation of this study did show the importance of geometrical constraints on a future algorithm-led optimization, as the airfoils should remain efficient at different flight conditions and angles of attack.

The root remains an area of concern. The aft-shock wave caused by the root effect resulted in an area of an almost zero skin-friction coefficient. The unsteady effects of this region should be further investigated, to see if this causes any buffeting. The Flying V root tail was presented as a partial solution. The root tail remains unoptimized. Different angles, sizes and lengths could reduce the intensity of the shock. The three-dimensional effects this tail has on the area surrounding the root should also be further investigated.

Next to the on-design performance, the off-design importance should be further investigated. The Mach drag divergence study showed that at higher angles of attacks (at lower Mach numbers), large suction peaks occur at the outboard wing. This might also influence the low-speed aerodynamic performance of the aircraft. Slats might be required at take-off and landing conditions to ensure safe flight. The overall low-speed performance of the new design has to be evaluated. Longitudinal static stability was ensured in this study. Lateral and dynamic stabilities should be further investigated.

The final section of this study focused on the aerodynamic flight performance of the aircraft. Even though the drag divergence Mach number was estimated at 0.925, the reliability of the RANS code becomes questionable in this flight regime. The RANS code also does not predict buffeting. Unsteady simulations or wind tunnel testing will be required to more reliably estimate the drag divergence characteristics of the aircraft. This study aimed to give a first estimation.

References

[1] *Ansys Fluent Theory Guide*. ANSYS inc., July 2022.

[2] *ANSYS Fluent User's Guide*. ANSYS inc., Nov. 2013.

[3] *Ansys Icem CFD Help Manual*. en. ANSYS inc., July 2021. (Visited on 08/07/2023).

[4] Guillermo Araya. "Turbulence Model Assessment in Compressible Flows around Complex Geometries with Unstructured Grids". en. In: *Fluids* 4.2 (Apr. 2019), p. 81. ISSN: 2311-5521. DOI: 10.3390/fluids4020081. URL: https://www.mdpi.com/2311-5521/4/2/81 (visited on 01/10/2023).

[5] J. Benad. "The Flying V A new Aircraft Configuration for Commercial Passenger Transport". en. In: (2015). Publisher: Deutsche Gesellschaft für Luft- und Raumfahrt - Lilienthal-Oberth e.V., 8 pages. DOI: 10.25967/370094. (Visited on 12/07/2022).

[6] J. Benad and R. Vos. *Aerial vehicle*. Delft University of Technology: Patent application N2034242, 2023.

[7] J. Benad and Roelof Vos. "Design of a Flying V Subsonic Transport". en. In: *ICAS 2022* (2022). URL: https://repository.tudelft.nl/islandora/object/uuid%3A95ea413d-d5b1-4cb2-a650-828cb106dbbd (visited on 05/17/2023).

[8] Justus Benad. "Development of a numerical flow channel with the Lattice Boltzmann method and application to highly swept wings at high angles of attack". en. In: (2022). Publisher: Technische Universität Berlin. DOI: 10.14279/DEPOSITONCE-15208. URL: https://depositonce.tu-berlin.de/handle/11303/16432 (visited on 12/09/2022).

[9] Jiri Blazek. *Computational Fluid Dynamics: Principles and Applications*. English. 3rd edition. Amsterdam: Butterworth-Heinemann, Apr. 2015. ISBN: 978-0-08-099995-1.

[10] Yaïr Brouwer. "Constrained Aerodynamic Optimization of the Flying-V Nose Cone and Center-Body Fairing". en. In: (2022). URL: https://repository.tudelft.nl/islandora/object/uuid%3A4f9eea41-8dbc-4947-b599-46647b3e365b (visited on 12/05/2022).

[11] Marco Ceze, Marcelo Hayashi, and Ernani Volpe. "A Study of the CST Parameterization Characteristics". In: June 2009. DOI: 10.2514/6.2009-3767.

[12] Zhenli Chen et al. "Assessment on critical technologies for conceptual design of blended-wing-body civil aircraft". en. In: *Chinese Journal of Aeronautics* 32.8 (Aug. 2019), pp. 1797–1827. ISSN: 10009361. DOI: 10.1016/j.cja.2019.06.006. URL: https://linkinghub.elsevier.com/retrieve/pii/S1000936119302493 (visited on 12/16/2022).

[13] *COVID-19 impact on the European air traffic network*. en. URL: https://www.eurocontrol.int/covid19 (visited on 01/31/2023).

[14] Adrien Crovato et al. "Effect of Levels of Fidelity on Steady Aerodynamic and Static Aeroelastic Computations". en. In: *Aerospace* 7.4 (Apr. 2020), p. 42. ISSN: 2226-4310. DOI: 10.3390/aerospace7040042. URL: https://www.mdpi.com/2226-4310/7/4/42 (visited on 05/09/2023).

[15] Defense Technical Information Center. *DTIC ADA073982: Experimental Data Base for Computer Program Assessment*. May 1979. URL: http://archive.org/details/DTIC_ADA073982 (visited on 08/11/2023).

[16] F. Faggiano. "Aerodynamic Design Optimization of a Flying V Aircraft". en. In: (2016). URL: https://repository.tudelft.nl/islandora/object/uuid%3A0b1472a5-3aad-433c-9a64-242c84b114fd (visited on 12/07/2022).

[17] Francesco Faggiano et al. "Aerodynamic Design of a Flying V Aircraft". en. In: *17th AIAA Aviation Technology, Integration, and Operations Conference*. Denver, Colorado: American Institute of Aeronautics and Astronautics, June 2017. ISBN: 978-1-62410-508-1. DOI: 10.2514/6.2017-3589. URL: https://arc.aiaa.org/doi/10.2514/6.2017-3589 (visited on 12/05/2022).

[18] A Favre. "Equations des Gaz Turbulents Compressibles". In: *Journal de Mecanique* Vol. 4 (1965), pp. 361–390.

[19] Joel H. Ferziger and Milovan Perić. *Computational Methods for Fluid Dynamics*. en. Berlin, Heidelberg: Springer, 2002. ISBN: 978-3-540-42074-3 978-3-642-56026-2. DOI: 10.1007/978-3-642-56026-2. URL: http://link.springer.com/10.1007/978-3-642-56026-2 (visited on 12/19/2022).

[20] *Global Market Forecast | Airbus*. en. Section: Commercial Aircraft. June 2021. URL: https://www.airbus.com/en/products-services/commercial-aircraft/market/global-market-forecast (visited on 01/31/2023).

[21] Falk Götten et al. "A review of guidelines and best practices for subsonic aerodynamic simulations using RANS CFD". In: Dec. 2019.

[22] Charles D. Harris. *NASA supercritical airfoils: A matrix of family-related airfoils*. NTRS Author Affiliations: NASA Langley Research Center NTRS Report/Patent Number: NASA-TP-2969 NTRS Document ID: 19900007394 NTRS Research Center: Legacy CDMS (CDMS). Mar. 1990. URL: https://ntrs.nasa.gov/citations/19900007394 (visited on 01/23/2023).

[23] Marleen Hillen. "Parametrisation of the Flying-V Outer Mould Line". en. In: (2020). URL: https://repository.tudelft.nl/islandora/object/uuid%3Af4863ae4-2792-4335-b929-ff9dfdb6fed5 (visited on 12/08/2022).

[24] Dominik Hofer. *Matlab to Ansys ICEM/Fluent and Spline Drawing Toolbox*. en. Aug. 2023. URL: https://nl.mathworks.com/matlabcentral/fileexchange/66215-matlab-to-ansys-icem-fluent-and-spline-drawing-toolbox (visited on 08/03/2023).

[25] B. R. Hutchinson and G. D. Raithby. "A MULTIGRID METHOD BASED ON THE ADDITIVE CORRECTION STRATEGY". en. In: *Numerical Heat Transfer* 9.5 (May 1986), pp. 511–537. ISSN: 0149-5720. DOI: 10.1080/10407788608913491. URL: http://www.tandfonline.com/doi/abs/10.1080/10407788608913491 (visited on 12/30/2022).

[26] The MathWorks Inc. *Choosing the Algorithm*. Sept. 2023. URL: https://nl.mathworks.com/help/optim/ug/choosing-the-algorithm.html.

[27] Nelson Johnson. "Effect of Winglet Integration and Rudder Deflection on Flying-V Aerodynamic Characteristics". en. In: (2021). URL: https://repository.tudelft.nl/islandora/object/uuid%3Ab664ae03-846f-4ad3-849a-c081a32260ad (visited on 12/09/2022).

[28] Sjoerd Joosten. "Piloted Assessment of the Lateral-Directional Handling Qualities of the Flying-V". en. In: (2022). URL: https://repository.tudelft.nl/islandora/object/uuid%3A092de789-1947-4554-91b2-cc357383b94c (visited on 12/13/2022).

[29] John D. Anderson Jr. *Fundamentals of Aerodynamics*. en. Google-Books-ID: xwY8PgAACAAJ. McGraw-Hill Education, Feb. 2010. ISBN: 978-0-07-339810-5.

[30] Anastasia Kharina and Daniel Rutherford. *Fuel Efficiency Trends for New Commercial Jet Aircraft: 1960 to 2014*. Aug. 2015.

[31] Brenda Kulfan and John Bussoletti. ""Fundamental" Parameteric Geometry Representations for Aircraft Component Shapes". In: *11th AIAA/ISSMO Multidisciplinary Analysis and Optimization Conference*. _eprint: https://arc.aiaa.org/doi/pdf/10.2514/6.2006-6948. American Institute of Aeronautics and Astronautics. DOI: 10.2514/6.2006-6948. URL: https://arc.aiaa.org/doi/abs/10.2514/6.2006-6948 (visited on 08/03/2023).

[32] Alexander Kurganov and Eitan Tadmor. "New High-Resolution Central Schemes for Nonlinear Conservation Laws and Convection–Diffusion Equations". en. In: *Journal of Computational Physics* 160.1 (May 2000), pp. 241–282. ISSN: 00219991. DOI: 10.1006/jcph.2000.6459. URL: https://linkinghub.elsevier.com/retrieve/pii/S0021999100964593 (visited on 12/27/2022).

[33] R. H. Liebeck. "Design of the Blended Wing Body Subsonic Transport". en. In: *Journal of Aircraft* 41.1 (Jan. 2004), pp. 10–25. ISSN: 0021-8669, 1533-3868. DOI: 10.2514/1.9084. URL: https://arc.aiaa.org/doi/10.2514/1.9084 (visited on 09/05/2023).

[34] Zhoujie Lyu and Joaquim R. R. A. Martins. "Aerodynamic Design Optimization Studies of a Blended-Wing-Body Aircraft". en. In: *Journal of Aircraft* 51.5 (Sept. 2014), pp. 1604–1617. ISSN: 0021-8669, 1533-3868. DOI: 10.2514/1.C032491. URL: https://arc.aiaa.org/doi/10.2514/1.C032491 (visited on 12/14/2022).

[35] M Meheut et al. "Aerodynamic Design of Transonic Flying Wing Configurations". In: Jan. 2009.

[36] F. R. Menter. "Two-equation eddy-viscosity turbulence models for engineering applications". en. In: *AIAA Journal* 32.8 (Aug. 1994), pp. 1598–1605. ISSN: 0001-1452, 1533-385X. DOI: 10.2514/3.12149. URL: https://arc.aiaa.org/doi/10.2514/3.12149 (visited on 12/22/2022).

[37] J. E. Michael and M.A.R Sharif. *EFFECT OF SURFACE ROUGHNESS ON TURBULENT TRANSONIC FLOW AROUND A RAE-2822 AIRFOIL*. Dec. 2005.

[38] Alan Le Moigne and Ning Qin. "Variable-Fidelity Aerodynamic Optimization for Turbulent Flows Using a Discrete Adjoint Formulation". en. In: *AIAA Journal* 42.7 (July 2004), pp. 1281–1292. ISSN: 0001-1452, 1533-385X. DOI: 10.2514/1.2109. URL: https://arc.aiaa.org/doi/10.2514/1.2109 (visited on 05/09/2023).

[39] Eric J. Nielsen and W. Kyle Anderson. "Recent Improvements in Aerodynamic Design Optimization on Unstructured Meshes". en. In: *AIAA Journal* 40.6 (June 2002), pp. 1155–1163. ISSN: 0001-1452, 1533-385X. DOI: 10.2514/2.1765. URL: https://arc.aiaa.org/doi/10.2514/2.1765 (visited on 05/09/2023).

[40] Ties Nieuwenhuizen. "Conceptual Design Optimisation of a Flying V Aircraft". en. In: (2021). URL: https://repository.tudelft.nl/islandora/object/uuid%3Aec1cbf97-f795-476a-87e3-066c3736b618 (visited on 12/08/2022).

[41] NLR. *A ROUTE TO NET ZERO EUROPEAN AVIATION*. Feb. 2021. URL: https://www.destination2050.eu/wp-content/uploads/2021/02/Destination2050_ExecutiveSummary.pdf.

[42] NPARC. "Verification Assessment". In: (Oct. 2021). URL: https://www.grc.nasa.gov/www/wind/valid/tutorial/verassess.html.

[43] Ed Obert. *Aerodynamic Design of Transport Aircraft*. en. Google-Books-ID: V1DuJfPov48C. IOS Press, 2009. ISBN: 978-1-58603-970-7.

[44] Paul Okonkwo and Howard Smith. "Review of evolving trends in blended wing body aircraft design". en. In: *Progress in Aerospace Sciences* 82 (Apr. 2016), pp. 1–23. ISSN: 03760421. DOI: 10.1016/j.paerosci.2015.12.002. URL: https://linkinghub.elsevier.com/retrieve/pii/S0376042115300336 (visited on 12/14/2022).

[45] Wilco Oosterom and Roelof Vos. "Conceptual Design of a Flying-V Aircraft Family". en. In: *AIAA AVIATION 2022 Forum*. Chicago, IL & Virtual: American Institute of Aeronautics and Astronautics, June 2022. ISBN: 978-1-62410-635-4. DOI: 10.2514/6.2022-3200. URL: https://arc.aiaa.org/doi/10.2514/6.2022-3200 (visited on 12/08/2022).

[46] Simon van Overeem, Xuerui Wang, and Erik-Jan Van Kampen. "Modelling and Handling Quality Assessment of the Flying-V Aircraft". en. In: *AIAA SCITECH 2022 Forum*. San Diego, CA & Virtual: American Institute of Aeronautics and Astronautics, Jan. 2022. ISBN: 978-1-62410-631-6. DOI: 10.2514/6.2022-1429. URL: https://arc.aiaa.org/doi/10.2514/6.2022-1429 (visited on 12/13/2022).

[47] Stephen B. Pope. *Turbulent Flows*. 1st ed. Cambridge University Press, Aug. 2000. ISBN: 978-0-521-59125-6 978-0-521-59886-6 978-0-511-84053-1. DOI: 10.1017/CBO9780511840531. URL: https://www.cambridge.org/core/product/identifier/9780511840531/type/book (visited on 12/19/2022).

[48] M. J. D. Powell. "A fast algorithm for nonlinearly constrained optimization calculations". en. In: *Numerical Analysis*. Ed. by G. A. Watson. Lecture Notes in Mathematics. Berlin, Heidelberg: Springer, 1978, pp. 144–157. ISBN: 978-3-540-35972-2. DOI: 10.1007/BFb0067703.

[49] N. Qin et al. "Aerodynamic considerations of blended wing body aircraft". en. In: *Progress in Aerospace Sciences* 40.6 (Aug. 2004), pp. 321–343. ISSN: 03760421. DOI: 10.1016/j.paerosci.2004.08.001. URL: https://linkinghub.elsevier.com/retrieve/pii/S0376042104000569 (visited on 12/14/2022).

[50] P.J. Roache, K. Ghia, and White. "Procedure for Estimation and Reporting of Uncertainty Due to Discretization in CFD Applications". en. In: *Journal of Fluids Engineering* 130.7 (2008), p. 078001. ISSN: 00982202. DOI: 10.1115/1.2960953. URL: http://FluidsEngineering.asmedigitalcollection.asme.org/article.aspx?articleid=1434171 (visited on 04/25/2023).

[51] P L Roe. "Characteristic-Based Schemes for the Euler Equations". en. In: *Annual Review of Fluid Mechanics* 18.1 (Jan. 1986), pp. 337–365. ISSN: 0066-4189, 1545-4479. DOI: 10.1146/annurev.fl.18.010186.002005. URL: https://www.annualreviews.org/doi/10.1146/annurev.fl.18.010186.002005 (visited on 12/29/2022).

[52] Dino Roman, Richard Gilmore, and Sean Wakayama. "Aerodynamics of High-Subsonic Blended-Wing-Body Configurations". en. In: *41st Aerospace Sciences Meeting and Exhibit*. Reno, Nevada: American Institute of Aeronautics and Astronautics, Jan. 2003. ISBN: 978-1-62410-099-4. DOI: 10.2514/6.2003-554. URL: https://arc.aiaa.org/doi/10.2514/6.2003-554 (visited on 12/14/2022).

[53] Christopher L. Rumsey and Richard A. Wahls. "Focused Assessment of State-of-the-Art CFD Capabilities for Prediction of Subsonic Fixed Wing Aircraft Aerodynamics". In: NTRS Author Affiliations: NASA Langley Research Center NTRS Report/Patent Number: L-19484 NTRS Document ID: 20080023857 NTRS Research Center: Langley Research Center (LaRC). June 2008. URL: https://ntrs.nasa.gov/citations/20080023857 (visited on 01/13/2023).

[54] Hermann Schlichting and Klaus Gersten. *Boundary-Layer Theory*. en. Berlin, Heidelberg: Springer Berlin Heidelberg, 2017. ISBN: 978-3-662-52917-1 978-3-662-52919-5. DOI: 10.1007/978-3-662-52919-5. URL: http://link.springer.com/10.1007/978-3-662-52919-5 (visited on 01/12/2023).

[55] V. Schmitt and F. Charpin. "Pressure distributions on the ONERA M6 wing at transonic Mach numbers". In: 1979. URL: https://www.semanticscholar.org/paper/Pressure-distributions-on-the-ONERA-M6-wing-at-Mach-Schmitt-Charpin/6498e2b6c38d7da95a07fe539bbf8525eba8f730 (visited on 01/13/2023).

[56] Ralph L Schwader. "The Development of the Flying Wing". en. In: *Journal of Aviation/Aerospace Education & Research* 8.1 (Jan. 1997). ISSN: 2329-258X. DOI: 10.58940/2329-258X.1212. URL: https://commons.erau.edu/jaaer/vol8/iss1/4 (visited on 08/25/2023).

[57] P. Spalart and S. Allmaras. "A one-equation turbulence model for aerodynamic flows". en. In: *30th Aerospace Sciences Meeting and Exhibit*. Reno,NV,U.S.A.: American Institute of Aeronautics and Astronautics, Jan. 1992. DOI: 10.2514/6.1992-439. URL: https://arc.aiaa.org/doi/10.2514/6.1992-439 (visited on 12/22/2022).

[58] Philippe Spalart. "Trends in turbulence treatments". en. In: *Fluids 2000 Conference and Exhibit*. Denver,CO,U.S.A.: American Institute of Aeronautics and Astronautics, June 2000. DOI: 10.2514/6.2000-2306. URL: https://arc.aiaa.org/doi/10.2514/6.2000-2306 (visited on 01/12/2023).

[59] Jiyuan Tu, Guan Heng Yeoh, and Chaoqun Liu. *Computational fluid dynamics: a practical approach*. English. Third edition. Amsterdam: Butterworth-Heinemann, 2018. ISBN: 978-0-08-101244-4. URL: https://www.sciencedirect.com/science/book/9780081011270 (visited on 01/11/2023).

[60] Jeroen van Uitert. "Experimental Investigation into the Effect of Aerodynamic Add-ons on the Aerodynamic Characteristics of the Flying V". en. In: (2021). URL: https://repository.tudelft.nl/islandora/object/uuid%3Afdfff622-792c-4d54-a048-b59abf477a11 (visited on 12/09/2022).

[61] Nikki Van Luijk and Roelof Vos. "Constrained Aerodynamic Shape Optimisation of the Flying V Outer Wing". en. In: *AIAA AVIATION 2023 Forum*. San Diego, CA and Online: American Institute of Aeronautics and Astronautics, June 2023. ISBN: 978-1-62410-704-7. DOI: 10.2514/6.2023-3250. URL: https://arc.aiaa.org/doi/10.2514/6.2023-3250 (visited on 08/24/2023).

[62] Rob Viet. "Analysis of the flight characteristics of a highly swept cranked flying wing by means of an experimental test". en. In: (2019). URL: https://repository.tudelft.nl/islandora/object/uuid%3A90de4d9e-70ae-4efc-bd0a-7426a0a669c3 (visited on 12/09/2022).

[63] R. Vos, F.J.J.M.M. Geuskens, and M.F.M. Hoogreef. "A New Structural Design Concept for Blended Wing Body Cabins". en. In: *53rd AIAA/ASME/ASCE/AHS/ASC Structures, Structural Dynamics and Materials Conference
20th AIAA/ASME/AHS Adaptive Structures Conference
14th AIAA*. Honolulu, Hawaii: American Institute of Aeronautics and Astronautics, Apr. 2012. ISBN: 978-1-60086-937-2. DOI: 10.2514/6.2012-1998. URL: http://arc.aiaa.org/doi/abs/10.2514/6.2012-1998 (visited on 12/12/2022).

[64] Roelof Vos and Saeed Farokhi. *Introduction to Transonic Aerodynamics*. Vol. 110. Fluid Mechanics and Its Applications. Dordrecht: Springer Netherlands, 2015. ISBN: 978-94-017-9746-7 978-94-017-9747-4. DOI: 10.1007/978-94-017-9747-4. URL: http://link.springer.com/10.1007/978-94-017-9747-4 (visited on 01/16/2023).

[65] P. Weiand. “Transonic Aerodynamics in Conceptual Aircraft Design”. en. In: (Jan. 2014). Publisher: Deutsche Gesellschaft für Luft- und Raumfahrt - Lilienthal-Oberth e.V., Bonn. URL: https://publikationen.dglr.de/?tx_dglrpublications_pi1[document_id]=301283 (visited on 01/16/2023).

[66] R. T. Whitcomb. “Review of NASA supercritical airfoils”. In: NTRS Author Affiliations: NASA Langley Research Center NTRS Report/Patent Number: ICAS PAPER 74-10 NTRS Document ID: 19740058562 NTRS Research Center: Legacy CDMS (CDMS). Haifa, Aug. 1974. URL: https://ntrs.nasa.gov/citations/19740058562 (visited on 01/23/2023).

[67] David C. Wilcox. *Turbulence Modeling for CFD*. English. 3rd edition. La Cãnada, Calif: D C W Industries, Nov. 2006. ISBN: 978-1-928729-08-2.

7

Appendix A: ONERA M6 Validation Data

Appendix A shows all pressure distribution comparison data of the ONERA M6 experimental validation.

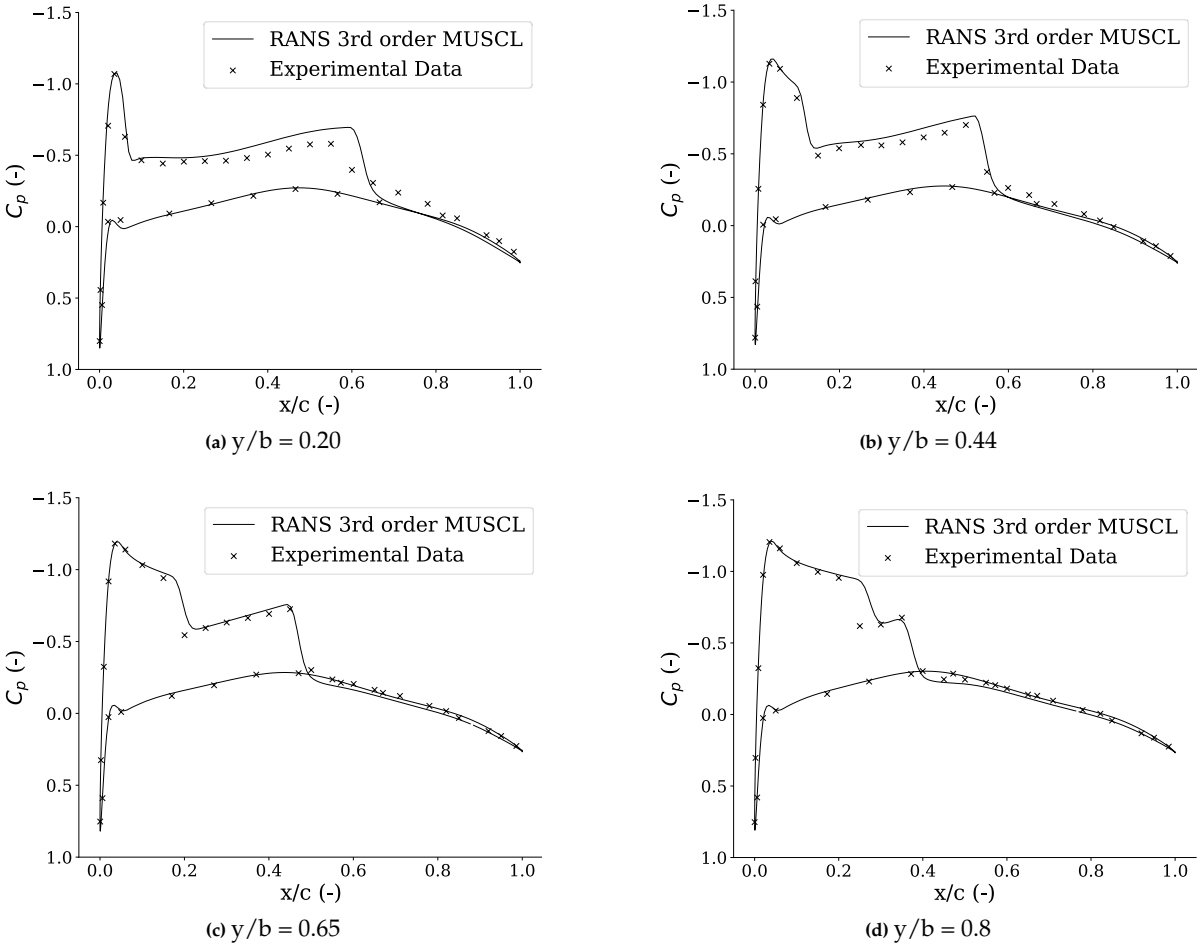

(a) y/b = 0.20 **(b)** y/b = 0.44

(c) y/b = 0.65 **(d)** y/b = 0.8

Figure 7.1: Pressure distribution validation on the ONERA M6 wing (Mach = 0.8395, AOA = 3.06 degrees, Re = 11.72 million)

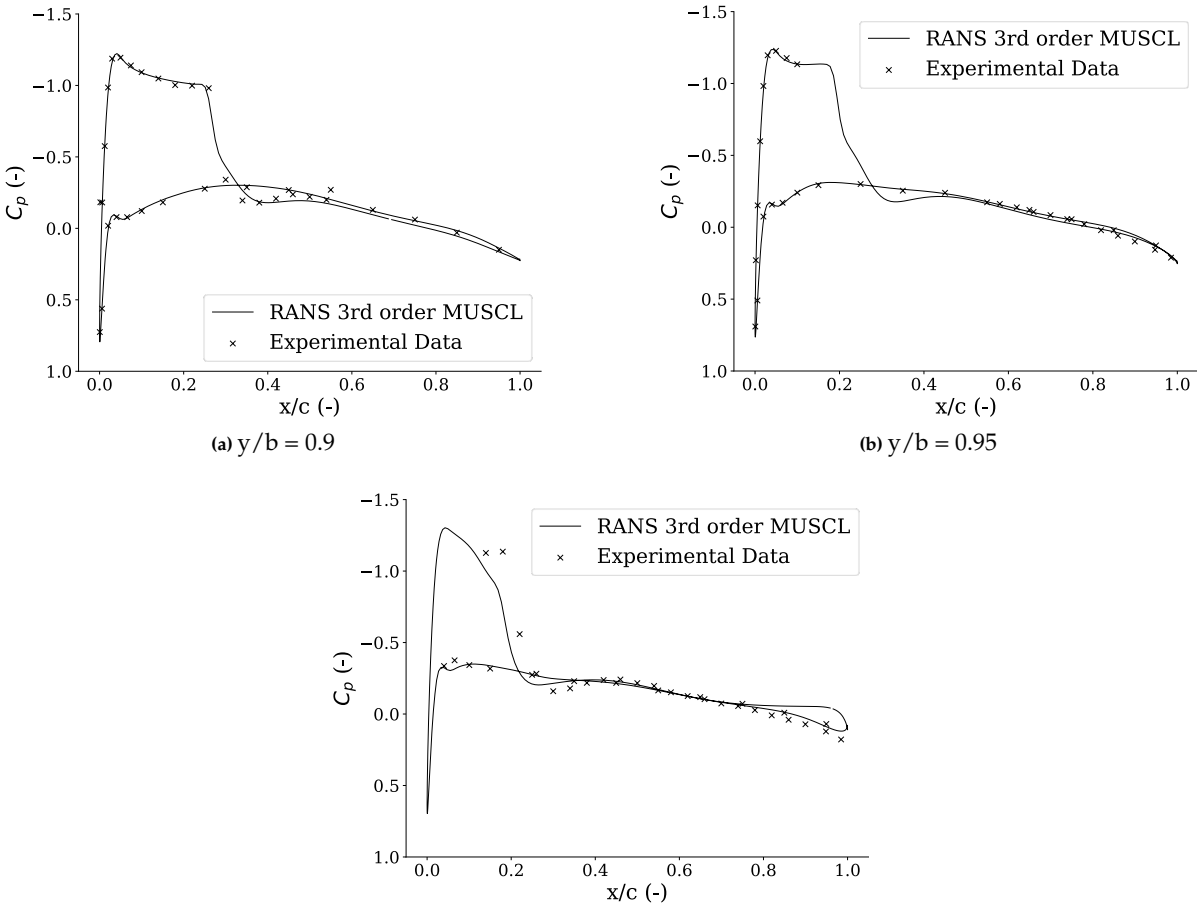

(a) y/b = 0.9

(b) y/b = 0.95

(c) y/b = 0.99

Figure 7.2: Pressure distribution validation on the ONERA M6 wing (Mach = 0.8395, AOA = 3.06 degrees, Re = 11.72 million)

8

Appendix B: Pressure Distributions Final Design

Appendix B shows the pressure distributions of the final design at every 2.5m of wing halfspan.

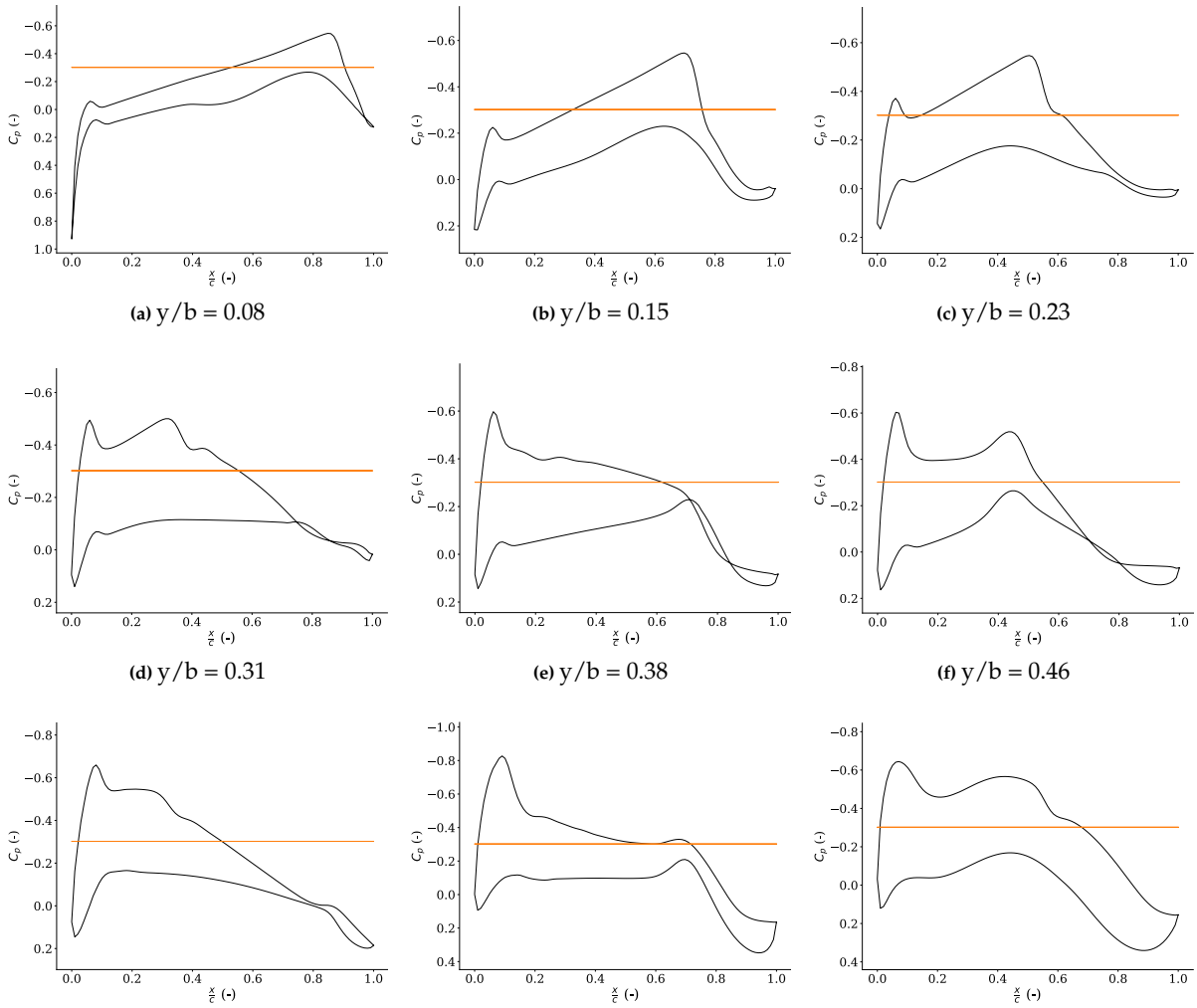

(a) y/b = 0.08 **(b)** y/b = 0.15 **(c)** y/b = 0.23

(d) y/b = 0.31 **(e)** y/b = 0.38 **(f)** y/b = 0.46

(g) y/b = 0.54 **(h)** y/b = 0.62 **(i)** y/b = 0.69

Figure 8.1: Pressure distributions of the final design (Mach =0.85, Re = 88.3 million, C_L = 0.26)

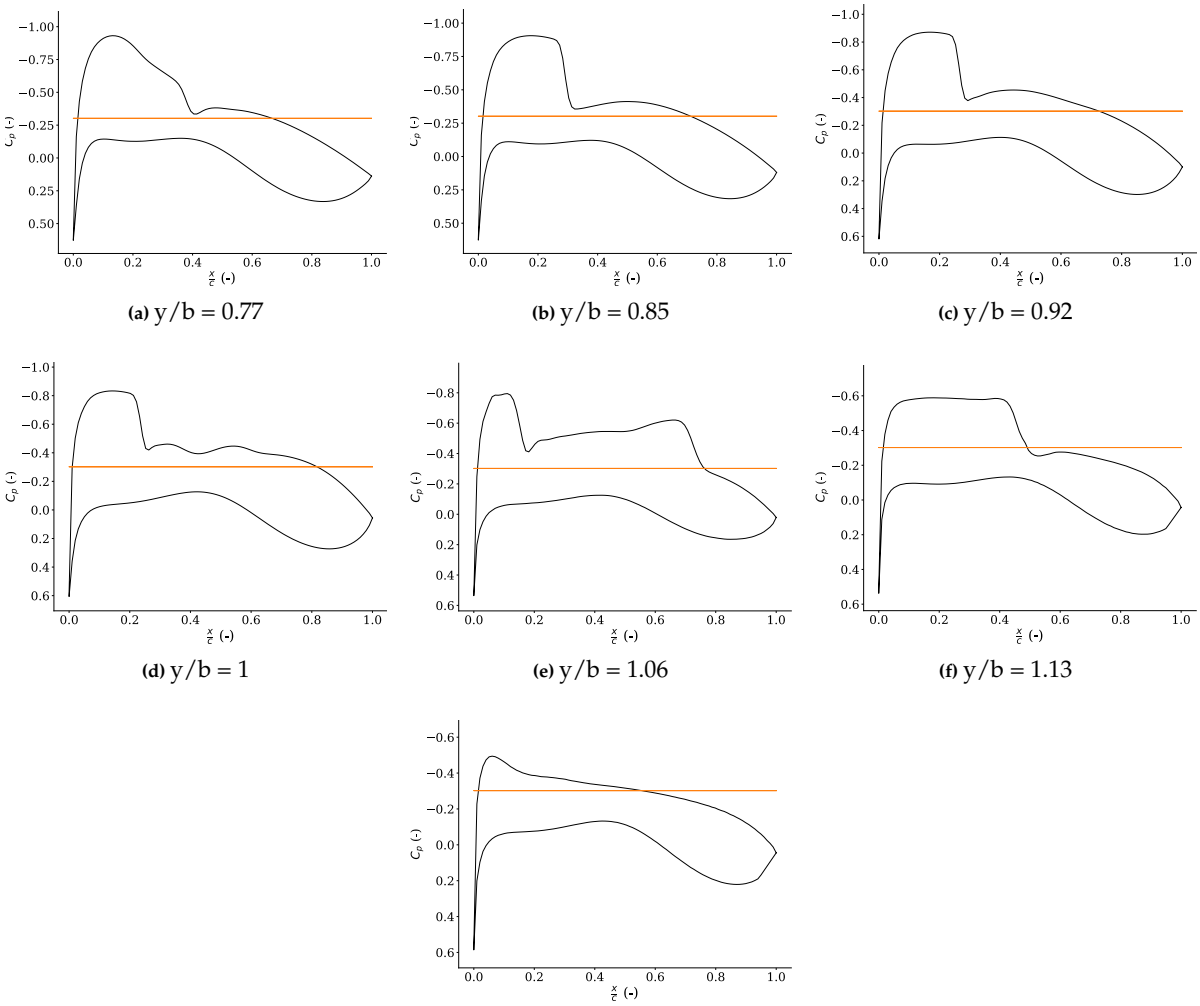

(a) y/b = 0.77 **(b)** y/b = 0.85 **(c)** y/b = 0.92

(d) y/b = 1 **(e)** y/b = 1.06 **(f)** y/b = 1.13

(g) y/b = 1.18

Figure 8.2: Pressure distributions of the final design (Mach =0.85, Re = 88.3 million, C_L = 0.26)